Dark Current and Persistence in HgCdTe-on-Si Infrared Detectors

---

Ph.D. *Doctor of Philosophy*

in Astrophysical Sciences and Technology

Lazar Buntic

School of Physics and Astronomy

Rochester Institute of Technology

Rochester, New York

December 2025

ASTROPHYSICAL SCIENCES AND TECHNOLOGY

COLLEGE OF SCIENCE

ROCHESTER INSTITUTE OF TECHNOLOGY

ROCHESTER, NEW YORK

Ph.D. DISSERTATION DEFENSE

Candidate: .....

Dissertation Title: .....

Adviser: .....

Date of defense: .....

The candidate's Ph.D. Dissertation has been reviewed by the undersigned. The Dissertation

(a) is acceptable, as presented.

(b) is acceptable, subject to minor amendments.

(c) is not acceptable in its current form.

Written details of required amendments or improvements have been provided to the candidate.

Committee:

Dr. Stefan Preble, Committee Chair

Dr. Michael Zemcov, Committee Member

Dr. Roger Smith, Committee Member

Dr. Donald F. Figer, Thesis Advisor

Please submit form to AST Graduate Program Coordinator

ASTROPHYSICAL SCIENCES AND TECHNOLOGY
COLLEGE OF SCIENCE
ROCHESTER INSTITUTE OF TECHNOLOGY
ROCHESTER, NEW YORK

CERTIFICATE OF APPROVAL

Ph.D. DEGREE DISSERTATION

The Ph.D. Degree Dissertation of *Lazar Buntic* has been examined and approved by the dissertation committee as satisfactory for the dissertation requirement for the Ph.D. degree in Astrophysical Sciences and Technology.

Dr. Stefan Preble, Committee Chair

Dr. Michael Zemcov, Committee Member

Dr. Roger Smith, Committee Member

Dr. Donald F. Figer, Thesis Advisor

Date

Dark Current and Persistence in HgCdTe-on-Si Infrared Detectors

By

Lazar Buntic

A dissertation submitted in partial fulfillment of the requirements for the degree of Ph.D. in Astrophysical Sciences and Technology, in the College of Science, Rochester Institute of Technology.

December, 2025

Approved by

Dr. Andrew Robinson	Date
Director, Astrophysical Sciences and Technology	

For Meghan, light of my life, my muse, and unending source of motivation. This would not have been possible without you.

Acknowledgments

I am incredibly grateful for the support that made this thesis possible, funded by a NASA FINESST Grant (Award Number 80NSSC22K1595).

I would like to acknowledge my colleagues at the Center for Detectors: Justin Gallagher, for keeping my harebrained schemes from running amok, Edwin Alexani, for his endless supply of humor and moral support, and my advisor Don Figer, for his inexhaustible knowledge of detector physics and always asking just the right questions to result in more research. He is fond of saying that there is infinite work to be done, and even after all these years I feel that I have barely scratched the surface of this field. I want to thank David Fanning, an unsung hero, whose open-source IDL library (idl-coyote) has prevented many IDL-related headaches. I would like to thank my family and friends for their love and support, too numerous to name here. You and your families have provided an invaluable quantity of joy and laughter to my life.

Finally, I acknowledge the use of Grok 4.1 (internal build v4.1-20251206-1), a large language model developed by xAI, as an auxiliary tool for proofreading, identifying grammatical errors, and enhancing the readability and consistency of the text. All scientific content, analysis, and conclusions remain the sole responsibility of the author.

Abstract

This thesis investigates the performance of Raytheon's mercury-cadmium-telluride-on-silicon (MCT-on-Si) infrared detector arrays, with particular emphasis on the impact of the heteroepitaxial silicon growth process on dark current and persistence characteristics.

Infrared detectors have been the cornerstone of astronomical discovery for the past four decades and remain essential for current and future flagship observatories, including the James Webb Space Telescope. Traditionally, the highest-performance HgCdTe (MCT) arrays are grown on lattice-matched cadmium-zinc-telluride (CZT) substrates, which are costly and limited in size. To enable low-cost, large-format arrays, Raytheon developed a process for direct epitaxial growth of MCT on silicon wafers. The large lattice mismatch inherent to this approach introduces defects that degrade detector performance, and these effects are systematically characterized in the present work.

Analysis of the best-performing pixels in the SATIN engineering-grade array (detector V23) reveals dark current levels substantially closer to those of state-of-the-art MCT-on-CZT devices than previously reported for MCT-on-Si technology. Persistence measurements demonstrate that charge-trapping timescales span many orders of magnitude and that trapping occurs almost exclusively within the bulk active region rather than at surface states. A clear correlation is established between larger p-n junction implant area and elevated dark current, driven by increased defect density in the active volume. Finally, on-sky observations obtained with the SATIN detectors are presented.

The results presented here indicate that MCT-on-Si technology, when combined with modern small-pixel architectures, offers a viable path toward low-cost, large-format, high-performance infrared imaging arrays for future astronomical instruments.

Contents

List of Figures

List of Tables

Chapter 1

Introduction

The night sky has long served as a powerful symbol for humanity. Throughout human history and prehistory, it has represented the unknown: distant and incomprehensible, yet beautiful and alluring. Astronomers are a natural outgrowth of the mammalian drive to comprehend our environment and thereby master it. Although modern astronomy is often traced to the ancient Greeks and, later, to the scholars of the Islamic Golden Age, humans have studied the stars for hundreds of millennia. As early hominins, our ancestors depicted constellations on cave walls and navigated vast distances using celestial cues. They developed sophisticated knowledge of equinoxes, constellations, and stellar motions, which they recorded in enduring stone monuments. [1] The pillars at Göbekli Tepe, for instance, appear to document the Younger Dryas impact event as coinciding with an encounter with the Taurid meteor stream.

1.1 A Brief History of Imagers

The ancient study of the sky relied on a remarkable yet limited natural imager: the human eye. Although the eye is well suited for everyday vision, it lacks the characteristics required of a scientific detector. The human brain, acting as sophisticated readout electronics, effectively masks many of these limitations — non-uniform spatial response, blind spots, wavelength-

dependent sensitivity, saturation, and severe persistence effects.[1] Most critically, the eye cannot integrate light over long periods, both because of its physiological design and because a human observer cannot remain sufficiently motionless.

Consequently, nearly all major advances in astronomy beyond simple catalogs of the brightest objects have required corresponding technological breakthroughs. The 19th century began with the development of photographic plates, which rapidly gave rise to the first dedicated astronomical imaging systems. A mere decade after the first daguerreotype, in 1840, J. W. Draper and others used photographic plates to record images of the Moon. Although film soon replaced plates in commercial photography, astronomical plates remained in widespread use until the late 20th century, most famously for the Palomar Observatory Sky Surveys conducted in the 1950s and again in the 1990s.

Photographic plates were only the first modern imaging technology; the 20th century saw the development of numerous electronic devices for collecting and quantifying light. The photomultiplier tube (PMT), invented in the 1930s by the Soviet physicist Leonid Kubetsky, exemplifies this transition. In a PMT, an incident photon striking the photocathode ejects a photoelectron, which a series of increasingly positive dynodes then accelerates and multiplies through secondary emission. A single photoelectron can thereby produce an avalanche of thousands or millions of electrons at the anode, generating a readily measurable voltage pulse. A related device, the proportional gas counter developed in the 1940s, operates on a similar principle of controlled electron multiplication within a noble-gas-filled chamber surrounding a high-voltage anode wire. When an ionizing particle or photon enters the chamber, it triggers a localized electron avalanche that produces a detectable signal. The core concept of electron multiplication pioneered in these early devices remains central to many state-of-the-art detectors today, albeit in radically different implementations.

The invention of the transistor in 1947, followed by rapid progress in solid-state electronics, laid the foundation for digital information storage. Complementary Metal-Oxide-Semiconductor (CMOS) technology emerged in the 1960s, but its application to imaging had

[1] Persistence manifests as the afterimage observed after viewing a bright source such as the Sun, a lightning bolt, or a welding arc, and then closing one's eyes.

to await the development of the active-pixel sensor (APS) architecture. The first practical CMOS APS was demonstrated in 1993 by Eric Fossum and his collaborators. Independently, the charge-coupled device (CCD) was invented in 1969 by Willard Boyle and George Smith at Bell Laboratories. They recognized that charge packets could be stored in metal-oxide-semiconductor (MOS) capacitors and sequentially transferred along a linear or two-dimensional array by applying appropriate clock voltages. Within two years, by 1971, the first CCD imagers were operational. The introduction of the CCD marks the beginning of the modern era of electronic imaging in astronomy. Since the 1970s, CCDs, and later CMOS sensors and their derivatives, have become the dominant detectors in virtually every major astronomical imaging instrument.

1.2 Infrared Light

Infrared (IR) radiation was discovered in 1800 by William Herschel. He passed sunlight through a glass prism and showed that thermometers placed just beyond the visible red end of the spectrum registered a temperature rise even though no visible light reached them. Throughout the 19th century, rudimentary IR detectors—primarily bolometers and thermopiles—were developed. These devices produce a measurable voltage in response to temperature changes in their absorbing elements.

Simple "night vision" devices were conceived for use in anti-air applications in the first half of the 20th century, and saw further development at the hands of major players in the second world war, primarily the Germans and Americans. The breakthrough for modern IR astronomy came from advances in narrow-gap semiconductors: indium antimonide (InSb) was first synthesized in 1952, and mercury cadmium telluride (HgCdTe or MCT) was developed in 1959. The tunable bandgap of MCT proved especially revolutionary, enabling detectors optimized for specific infrared wavelength ranges. These detectors cover the 1–30 μm range, although the majority of astronomical applications exploit the 1–15 μm interval.

1.3 Mercury Cadmium Telluride on Silicon

$Hg_{1-x}Cd_xTe$—where x is the cadmium mole fraction—is a II-VI ternary semiconductor alloy that has historically been the premier material for infrared detectors. It offers exceptional flexibility in wavelength tuning from 1–30 μm, enabling detectors for a wide range of military, medical, and scientific applications. Adjusting x directly controls the bandgap and thus the long-wavelength cutoff of the detector.

Historically, infrared MCT arrays have been grown epitaxially on cadmium-zinc-telluride (CdZnTe or CZT) substrates. These substrates provide excellent lattice matching to MCT, resulting in absorber layers with very low defect density. Low defect density is critical because dark current in these detectors scales strongly with the concentration of mid-gap traps. Unfortunately, CZT remains expensive and difficult to produce in large areas; typical wafers measure only 10–100 cm^2. To overcome the size and cost limitations of CZT, substantial efforts in the late 1980s and early 1990s focused on heteroepitaxial growth of MCT directly on silicon substrates.[2, 3] Silicon wafers are far less expensive and readily available in diameters exceeding twelve inches ($\geq$700 cm^2), making them highly attractive for large-format focal-plane arrays. The detectors characterized in this thesis were grown using Raytheon's most recent MCT-on-Si process, which inserts thick buffer layers between the silicon substrate and the MCT absorber to mitigate dislocations arising from the large lattice mismatch. This same buffer-layer approach was developed in parallel with the MCT-on-CZT detectors supplied for the VISTA observatory, although performance testing at the time revealed an excessively high dark-current tail for that particular application.[4, 2]

This elevated dark current arises primarily from threading dislocations generated by lattice mismatch between the substrate and the epitaxial layers. Such mismatch becomes especially severe when the constituent materials exhibit substantially different lattice constants, as illustrated in Figure 1.1 for numerous semiconductor alloys of interest. Two ternary alloys—CZT and MCT—are included for reference, although their exact lattice constants and bandgaps vary with alloy composition.

The conventional growth approach (*i.e.*, MCT grown on lattice-matched CZT substrates)

minimizes mismatch and therefore defectivity. Precise adjustment of the cadmium mole fraction in the CZT substrate places its lattice constant between those of ZnTe and CdTe, as shown in Figure 1.1. Similarly, MCT lies between CdTe and HgTe. This plot also explains the widespread use of MCT in infrared detectors: the large separation in bandgap along the y-axis between HgTe and CdTe enables continuous tuning over a broad range of cutoff wavelengths. By finely controlling the cadmium fraction in the CZT substrate, state-of-the-art detectors (for example, Teledyne's HxRG series) achieve near-perfect lattice matching with the MCT absorber, thereby attaining extremely low defect densities.

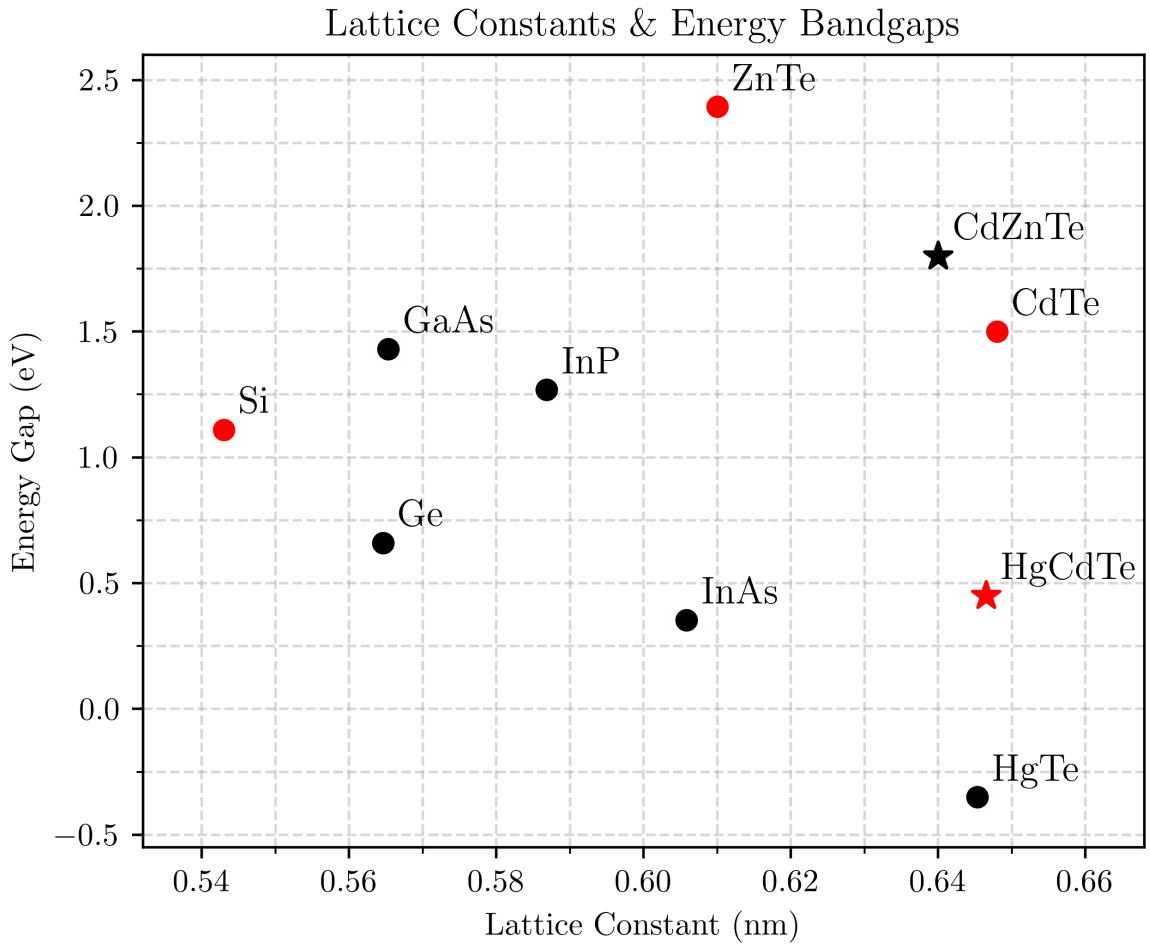

Figure 1.1: The figure displays lattice constants and energy bandgaps for several semiconductor alloys commonly employed in detector fabrication. The positions of the ternary alloys CZT and MCT vary with cadmium mole fraction.

The detectors developed for the SATIN program had to overcome the large lattice mismatch between silicon and MCT. This challenge was addressed by growing two buffer layers on the silicon wafer before depositing the MCT absorber. The growth sequence consists of a ZnTe layer on the silicon substrate, followed by a CdTe layer, and finally the HgCdTe device structure. This layered approach has proven effective at terminating the majority of threading dislocations at the heterointerfaces.[5]

After completion of the full epitaxial stack, most of the buffer material is removed by selective etching. Only a small amount of CdTe is retained on the backside of the MCT, and this residual layer is subsequently passivated to suppress surface states that would otherwise generate significant dark current. One consequence of retaining this CdTe layer is that it imposes a short-wavelength quantum-efficiency cutoff near 800 nm (see Section 3.5).

1.4 History of the SATIN Detector Development Program

The SATIN (SWIR Advanced Technology Instruments for NSF and NASA) program was a two-phase development effort funded jointly by NSF and NASA to improve the performance of MCT detectors grown on silicon substrates for astrophysical applications. Phase I supported the fabrication of two detector lots. The first lot was comprised of two 2048×2048 arrays—one grown on CZT (designated 9A) and one on silicon (VIRGO-14)—together with five variable-unit-cell (VUC) test devices (V1–V6). The 9A and VIRGO-14 arrays established the performance baseline for subsequent lots. Each VUC device contained four quadrants with different mesa sizes; characterization of these quadrants directly informed the design of the second Phase I lot, which consisted of three detectors (F3, F6, and VTHIN1) with 17 μm mesas. Although this second lot satisfied nearly all original program goals, the measured dark current remained approximately a factor of three higher than the target value.

Phase II continued the development with three additional fabrication rounds. The first round evaluated two new substrate-removal and annealing processes. The second round focused on reducing the dark-current tail by limiting defect propagation from the buffer layers into the absorber. The third and final round introduced a shift from the mesa architecture

used throughout Phase I to a planar architecture. This final lot produced eight devices, designated V21 through V28. The results presented in this thesis are based primarily on V23, which is the highest-performing detector from this lot.

V23 is the only device from the final SATIN lot that arrived at RIT without major mechanical damage. A packaging failure during shipment from Raytheon damaged most detectors in the lot. Although all devices were returned to Raytheon for wire-bond repair, the cosmetic and surface damage remained. V23 suffered the least surface damage and has therefore served as the primary subject of our characterization work. Figure 1.2 shows a quadrant map and a high-resolution scan of V23.

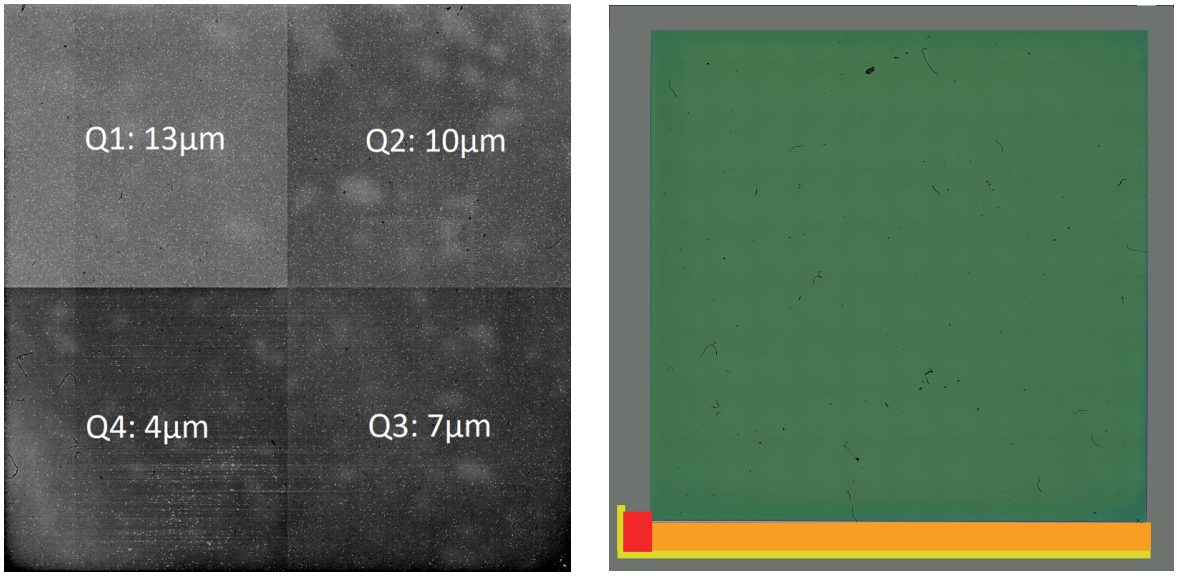

Figure 1.2: Left: A quadrant map of V23 indicating the p-n junction implant sizes in each quadrant. Right: A high-resolution optical scan of V23 with edge circuitry and identifying markings redacted. The yellow region marks the wire-bond attachment pads to the ROIC, the orange region covers the column output circuitry, and the red region covers the clocking and protection circuitry.

1.4.1 Materials and Dopants

The SATIN detectors employ a p-on-n $Hg_{1-x}Cd_xTe$ heterostructure in which a p-type layer doped with arsenic is grown on top of an n-type layer doped with indium. The exact doping concentrations and profiles remain proprietary to Raytheon. Nevertheless, several key material

parameters can be inferred from measured device performance, including the cadmium mole fraction x and the dielectric constant ϵ.

The cadmium mole fraction x is the primary determinant of the detector cutoff wavelength. An empirical expression for the temperature-dependent bandgap E_g (in eV) of $Hg_{1-x}Cd_xTe$ was derived by Hansen *et al.*:[6]

$$E_g(x,T) = -0.302 + 1.93x + 5.35 \times 10^{-4}T(1-2x) - 0.810x^2 + 0.832x^3, \tag{1.4.1}$$

where x is the mole fraction and T is the temperature in kelvin (typically 70 K for the measurements presented here). The measured cutoff wavelength of V23 is 2750 nm (see Section 3.5). The corresponding bandgap is

$$E_g = \frac{hc}{\lambda q} = 0.451\,\text{eV}, \tag{1.4.2}$$

where $h = 6.626 \times 10^{-34}$ J/Hz is Planck's constant, $c = 2.998 \times 10^8$ m/s is the speed of light, and $q = 1.6 \times 10^{-19}$ J/eV is the elementary charge. Substituting $E_g = 0.451$ eV and $T = 70$ K into Equation (1.4.1) and solving the resulting cubic equation for x yields a single physically meaningful root:

$$x = 0.431. \tag{1.4.3}$$

1.4.2 ROIC Structure

The VIRGO readout integrated circuit (ROIC) employs a three-transistor (3T) pixel architecture, shown schematically in Figure 1.3. The three transistors perform the following functions: the select transistor (SEL) connects the pixel to the column bus during readout, the reset gate transistor (RG) restores the integration node to the nominal reset voltage after readout, and the source-follower transistor (SF) buffers the photodiode signal before it is driven off-chip.[7] The detector common bias is labeled vdetCom, the source-follower drain supply is vnUc, and the reset voltage is vrstUc. The effective reverse bias across the detector is V_r = vrstUc − vdetCom.

Although the exact physical layout of these components is proprietary to Raytheon, their

general placement can be inferred from the known 3T architecture and from similar designs reported in the literature. The photodiode resides in the HgCdTe layer, where the p-n junction meets the indium bump that hybridizes the detector array to the ROIC. This indium bump connects the photodiode cathode to the floating-diffusion (sense) node labeled FD. To the right of each pixel lies the column bus. The column slew current source is denoted Islew, the analog supply for the column current source is vpUc, the output source-follower return is vnOut, and COL leads to a second source-follower stage that requires an external current source I_{ext}.

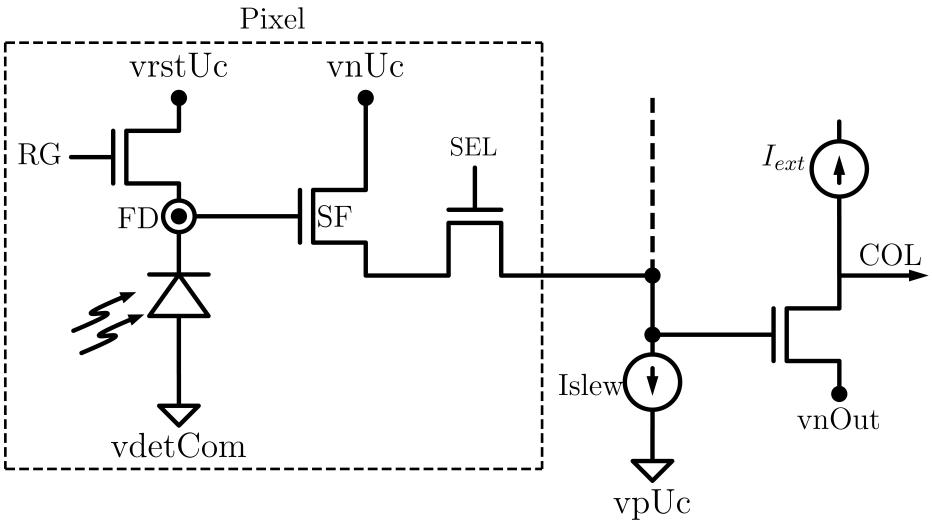

Figure 1.3: The figure shows the 3T pixel architecture used in the VIRGO ROIC. The three transistors are labeled SEL (select), RG (reset gate), and SF (source follower).

Chapter 2

Theory

2.1 p-n Junction Theory

The p-n junction forms the core of every detector pixel and enables the integration and collection of photogenerated charge. Modern semiconductor detectors would not exist without it. A brief review of p-n junction physics is therefore essential for understanding the operation of virtually all semiconductor-based active-pixel sensors.

2.2 Properties of the p-n Junction

A p-n junction forms when a p-doped semiconductor region, containing a high concentration of mobile holes from acceptor impurities, is brought into direct contact with an n-doped region, which contains a high concentration of mobile electrons from donor impurities (Figure 2.1a). Immediately after contact, electrons diffuse from the n-side into the p-side, and holes diffuse from the p-side into the n-side. This carrier diffusion uncovers fixed, uncompensated charges: positively charged donor ions (N_d^+) on the n-side and negatively charged acceptor ions (N_a^-) on the p-side. The resulting charge separation establishes a depletion region devoid of mobile carriers and produces a built-in electric field directed from the n-side to the p-side (Figure 2.1b).[8]

Although the depletion region is often drawn symmetrically for simplicity, the depletion

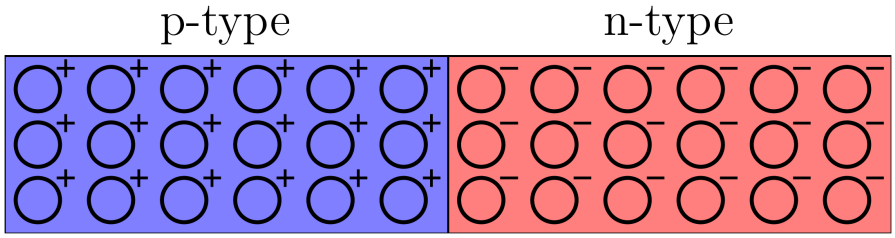

(a) A theoretical p-n junction at the moment the p-type and n-type materials are joined, with symbols representing the donor and acceptor ions. In reality, one layer is grown atop another, but this representation is a useful tool for understanding how the depletion region evolves.

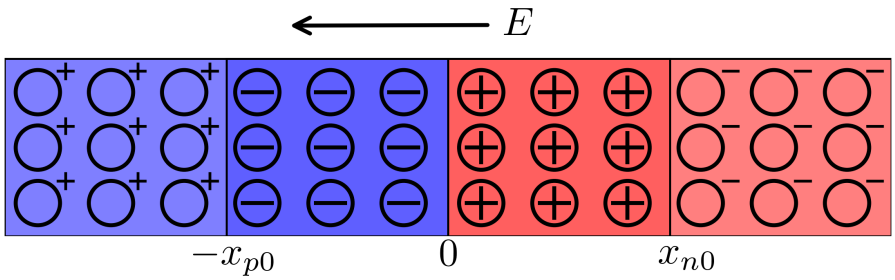

(b) The p-n junction shortly after the initial joining, after the diffusal of free carriers across the junction. The depletion region is now populated by uncompensated acceptor and donor atoms. The carriers stripped from the dopant atoms neutralize a small number of dopant atoms just outside of the depletion region, shown in Figure 2.5.

Figure 2.1

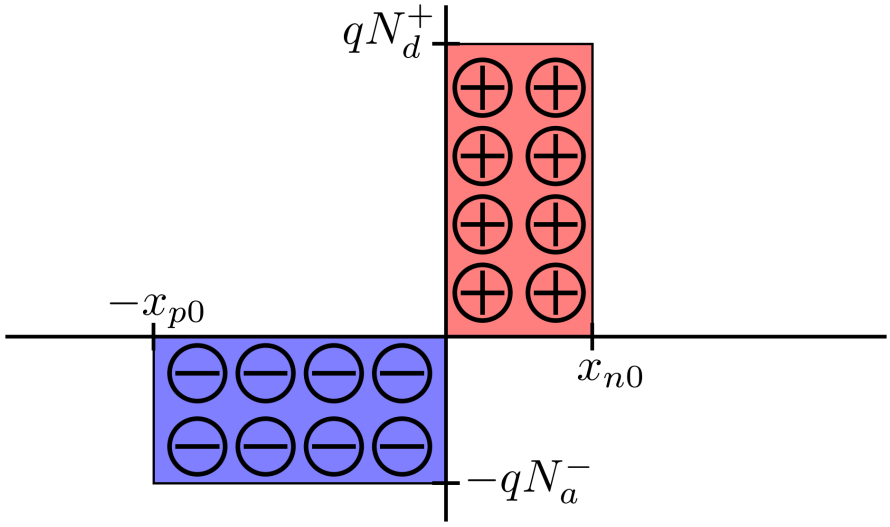

(a) A charge density distribution for the p-n junction at equilibrium. The abrupt borders at x_{p0} and x_{n0} due to carrier depletion within the depletion region and neutrality outside it are an approximation; In reality, the edge is a sharp gradient.

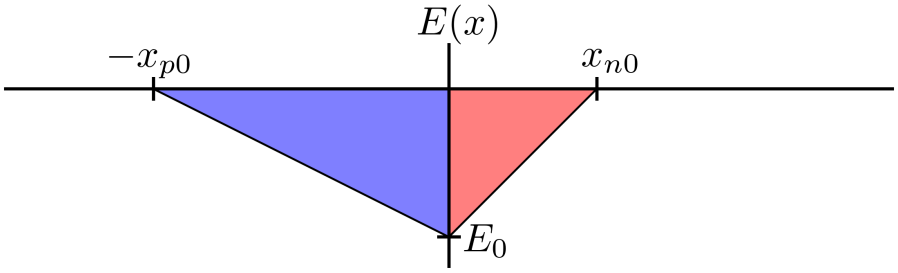

(b) A depiction of the strength of the electric field within the depletion region of the p-n junction, with a peak strength of E_0.

Figure 2.2

widths on the two sides are generally unequal ($x_{p0} \neq x_{n0}$). This asymmetry arises because charge neutrality requires the total positive charge on the n-side to equal the magnitude of the total negative charge on the p-side ($Q_+ = |Q_-|$), while the doping concentrations themselves are typically very different ($N_a \neq N_d$, often by orders of magnitude). Figure 2.2a and Equation 2.2.1 show that the total uncompensated charge on either side of the junction is equal:

$$Q_+ = |Q_-| \implies qAN_d^+ x_{n0} = qAN_a^- x_{p0} \tag{2.2.1}$$

where A is the cross-sectional area of the junction. Importantly, this charge-balance equation simplifies to $N_d x_{n0} = N_a x_{p0}$, which will be useful below (note that $N = N^{+/-}$ as the density of ions is an intrinsic property of the physical material). The maximum strength of the electric field E_0 in Figure 2.2b can be calculated by integration for either side of the p-n junction:

$$\frac{dE}{dx} = \frac{qN_d}{\epsilon\epsilon_0}, \quad 0 < x < x_{n0} \implies \int_{E_0}^{0} dE = \frac{qN_d}{\epsilon\epsilon_0} \int_0^{x_{n0}} dx \implies E_0 = -\frac{qN_d}{\epsilon\epsilon_0} x_{n0} \tag{2.2.2}$$

$$\frac{dE}{dx} = \frac{qN_a}{\epsilon\epsilon_0}, \quad -x_{p0} < x < 0 \implies \int_{0}^{E_0} dE = \frac{qN_a}{\epsilon\epsilon_0} \int_{-x_{p0}}^{0} dx \implies E_0 = -\frac{qN_a}{\epsilon\epsilon_0} x_{p0} \tag{2.2.3}$$

The built-in potential V_0 across the depletion region can be obtained by integrating the electric field, $E(x) = -\mathrm{d}V/\mathrm{d}x$, or equivalently by evaluating the area under the electric-field profile shown in Figure 2.2b:

$$V_0 = -\frac{1}{2}\left(x_{p0}E_0 + x_{n0}E_0\right) = -\frac{1}{2}E_0 W_{\mathrm{dep}} \tag{2.2.4}$$

where $W_{\mathrm{dep}} = x_{p0} + x_{n0}$ is the total width of the depletion region. Substituting Equation 2.2.2 for E_0:

$$V_0 = \frac{1}{2}\frac{q}{\epsilon\epsilon_0} N_d x_{n0} W_{\mathrm{dep}} \tag{2.2.5}$$

Recalling that $N_d x_{n0} = N_a x_{p0}$ and $W_{\mathrm{dep}} = x_{p0} + x_{n0}$, we can solve for x_{n0} as:

$$x_{p0} = x_{n0}\frac{N_d}{N_a} \implies W_{\mathrm{dep}} = x_{n0}\left(1 + \frac{N_d}{N_a}\right) = x_{n0}\left(\frac{N_a + N_d}{N_a}\right) \implies x_{n0} = \frac{W_{\mathrm{dep}} N_a}{N_a + N_d} \tag{2.2.6}$$

and make a final substitution into Equation 2.2.5 to get the intrinsic potential across the

junction:

$$V_0 = \frac{qN_dN_a}{2\epsilon\epsilon_0(N_d + N_a)}W_{\text{dep}}^2 \tag{2.2.7}$$

where N_a is the concentration of acceptor ions in the p-type material, N_d is the concentration of donor ions in the n-type material. Under the assumption of a linearly graded junction, V_0 can be calculated independently of W_{dep} [9, 8], or even just approximated as $V_0 = E_g/q$ [10, 11]:

$$V_0 = \frac{kT}{q}\ln\left(\frac{N_aN_d}{n_i^2}\right) \tag{2.2.8}$$

where n_i is the intrinsic carrier concentration of the parent material due to thermal excitation of electrons from the valence to the conduction band.[12] n_i is given by:

$$n_i = (5.585 - 3.820x + 1.753 \times 10^{-3}xT)\left[10^{14}{E_g}^{3/4}T^{3/2}e^{-\frac{E_g}{2k_bT}}\right] \tag{2.2.9}$$

where x is the cadmium mole fraction, T is the temperature in Kelvin, and E_g is the bandgap energy of the MCT material.[6] W_{dep} can be derived by solving Equation 2.2.7 for:

$$W_{\text{dep}} = \left[\frac{2\epsilon\epsilon_0(V_0 - V_a)}{q}\left(\frac{N_a + N_d}{N_aN_d}\right)\right]^{\frac{1}{2}} \tag{2.2.10}$$

where ϵ is the dielectric constant for the detector material, $\epsilon_0 = 8.85 \times 10^{-12}\,\text{F/m}$ is the vacuum permittivity, $q = 1.6 \times 10^{-19}\,\text{C}$ is the elementary charge. V_a is a variable added to represent any externally applied voltage, and for $Hg_{1-x}Cd_xTe$, $\epsilon \approx 20.5 - 15.5x - 5.7x^2$, where x is the cadmium mole fraction.[13, 14, 15]

A p-n junction is forward-biased when the p-region is held at a positive voltage relative to the n-region. In this regime the potential barrier is reduced, the depletion region narrows, and current can flow across the junction. Conversely, the junction is reverse-biased when a negative voltage is applied to the p-region relative to the n-region. The depletion region then widens and only a very small saturation current flows. The ideal diode equation that describes this behaviour is:

$$I_{\text{ideal}} = I_0\left(\exp\left[\frac{qV}{kT}\right] - 1\right), \tag{2.2.11}$$

where I_0 is the reverse saturation current, q is the elementary charge, V is the applied voltage (positive for forward bias), k is Boltzmann's constant, and T is the absolute temperature.

The ideal diode equation holds until the reverse bias reaches a critical magnitude, at which point the junction undergoes reverse breakdown and large currents flow. Figure 2.3 shows the current–voltage characteristic of a p-n junction, illustrating exponential current increase under forward bias and breakdown at large reverse bias.

Figure 2.4a presents the equilibrium band diagram of the p-n junction, while Figure 2.4b shows the band diagram under an applied reverse bias V_r. The potential difference between the conduction (and valence) bands in the p- and n- regions is proportional to $V_0 - V_r$, while the depletion width increases with the square root of this potential difference, as given in Equation (2.2.10). As the reverse bias magnitude increases, the bands tilt more steeply and the probability of band-to-band tunneling rises significantly. This mechanism will be examined as a source of dark current in Section 2.3.3.

Figure 2.3: This figure shows the current–voltage characteristic of a p-n junction, illustrating exponential current increase under forward bias and breakdown at large reverse bias.

2.2.1 Capacitance of a p-n Junction

The p-n junction under reverse bias behaves like a parallel-plate capacitor. The associated depletion capacitance C_{dep} depends on both the junction area and the depletion width. It consists of two contributions: the bottom-junction capacitance C_b (Equation (2.2.12)) and the sidewall capacitance C_s (Equation (2.2.13)). The total depletion capacitance is therefore $C_{\text{dep}} = C_b + C_s$.

$$C_b = \frac{\epsilon\epsilon_0 A}{W_{\text{dep}}} \left(1 - \frac{V}{V_0}\right)^{-m_b} \tag{2.2.12}$$

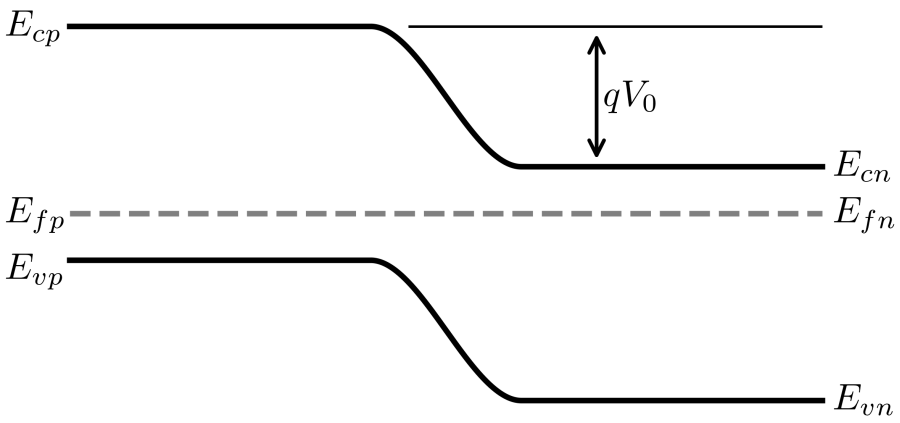

(a) The figure shows the band diagram of a p-n junction at equilibrium. The conduction-band edge is labeled E_c, the valence-band edge is E_v, and the Fermi level is E_f. Subscripts p and n denote the p-side and n-side of the junction, respectively.

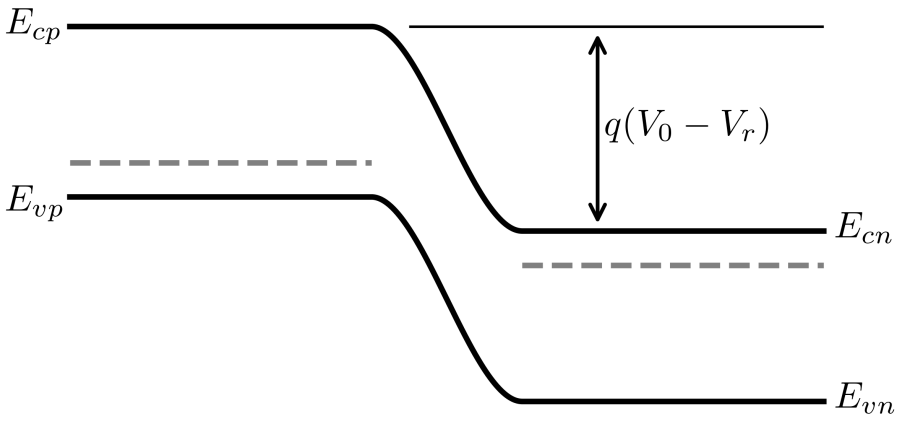

(b) The figure shows the band diagram of a p-n junction under an applied reverse bias V_r. The Fermi levels remain at approximately the equilibrium value in its respective neutral region; E_{fp} and E_{fn} are separated by the applied voltage from one another.

Figure 2.4

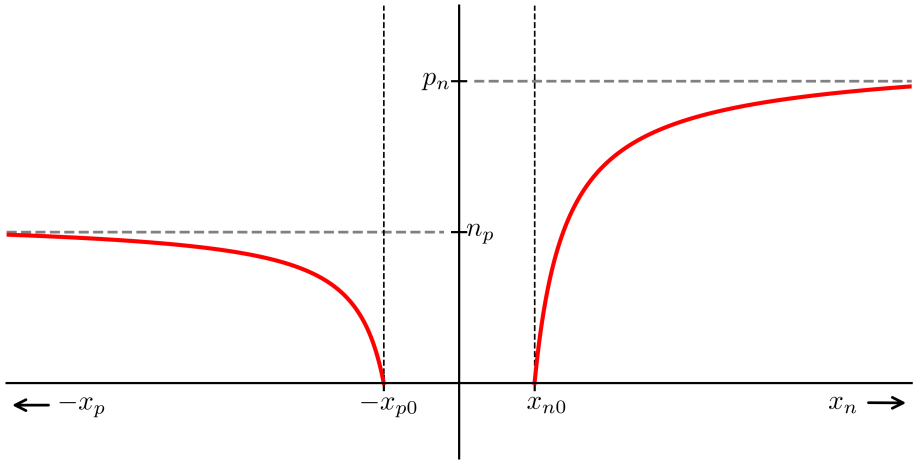

Figure 2.5: This figure shows a diagram of minority carrier distribution in the neutral regions that surround the depletion region of the p-n junction.

$$C_s = \frac{\epsilon\epsilon_0 A_s}{W_s}\left(1 - \frac{V}{V_0}\right)^{-m_s} \tag{2.2.13}$$

where V_0 is the intrinsic potential of the junction, V is the voltage across the junction when accounting for the reverse bias and integrated charge, W_s is the sidewall depletion depth, $A_s = Pd$ is the area of the sidewall component which is the product of the perimeter P of the implant and the depth d of the implant, A is the bottom area of the p-n junction, and m_s and m_b are junction grading coefficients for the sidewall and bottom gradients, respectively. There are additional sources of capacitance in each pixel arising from the MOS gate (C_g) and other sources of parasitic capacitance, though modeling them is rather difficult without knowledge of grading profiles, ROIC component locations, and other proprietary detector parameters. For the purposes of the modeling within this thesis, the gate capacitance is modeled as such:

$$C_g = \frac{\epsilon\epsilon_0 LW}{Z}\left(1 - \frac{V}{V_0}\right)^{-m_g} \tag{2.2.14}$$

where L and W are the length and width of the gate implant, Z is the thickness of the gate, and m_g is a scaling factor.

In the models presented in this thesis, the gate capacitance is used as an effective lumped parameter that accounts for multiple parasitic capacitance contributions. Accurate modeling

of the various capacitance contributions within a pixel is highly complex, even when the pixel and ROIC geometry are fully known. (Entire PhD theses have been devoted to this subject; see, for example, Wang [16].) A discussion of the dominant capacitance terms and their impact on detector linearity is presented in Section 3.6.

2.2.2 Charge Generation and Collection within the p-n Junction

When a photon with energy greater than the bandgap E_g is absorbed in the detector, it excites an electron from the valence band to the conduction band, generating a free electron–hole pair. Photons with energy below E_g cannot bridge the bandgap and therefore produce no photocarriers; this defines the intrinsic cutoff wavelength of the detector.

The built-in electric field, directed from the n-type cathode to the p-type anode, separates the photogenerated carriers. The electron drifts toward the cathode and accumulates there, while the hole drifts toward the anode (Figure 2.6).[17] As electrons collect on the cathode, the effective reverse bias across the junction decreases and the depletion region contracts. This phenomenon, often termed debiasing, gives rise to several secondary effects, including persistence (see Section 3.2).

At the end of the integration period, the pixel is selected, the accumulated charge is measured through the resulting voltage change across the junction, and the signal is digitized and stored. The photodiode is then reset to its original reverse-bias voltage, clearing the collected charge and preparing the pixel for the next integration cycle.

2.3 Dark Current

Dark current refers to the collective current generated in a photodiode in the absence of illumination. The primary mechanisms responsible for dark current in HgCdTe detectors are thermal generation of carriers within the depleted region and tunneling across the narrow bandgap. In state-of-the-art infrared and visible detectors, dark current can be extremely low, on the order of 10^{-5} e/pixel/s. For certain long-wavelength applications, however, significantly higher values are tolerated; the HgCdTe GeoSnap detectors, for example, exhibit dark

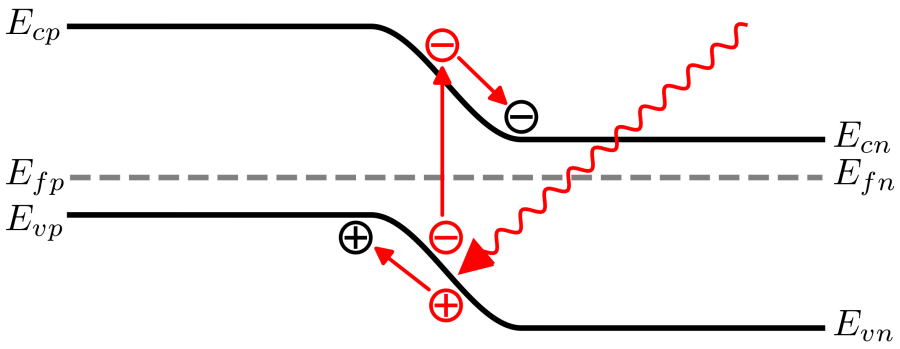

Figure 2.6: The figure illustrates the photogeneration process in a p-n junction. An incident photon with energy greater than the bandgap is absorbed and excites an electron from the valence band to the conduction band, thereby creating an electron–hole pair. The built-in electric field then sweeps the electron toward the n-side and the hole toward the p-side.

currents above 10^5 e/pixel/s.[18] This section presents models for the dominant dark-current mechanisms, which are compared with the measurements obtained for V23 in Section 3.3.

2.3.1 Diffusion

Diffusion current arises from thermally generated carriers that reach the edge of the depletion region and are subsequently swept across the junction by the built-in electric field. In the neutral p-type region, a small fraction of the electrons generated within one diffusion length of the depletion-region boundary diffuse to the junction and are injected into the n-side. Similarly, holes generated within one diffusion length of the junction in the neutral n-type region diffuse to the depletion-region edge and are injected into the p-side.[19, 8, 12, 20] Diffusion current is given in Equation 2.2.11, and can be expanded to this form in units of $e^-/s/\text{pix}$:

$$J_{\text{diff}} = \frac{A{n_i}^2 d}{N_d \tau_b} \left(e^{\frac{qV_{\text{actual}}}{k_b T}} - 1 \right) \tag{2.3.15}$$

where A is the area of the p-n junction in in cm^2, d is the thickness of the absorber region in cm, N_d is the donor ion dopant concentration in cm^{-3}, τ_b is the minority carrier lifetime in seconds, $q = 1.6 \times 10^{-19}$ is the elementary charge in coulombs, V_{actual} is total potential across the junction at any point in time, $k_b = 1.38 \times 10^{-23}$ J/K is the Boltzmann constant, T is the

temperature in Kelvin, and n_i is the intrinsic carrier concentration in cm^{-3} given by Equation 2.2.9. For the SATIN detectors, which are strongly reverse biased (1 V for nominal operation) diffusion is only expected to contribute at very high temperatures, dominating other sources of dark current above 120K.

2.3.2 Generation-Recombination

The generation-recombination component of dark current (in units of $e^-/s/\mathrm{pix}$) is given by [21]:

$$I_{\text{G-R}} = \frac{qAn_iW}{\tau_{GR}} \frac{\sinh\left(\frac{-qV_{\text{actual}}}{2k_bT}\right)}{\frac{q(V_0-V_{\text{actual}})}{2k_bT}} f(b) \tag{2.3.16}$$

where $f(b)$ and b are given by

$$f(b) = \int_{z_1}^{z_2} \frac{dz}{z^2 + 2bz + 1} \tag{2.3.17}$$

$$b = e^{\frac{-qV_{\text{actual}}}{2k_bT}} \cosh\left(\frac{E_i - E_{\text{trap}}}{k_bT}\right) \tag{2.3.18}$$

and $z_{1,2}$ are:

$$z_{1,2} = \left(\frac{\tau_{p0}}{\tau_{n0}}\right)^{1/2} e^{\mp\left(\frac{q(V_0-V_{\text{actual}})}{2k_bT}\right)} \tag{2.3.19}$$

where $q = 1.6\times10^{-19}$ is the elementary charge in coulombs, A is the area of the p-n junction in in cm^2, τ_{GR} is the carrier lifetime in seconds, V_{actual} is the bias applied to the detector in volts, V_0 is the intrinsic bias of the junction, k_b is the Boltzmann constant, T is the temperature in Kelvin, and n_i is the intrinsic carrier concentration in cm^{-3} given by Equation 2.2.9.[6].

Treatments of this model in the literature (Bacon[19], Cabrera[22]) extend the integration limits of $f(b)$ to be from 0 to ∞, which can be done when the applied bias is several kT/q less than the intrinsic bias of the junction, as is the case for Teledyne devices treated in those theses.[21] However, as the SATIN devices are meant to operate at much higher applied biases this simplification does not apply. Moreover, as the regime of interest for the SATIN detectors is at low temperatures, we find that the G-R current at high temperatures is adequately

modeled by the simplest form of the G-R function [10]:

$$I_{\text{G-R}} = \frac{qAn_iW}{\tau_{GR}} \tag{2.3.20}$$

2.3.3 Tunneling

Quantum-mechanical tunneling contributes to dark current through two principal mechanisms: direct band-to-band tunneling (BTBT), in which electrons tunnel from the valence band to the conduction band, and trap-assisted tunneling (TAT), in which electrons tunnel via mid-gap trap states. The band-to-band tunneling current (in e/s/pixel) is given by [11, 23]:

$$I_{bb} = -\frac{q^2AEV_{\text{actual}}}{4\pi^3\hbar^2}\sqrt{\frac{2m_{eff}}{E_g}}\exp\left(-\frac{\pi\sqrt{m_{eff}}{E_g}^{3/2}}{2\sqrt{2}q\hbar E}\right) \tag{2.3.21}$$

where E_g is the bandgap energy, m_{eff} is the effective mass of an electron, and E is the electric field across the depletion region given by:

$$E = \sqrt{\frac{2N_d(E_g - qV_{\text{actual}})}{\epsilon\epsilon_0}} \tag{2.3.22}$$

I_{bb} also encodes Zener breakdown, which is an increase in current resulting from a narrowing of the gap between the conduction and valence bands as the applied voltage increases. Since the potential difference between the conduction and valence bands of their respective regions is proportional to $V_0 - V_r$ and depletion width scales with the square root of this relation (Equation 2.2.10), the gap between the bands narrows more quickly and increases the probability of tunneling across the potential barrier (Figure 2.7).

In the trap assisted case,

$$I_{tb} = \frac{q^2m_{eff}n_tAV_{\text{actual}}M^2}{8\pi\hbar^3(E_g - E_t)}\exp\left(-\frac{4\sqrt{m_{eff}}E_g^{3/2}}{2\sqrt{2}qE\hbar}G(a)\right) \tag{2.3.23}$$

where E_t is the trap energy relative to the valence band, and n_t is the density of traps with that energy. $M^2 \approxeq 10^{-23}$ eV^{2}cm^3 is the mass matrix associated with the trap potential.[22, 10]

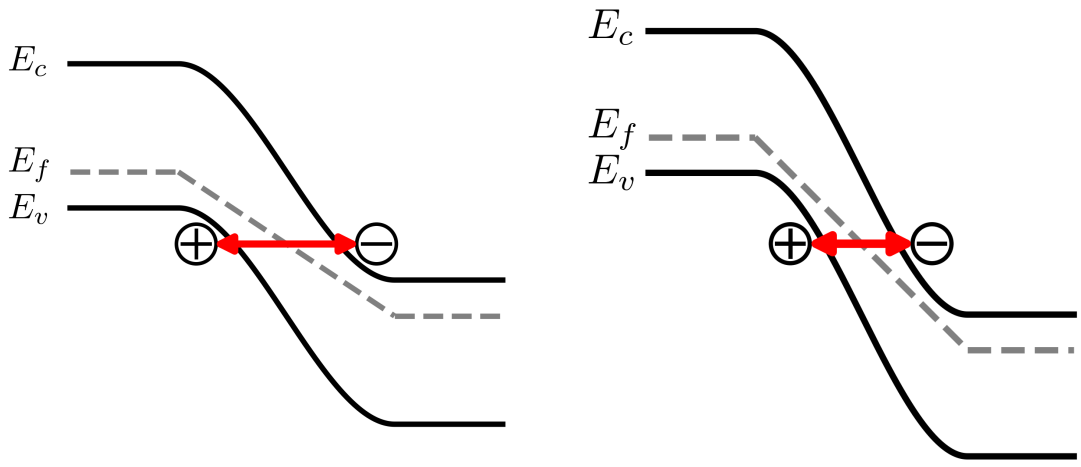

Figure 2.7: This figure compares band diagrams of a p-n junction under two different reverse-bias conditions. The left diagram corresponds to low reverse bias, while the right diagram corresponds to high reverse bias. The increased reverse bias reduces the effective tunneling distance across the gap and increases the probability of band-to-band tunneling.

$G(a)$ is a geometric factor:

$$G(a) = \frac{\pi}{2} - a(1 - a^2) - \text{asin}(a) \tag{2.3.24}$$

where a is a factor representing the trap location within the bandgap energy:

$$a = 2\frac{E_t}{E_g} - 1 \tag{2.3.25}$$

In V23, which has a high defect density n_t, I_{tb} dominates over I_{bb} by several orders of magnitude, despite the high reverse bias.

2.3.4 Surface Currents

The SATIN detectors are novel in part due to the growth method used to create them, which starts with a silicon wafer, buffer layers, and finally the HgCdTe material. The large lattice mismatch between the silicon and the buffer layers causes threading dislocations which propagate through the buffer layers and extend into the HgCdTe. After growth, most of the buffer

material is removed by selective etching, a step that—together with the presence of threading dislocations—produces surface defects that require passivation. Imperfect passivation results in surface currents, which can contribute significantly to the overall dark current. Following the work of Bacon[19], we model the surface currents as:

$$I_s = \frac{qAn_{is}s}{2} \tag{2.3.26}$$

where s is given by:

$$s = s_0 \frac{W_d}{\tau_s} \left[\exp\left(\frac{qV}{\beta k_b T} - 1 \right) \right] \tag{2.3.27}$$

where s_0 is a unitless velocity coefficient, τ_s is the lifetime of the surface states, W_d is the width of the depletion region, T is the temperature, q is the elementary charge, V is bias across the junction, and k_b is the Boltzmann constant. β is an ideality factor, and is also used to modify the usual n_i to n_{is}:

$$n_{is} = (5.585 - 3.820x + 1.753 \times 10^{-3} xT) \left[10^{14} {E_g}^{3/4} T^{3/2} \exp\left(-\frac{E_g}{\beta k_b T} \right) \right] \tag{2.3.28}$$

β is not the only variable that can be modified to affect the behavior of I_s, it is also possible to adjust the composition fraction x to affect it as well. Since the function describes the behavior of currents generated at the surface, it is probable that the material composition varies due to processing effects and the growth method. In the case of the V23, we find that $\beta = 3$ with an unmodified x is sufficient to support the findings in the data.

2.3.5 Rule-22

Analytical evaluation of the dark-current equations presented above is challenging and rarely yields results that fully capture the observed device behaviour. Consequently, most published studies of dark-current performance rely on parameterised fits rather than detailed physically based models. This situation is further complicated by the fact that detector manufacturers typically do not disclose the detailed doping profiles within the pixels, information that would be essential for rigorous modelling. Nevertheless, extensive characterisation efforts,

particularly those performed on Teledyne HgCdTe detectors, have produced a large and reliable dataset of dark-current measurements across a wide range of material and processing conditions.

"Rule-07", and later, "Rule-22", were defined as heuristic models to estimate the performance of a device based on a range of parameters.[24, 25] Rule-07 was created to accurately model the dark current of a pixel when the signal is dominated by the thermal generation of electrons, while Rule-22 is an update to it that extends the heuristic model to lower temperatures, where G-R and tunneling currents dominate. Zandian defines Rule-22 as a sum of functions, which individually model aspects of dark current generation: $J_{22} = J_1 + J_2 + J_3$. J_0 is a prefactor which forms the baseline function and roughly describes the performance of most devices:

$$J_0 = 10^7 \lambda^{-6.2} + 70\lambda^{1.08} \tag{2.3.29}$$

J_1 modifies the pre-factor to more accurately model devices which are limited by Auger-1 diffusion currents:

$$J_1 = J_0 \exp\left\{-\frac{1.2896q}{\lambda kT}\right\}. \tag{2.3.30}$$

J_2 describes the section of the Rule-22 curve where trap-assisted-tunneling currents are believed to dominate over Auger-1 diffusion for the best of Teledyne devices:

$$J_2 = 2 \times 10^{-10} J_0 \exp\left\{-\frac{0.4836q}{\lambda kT}\right\}. \tag{2.3.31}$$

The final term, J_3, describes the regime where dark current is believed to be limited by a poorly understood background flux, a portion of which is attributed to glow from the ROIC electronics:

$$J_3 = 1.5 \times 10^{-21} \lambda^2 T. \tag{2.3.32}$$

Combining these equations yields Rule-22:

$$J_{22} = \left(10^7 \lambda^{-6.2} + 70\lambda^{1.08}\right) \times \left(\exp\left\{-\frac{1.2896q}{\lambda kT}\right\} + 2 \times 10^{-10} \exp\left\{-\frac{0.4836q}{\lambda kT}\right\}\right) + 1.5 \times 10^{-21} \lambda^2 T \tag{2.3.33}$$

J_3 is chosen to model the relatively minimal glow that is present in state-of-the-art Teledyne devices, which have mitigation architectures for the glow. These primarily take the form of metallization layers between the ROIC and the substrate, which are designed to prevent emission from the readout nodes from reaching the detector bulk. Such layers significantly reduce the amount of radiation that reaches the detector bulk, as the primary throughput locations are only small gaps in the metallization layer that are left bare for the indium bump bonds.[7, 26, 27, 28] Unfortunately, such layers are not present in the SATIN devices, and as such the pixels are completely exposed to the underlying glow, which may contribute significantly to the noise floor. Regardless, Rule-22 provides a helpful point of reference for comparison to the SATIN data.

2.4 Theory of Persistence

Persistence, sometimes referred to as latency, is the phenomenon in which charge from a previous illumination continues to appear in subsequent frames or ramps even after the detector has been reset. In extreme cases the effect can persist for many hours or even days. As noted in the introduction, persistence resembles the afterimage observed in the human eye after exposure to a bright source. The effect has been documented since the earliest solid-state imaging arrays and has become a major concern for high-performance infrared detectors, particularly HgCdTe devices, over the past several decades.[29, 30, 31, 32]

The currently accepted model for persistence in modern HgCdTe detectors was proposed by Roger Smith in 2008.[33, 34] It attributes the dominant persistence mechanism to charge trapping at defect states within the p-n junction depletion region. During illumination the depletion region contracts, allowing photogenerated carriers to be captured by these traps. When the junction is subsequently reset to its full reverse bias, the depletion region expands again, but a fraction of the trapped carriers remains inside it. These carriers are then released on various timescales and are detected as signal in subsequent readouts. Figure 2.8 illustrates the process schematically. From top to bottom the subfigures show:

- **a**) a p-n junction after sufficient time under reverse bias for all traps to empty (hole

traps are denoted by squares, electron traps by circles);

- **b**) the junction after saturation by photogenerated charge (depletion region contracted);
- **c**) the junction immediately after reset (depletion region expanded, with trapped carriers remaining inside it);
- **d**) the gradual release of trapped carriers into the depletion region, where they are registered as apparent photocurrent in subsequent frames.

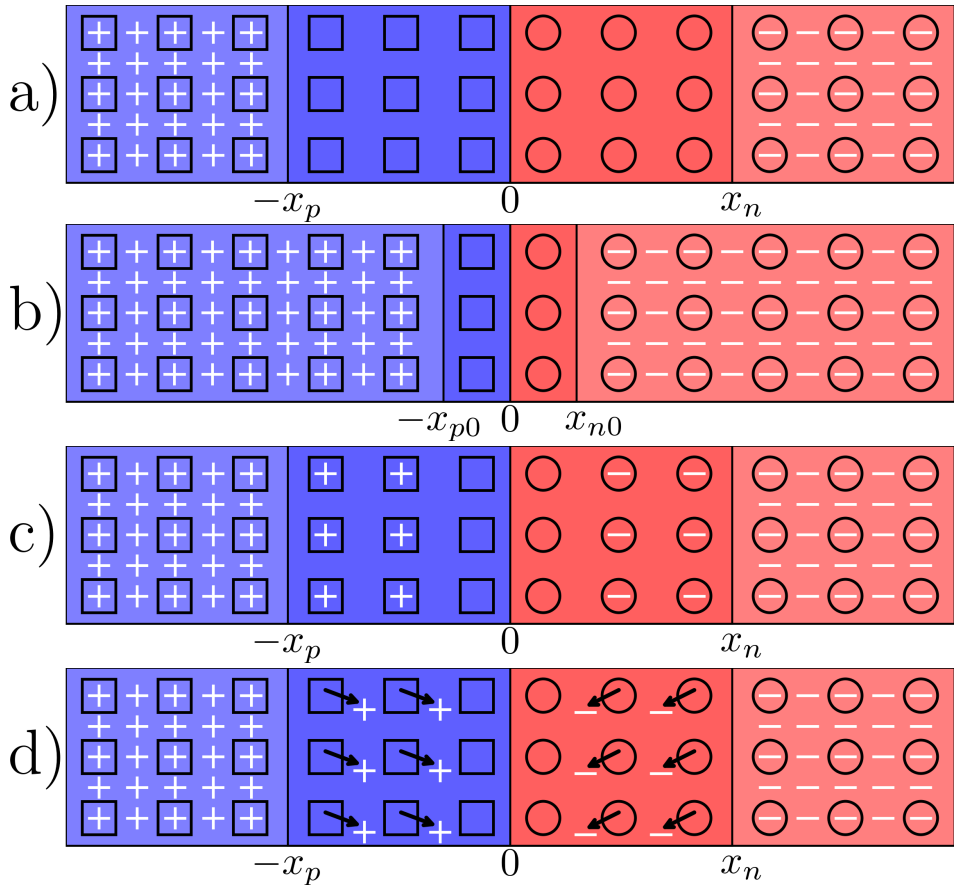

Figure 2.8: A schematic of persistence generation in a photodiode, where charge is trapped in fixed trap sites during charge integration, and released once the diode is reset for the next read.

The schematic representation in Figure 2.8 necessarily simplifies several important aspects of the trapping process. First, hole and electron traps are not confined to the p-type or

n-type regions, respectively; both types of trap can exist on either side of the junction. It is therefore possible for an electron–hole pair generated within the depletion region to be captured immediately by nearby traps on the same side before the carriers separate. Upon release these carriers follow the standard drift paths determined by the internal electric field. Second, the trapping and detrapping timescales vary widely from site to site, spanning many orders of magnitude. The quantity of charge ultimately trapped also depends strongly on the duration of the illumination period. Third, the spatial distribution of traps is far from uniform. Trap locations are governed by the underlying defect sources—threading dislocations, lattice impurities, and processing-induced defects—and therefore exhibit a semi-random distribution throughout the absorber volume.

The timescales for trapping and release have been discussed sparsely in the literature; One effective method for modeling the trap populations treats them as a sum of exponential functions.[35, 36] We define the amount of charge released in a persistence image $Q(t)$ as:

$$Q(t) = \sum_{n=1}^{n_{max}} N_n \left[1 - exp\left(\frac{-t}{\tau_n}\right)\right] \tag{2.4.34}$$

where N_n is the number of traps with trapping or detrapping time constant τ_n, n_{max} is the number of time constants, and t is the integration time of the exposure measuring persistence. By measuring the amount of charge $Q(t)$ released in a persistence image and adopting a set of reasonable values for the release time constants τ_n, the corresponding trap densities N_n can be determined.

Chapter 3

Characterization

Portions of this chapter are based on previously published works:

1. Buntic, Lazar, et al. 2024, *Advancing Large Format MCT/Si Infrared Detectors for Astrophysics Research*, SPIE Proceedings Volume 13103, DOI: 10.1117/12.3019111

2. Figer, Donald F., Buntic, Lazar, et al. 2022, *The SATIN Infrared Detector Development Program and the Road to HELLSTAR*, SPIE Proceedings Volume 12191, DOI: 10.1117/12.2627511

3.1 Pixel Masking

In order to properly characterize pixel behavior, we first have to reject anomalous pixels that would otherwise contaminate the data. In order to do so, we begin by identifying those anomalous pixels. Aside from the obvious, *i.e.* dead pixels (those that fail to integrate any charge) and hot pixels (those which are permanently saturated), a number of other behaviors were observed in the V23 data. Figure 3.1 shows a selection of pixels that exhibit those behaviors. The first two columns of plots were created using the same reference voltage but different gains, hence the pixels in the middle column reaching saturation in earlier frames. The third column of plots was created with an increased reference voltage, resulting in a slight non-linearity and quicker saturation. Among them are pixels that saturate early, exhibit significant non-linearity at low signal levels, reset to a level higher than the pixel nominally

should, or exhibit some combination of those effects. The signal plots in the top row of Figure 3.1 are for pixels that don't reset fully, one of which also exhibits a strong early non-linearity (purple) and one of which saturates early (light pink). The bottom row of plots shows a selection of well behaved (green) and hot pixels (red). Most of the hot pixels that are not instantaneously saturated upon reset exhibit increased signal gain at low signal level.

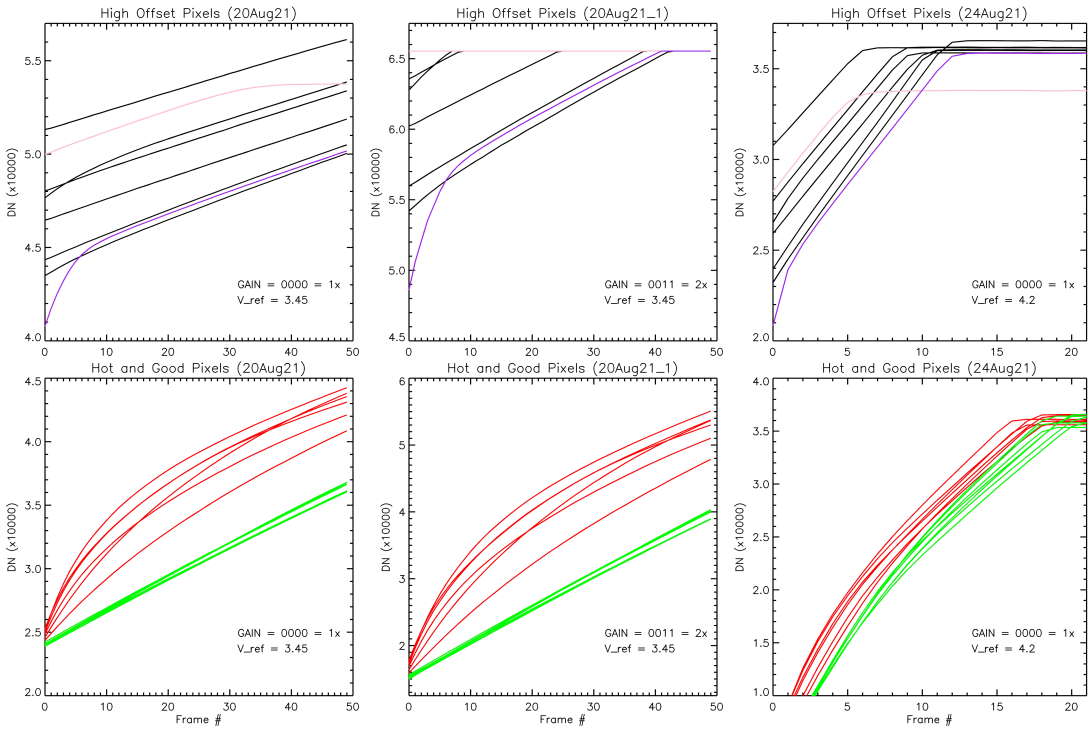

Figure 3.1: These plots show dark current plots for well behaved, linear pixels (green), hot pixels that exhibit nonlinear behavior (red), pixels that start at an abnormally high signal (black), high-offset pixels that saturate earlier than others (pink), and high-offset pixels that exhibit nonlinear behavior (purple.) Note the changes in electronic gain and reference voltage between columns of plots.

It is trivial to mask out the pixels that do not reset to the nominal level by doing a simple boolean search for pixels that have signal above a certain value in the first frame after the detector reset, which incidentally also masks out the pixels which are immediately saturated. In order to mask out the pixels that exhibit odd and non-linear behavior, we identify linear and nonlinear pixels by measuring the concavity of their signals versus time via the second derivative. We calculate the second derivative of the signal up the ramp for each pixel, and

reject all pixels whose second derivative has a standard deviation above a rejection threshold. Figure 3.2 shows two relevant plots. The first depicts the second derivative of pixel values through the test ramp, showing that the good pixels behave linearly, and thus have a constant second derivative. Pixels that do not have linear behavior produce the curves show in red. Taking the standard deviation of the second derivative (SDSD) has proven a simple and effective way to find the number of pixels that behave anomalously. The second plot shows the standard deviations of pixels in each quadrant, as well as the full array. Note that Q4 has the smallest tail, implying that it has fewest hot/nonlinear pixels, which is consistent with our dark current maps. Of the full array, 1.6% of the pixels have an SDSD$\geq$10. In Q4, only 0.8% of pixels have an SDSD$>$10, while nearly 2.6% of pixels in Q1 exceed this limit.

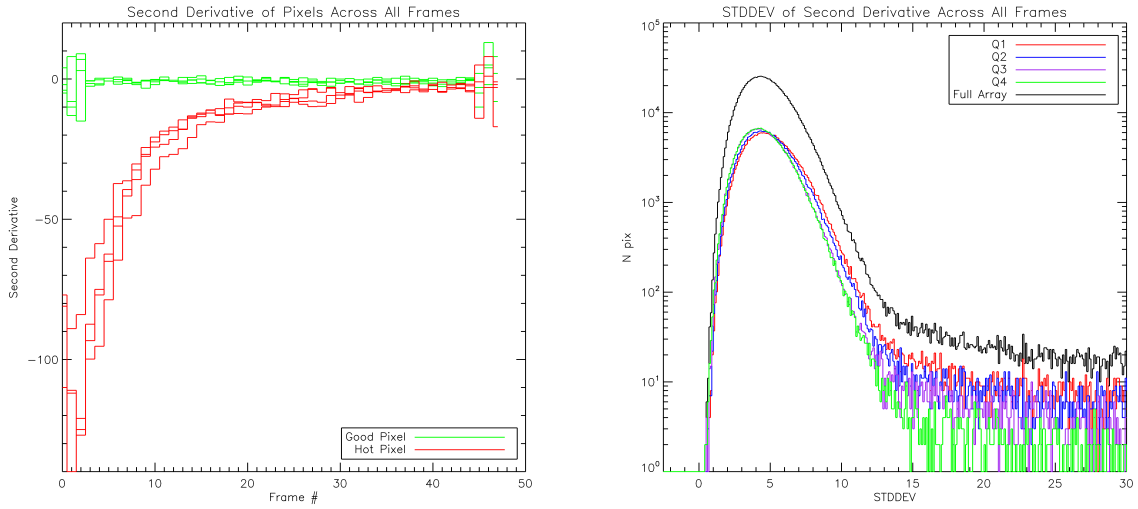

Figure 3.2: This figure presents two plots that show how we calculate the second derivative of the signal through a series of 50 frames for V23. Shown on the left are plots for a few good pixels (green), and hot pixels (red). Shown on the right are the standard deviations of pixel values in each quadrant; Note that the tail for Q4 is lower than the other quadrants.

3.2 Persistence

3.2.1 Experimental Methods for Persistence Testing

Three distinct experimental protocols were developed to characterize persistence in the SATIN detectors and thereby estimate the density of charge traps. The first protocol, designated the "leaveopen" test, continuously illuminates the detector with strong flux throughout a integration ramp to ensure that all accessible traps become filled. After this "soak" period the detector is reset and a sequence of dark frames is acquired to record the time-dependent release of trapped charge. Figure 3.3 illustrates the illumination and charge-collection timeline for this mode: the solid black line represents the total integrated signal during illumination, the dashed red line is the incident photon flux, and the solid red line is the latent charge released after reset.

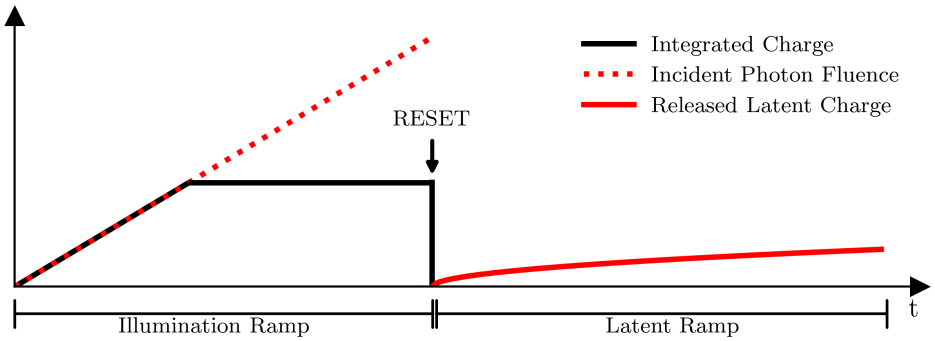

Figure 3.3: The figure illustrates the illumination and readout sequence used in the leaveopen persistence test protocol. The vertical axis and all features are schematic and not drawn to scale.

The second protocol, denoted "biasonly", eliminates optical illumination entirely. Instead, the reverse bias across the photodiode is reduced (or briefly made forward) to collapse the depletion region and allow carriers from the neutral regions to fill traps. In the measurements reported here the diode was forward-biased just sufficiently to eliminate the built-in depletion region. In all three protocols the duration of the period during which charge is available to fill traps is referred to as the soak time.

The third protocol, designated FWD%, operates as follows. The detector is illuminated to

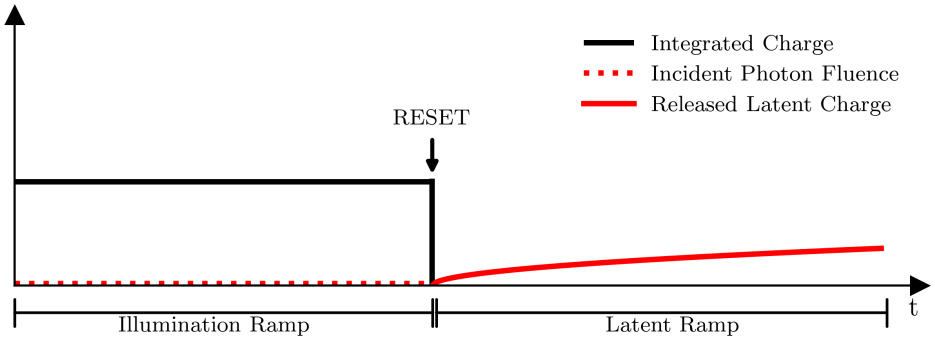

Figure 3.4: The figure illustrates the illumination and readout sequence used in the biasonly persistence test protocol. The vertical axis and all features are schematic and not drawn to scale. Note the lack of actual illumination, as all charge integration is achieved by bias manipulation.

a target fraction of full-well capacity within the first 15 s of the ramp. This level is then held constant for a controlled soak duration, after which the detector is reset and the subsequent persistence release ramp is acquired. The required photon flux is determined automatically at the start of each run. The control software iteratively adjusts the monochromator entrance-slit width and acquires short test exposures until the desired signal level is reached within the 15 s window.

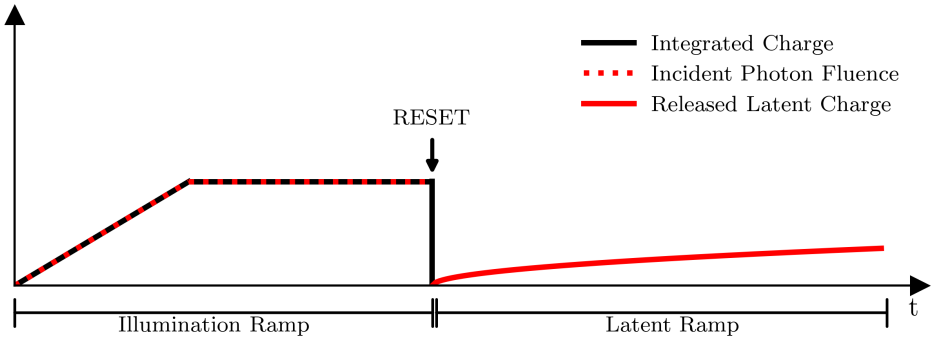

Figure 3.5: The figure illustrates the illumination and readout sequence used in the biasonly persistence test protocol. The vertical axis and all features are schematic and not drawn to scale. Note that the light source is shut off when the desired level of illumination is achieved.

The leaveopen and biasonly test modes were designed to serve essentially the same purpose: both supply the depletion region with a carrier population greatly exceeding the number of available traps, thereby ensuring near-complete trap filling. One important difference is that

the leaveopen protocol, by generating carriers throughout the entire absorber volume, can populate traps located outside the nominal depletion region (for example, near the backside surface) that the bias-only protocol cannot reach. This distinction is exploited later in the present section to discuss the spatial distribution of the dominant trapping sites within the pixel.

3.2.2 Variable-Integration-Time Readout Mode

A dedicated readout mode was implemented for the persistence measurements presented in this thesis. In this mode the integration time per frame increases progressively until a maximum value is reached, after which an arbitrary number of frames are acquired at that maximum integration time. A typical long ramp, for example, consisted of up-the-ramp (UTR) frames with integration times of 1, 2, 5, 10, 20, 50, 100, 200, and 500 s, followed by ten frames at 1000 s each. This variable-integration-time scheme enables total exposure times exceeding 10,000 s while retaining high temporal resolution during the critical early portion of the ramp—a resolution that would be lost in conventional constant-integration-time (fixed-duration) sampling. With fixed integration time the observer must choose between very few long frames (e.g., ten frames of 1000 s) or many short frames (e.g., 10,000 frames of 1 s); only the latter preserves early-time resolution, but it exceeds the memory capacity of the IDL 6.3 data-acquisition system used to store the raw frames before conversion to `.fits` format. The variable-integration-time mode therefore provides the necessary combination of long total exposure and fine initial sampling required for accurate fitting to Equation (2.4.34).

3.2.3 Persistence in V23

Persistence constitutes a major challenge in the characterization of dark current for the SATIN arrays. The standard dark current measurement protocol begins by fully rotating the filter wheels inside the dewar before closing them, a step that momentarily exposes the detector to infrared emission from the integrating sphere. This brief illumination fills a substantial number of charge traps. The subsequent release of trapped carriers contaminates the dark

ramps, producing an elevated signal in the first ramp that decays over successive ramps. For short-duration measurements the persistence signal exceeds the intrinsic dark current by significantly, and even experiments extending over tens of hours remain measurably affected by this contamination.

Figure 3.6 shows a map of persistence in the V23 detector, for the whole array and just Q4. Of all four quadrants, Q4 is the only one that exhibits highly localized clusters of pixels that have high persistence, while the other quadrants lack any such distinguishing features. The locations in the top-middle of the arrays that have high persistence are due to physical damage that the detector sustained during an observing run, and the dark cross-like feature in Q2 is not understood. Interestingly, the cross feature does not show up any other performance maps.

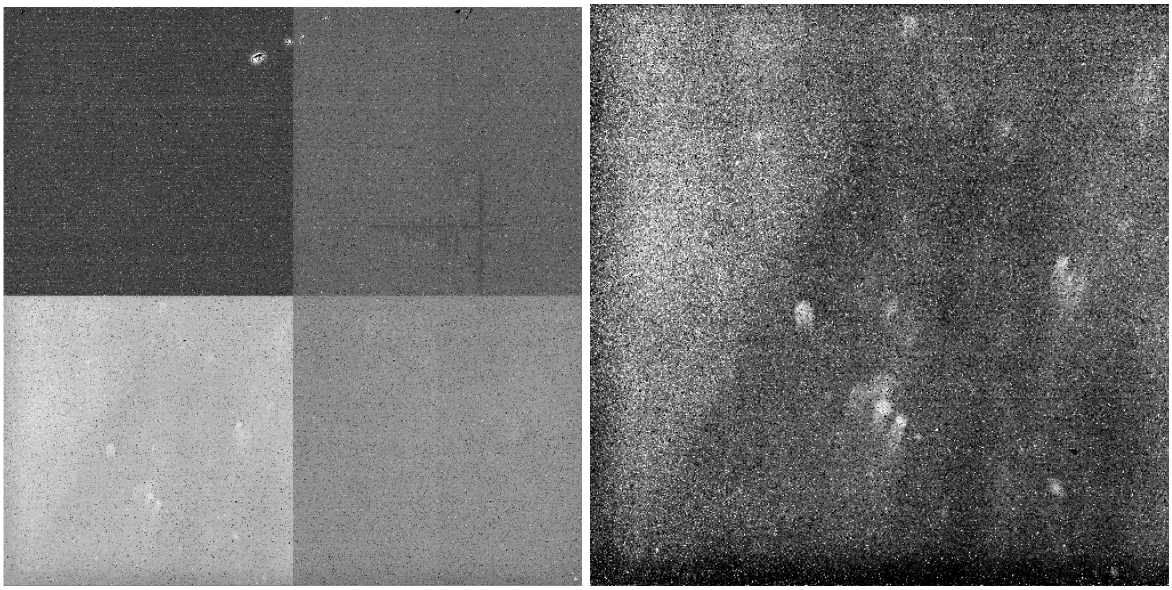

Figure 3.6: This figure shows two persistence maps for V23. On the left is the whole detector, while the one on the right shows Q4 with scaling and stretch to exacerbate the features within.

If the locations of traps were to be concentrated on the surface of the detector due to passivation issues and surface trapping, we would expect to see a morphological difference in the persistence maps for these two testing modes. As such, the latency data for the leaveopen and biasonly modes were inspected to determine if there were any differences in the persistence

maps. Figure 3.7 shows two maps of persistence in Q4: the latent data for the leaveopen mode on the left, and for the biasonly mode on the right. On first inspection, the only notable difference between the two images aside from the cosmic ray impact in the bottom right of the biasonly image is a dark spot on the left side of that image. This spot appears in both images and correlates to a physical defect in the detector, but is significantly more pronounced in the bias-manipulated data. It is unclear why only one of these dark spots would be disproportionately affected by the bias manipulation while the others are not, as is evidenced by Figure 3.8. That figure shows a difference image of the two modes on the left and a division of the leaveopen image by the biasonly one on the right. Aside from the defective spot, the difference image shows the same morphology as either dataset, as is expected if all of the trapping is occurring within the bulk of the detector and not near the surface. The ratio image is essentially flat, showing that the persistence in the illuminated image is higher by approximately 10% (10.7% mean, 10.4% median.)

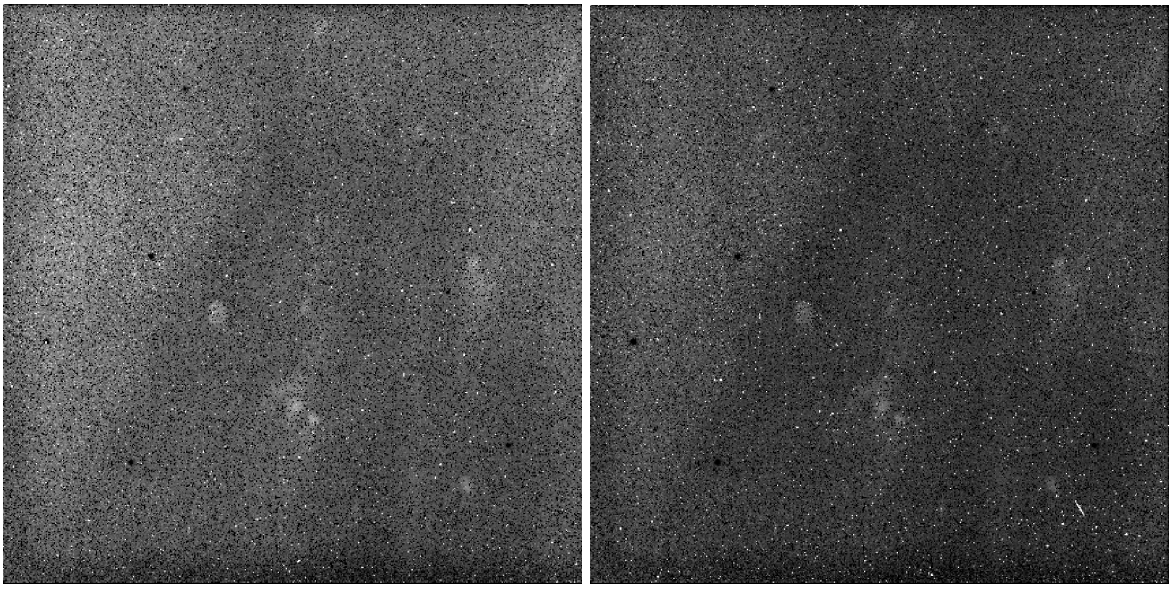

Figure 3.7: This figure shows two maps of persistence for Q4 of V23. On the left is persistence from the leaveopen test mode, on the right is persistence from the biasonly test mode.

Figures 3.9 and 3.10 present persistence decay curves measured in well-behaved pixels of Q4 using the leaveopen and biasonly exposure modes, respectively. In each figure the upper

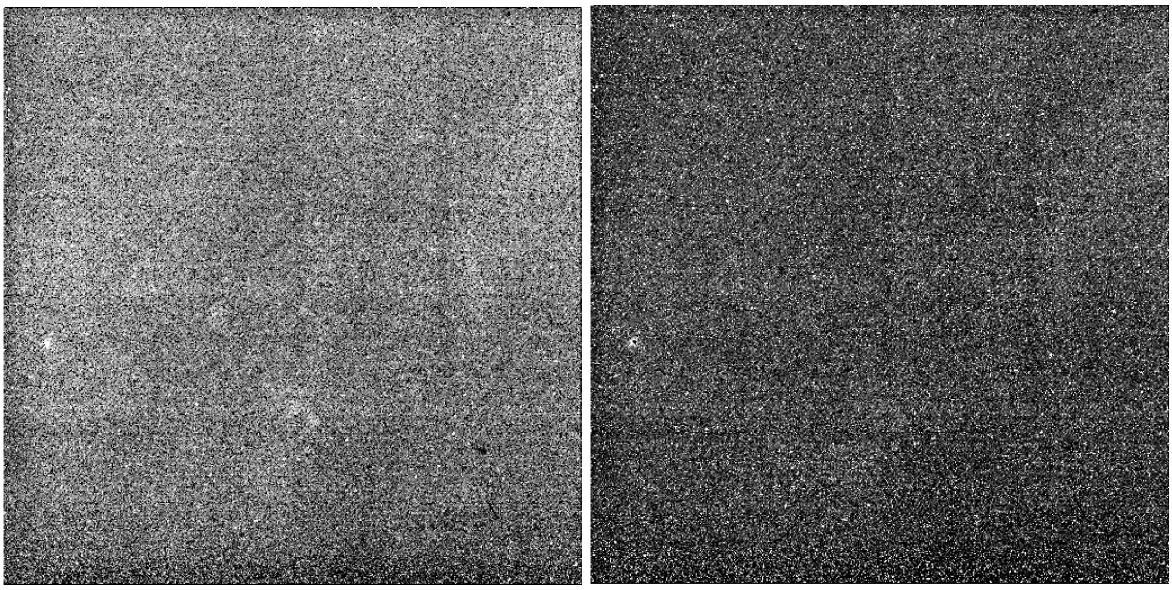

Figure 3.8: This figure shows two maps of persistence for Q4 of V23. On the left is a difference image made by subtracting the biasonly persistence from the leaveopen persistence. On the right is a map made by dividing the leaveopen data by that from the biasonly data.

panel displays the individual exponential components obtained from fitting Equation (2.4.34) together with their sum, while the lower panel shows the cumulative released charge as a function of time. The cumulative trace in the lower panel includes the contribution from the labeled time constant and all shorter time constants.

Table 3.1 lists the number of traps N_n derived for each time constant in both exposure modes. Previous studies of comparable detectors indicate that trap populations associated with different time constants are typically of similar magnitude. The noticeably lower N obtained for $\tau = 1\,\mathrm{s}$ is therefore an artifact of the measurement procedure: the first 1-second frame is subtracted from itself and all subsequent frames to remove reset-level variability, which necessarily discards a fraction of the charge released on the shortest timescale. A complementary excess in the longest time-constant bin is likewise attributed to a small population of traps with release times exceeding the $10^4\,\mathrm{s}$ duration of the present measurements.

The total charge released in the leaveopen protocol exceeds that measured in the biasonly protocol by approximately 12%. This excess demonstrates that optical illumination likely populates traps located outside the nominal depletion region—regions that remain inaccessible

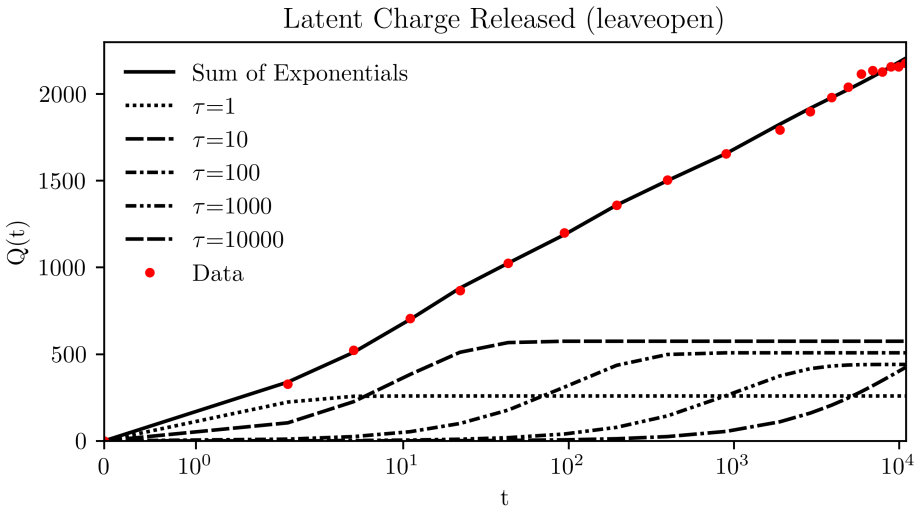

(a) This plot shows each of the fitted time constant functions for the data acquired via the leaveopen read mode, as well as their sum, shown as a solid black line.

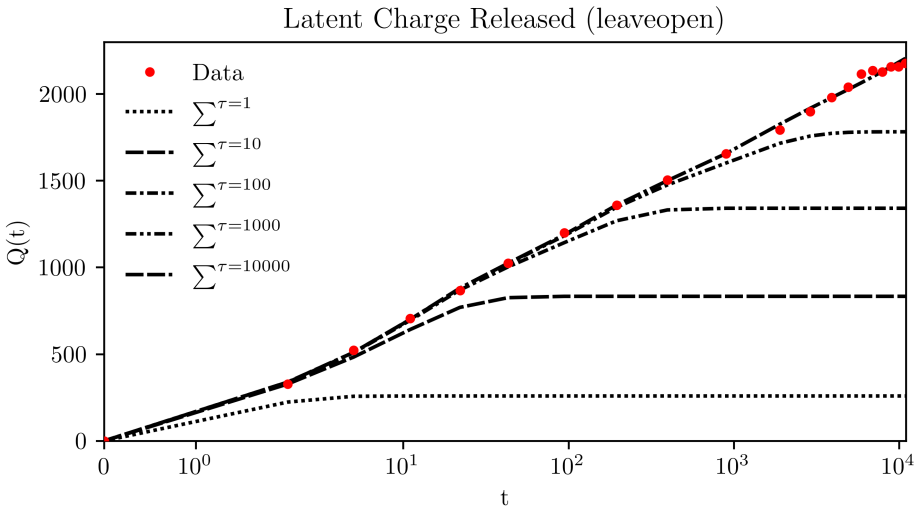

(b) This plot shows the cumulative sums of the fitted time constant functions for the data acquired via the leaveopen read mode.

Figure 3.9

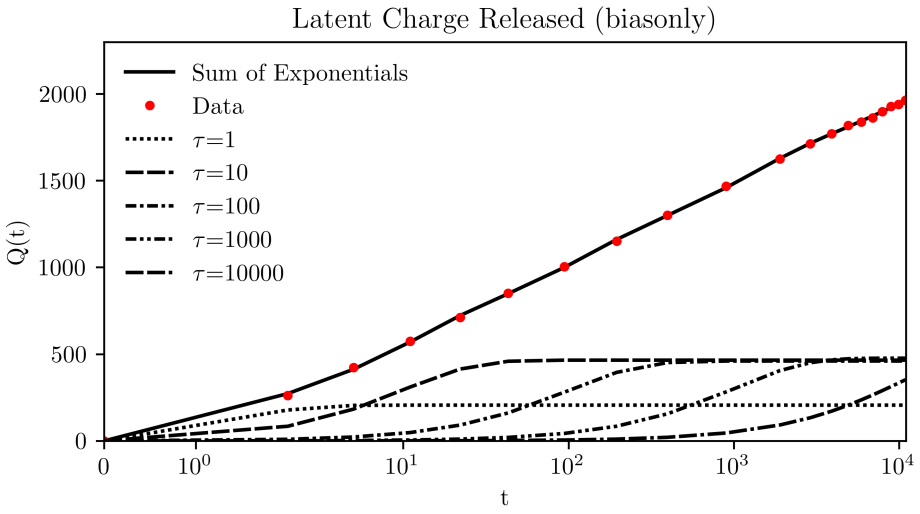

(a) This plot shows each of the fitted time constant functions for the data acquired via the biasonly read mode, as well as their sum, shown as a solid black line.

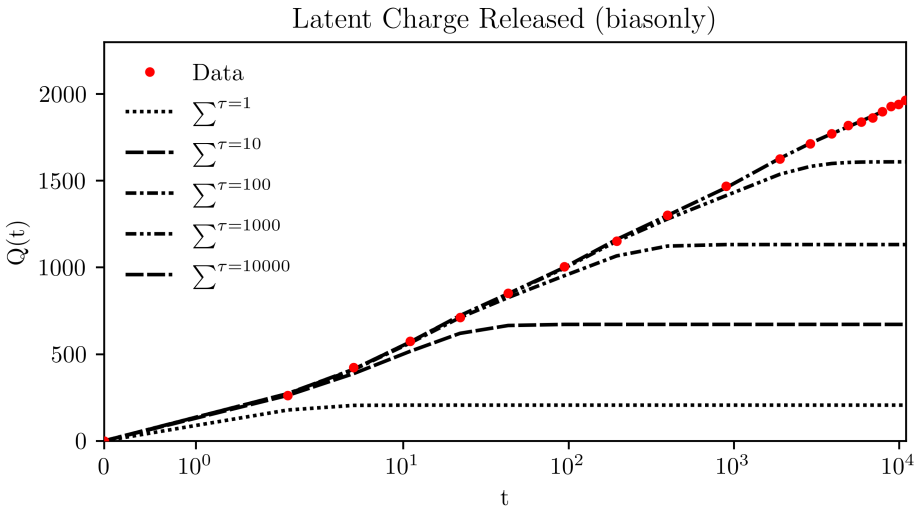

(b) This plot shows the cumulative sums of the fitted time constant functions for the data acquired via the biasonly read mode.

Figure 3.10

when charge is introduced solely by bias manipulation. Carriers released from these extra-depletion traps subsequently diffuse via random walk until they enter the depletion region, where the built-in field sweeps them to the collection junction and registers them as apparent photogenerated signal in later readouts.

	leaveopen	**biasonly**
τ	N_i	N_i
1	269	212
10	588	484
100	523	465
1000	432	470
10000	617	532
Sum:	2429	2163

Table 3.1: Fitting parameters for the chosen τ values to the released latent charge after the flooded and bias-manipulated exposure modes.

Figure 3.11 shows the increase in persistence signal as a function of pseudo-forward-bias magnitude during the charge-soak phase. The left panel corresponds to a 100 s soak time; the right panel corresponds to a 1000 s soak time. In each panel multiple latent-charge release curves are plotted, with each curve labeled by the value of the reset-gate voltage vrstUc applied during the preceding soak ramp.

Under nominal operating conditions the detector is reverse-biased by 1 V ($V_r = -1\,\mathrm{V}$), achieved by setting vrstUc = 0.002 V and vdetCom = 1.00 V (see Section 1.4.2). Positive values of vrstUc shown in Figure 3.11 therefore reduce the applied reverse bias during the soak period. After the soak ramp the detector is returned to its standard reset parameters, allowing previously filled traps to release their charge, which is subsequently recorded as persistence signal in the following readout sequence.

A direct comparison with persistence measurements reported for the state-of-the-art H4RG-10 detectors developed for the Nancy Grace Roman Space Telescope is instructive.[31] Although the test protocols differ, the Roman data provide a useful benchmark. In those measurements the detector was illuminated for 100 s at the end of a 600 s ramp, allowed to soak charge for a 60 s period, reset, and the released latent charge was quantified between 150 s and 300 s of the subsequent dark ramp. The median persistence signal reported with this protocol

is approximately 20 electrons (0.02% of the ≈100,000 electron full well depth).

The uppermost curve in the left panel of Figure 3.11 yields approximately 95 electrons of released charge over the same 150–300 s interval. This value is nearly five times higher than the Roman result. However, that difference surprisingly small given the larger V23 pixel area (20 μm versus 10 μm pitch), longer effective soak time, substantially higher defect density in the MCT-on-Si substrate, and full-well capacity at least four times larger than that of the H4RG-10 detectors. If threading dislocation density were the dominant source of persistence traps, a considerably larger increase would be anticipated. The relatively modest enhancement observed here therefore suggests that bulk material defects are not the sole driver of persistence in these arrays. Definitive conclusions, however, require more detailed comparative measurements and knowledge of the H4RG-10 junction implant geometry.

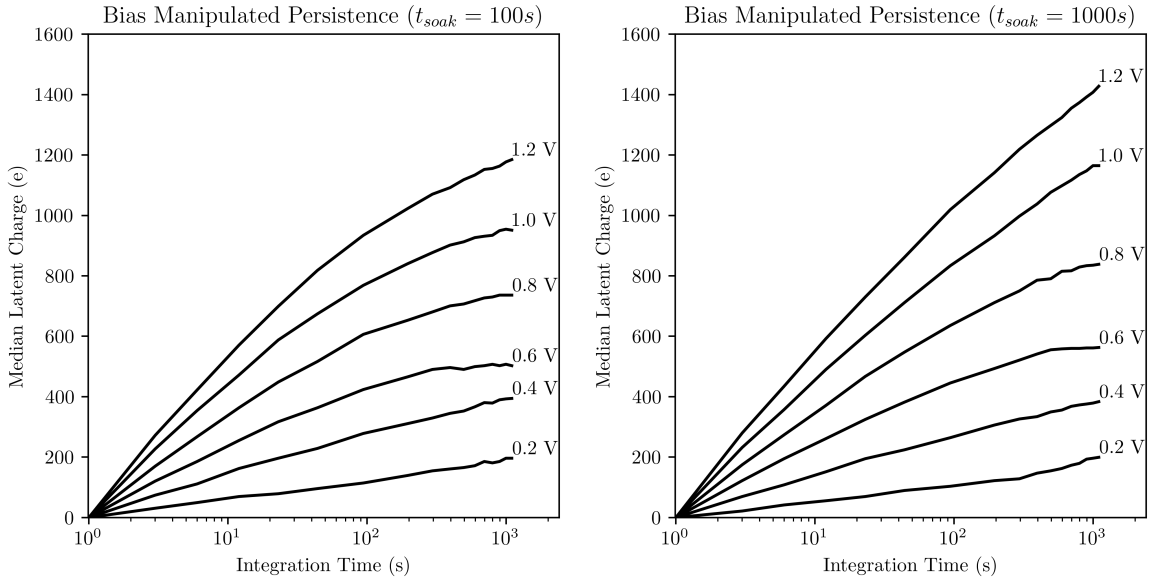

Figure 3.11: This figure shows two plots of biasonly persistence for Q4 of V23 across a large range of reverse biases, for soak times of 100 s and 1000 s respectively.

Figure 3.12 presents persistence release curves obtained using the FWD% test protocol with a fixed 1000 s soak time. Each curve corresponds to a different initial fill level of the pixel well, expressed as a percentage of full-well capacity and indicated by the label. After the illumination/soak phase the detector is reset (to nominal reverse bias), and the subsequent

latent-charge release ramp is recorded.

Table 3.2 summarizes the persistence measurements presented in Figure 3.12. The three rows list, respectively: (1) the illumination level expressed as a percentage of full-well capacity for the soak ramp, (2) the total number of electrons released during the subsequent persistence ramp, and (3) the released charge expressed as a percentage of the maximum observed value (1361 electrons, obtained at 100% illumination). The near-identical growth rates of rows 1 and 3 demonstrate that the total number of filled traps scales linearly with incident fluence.

Figure 3.13 shows vertical cross-sections through the persistence images of Figure 3.11 at selected times after reset. These profiles confirm that the magnitude of the released latent charge increases linearly with the total fluence delivered during the preceding illumination/soak phase. Taken together, the data in Table 3.2 and Figure 3.13 establish that trap occupancy in the SATIN detectors rises linearly with integrated illumination over the range examined. It is not clear why the data features a consistent droop at high integration times after the 0.6 V soaking ramps, or why there's an inverse effect for the 0.2 V data.

% of FWD	19.10	36.79	54.12	64.46	77.33	86.02	93.26	100.00
total released charge (e)	249.0	464.0	702.2	853.8	1039.4	1164.6	1265.2	1361.1
% of total released charge	18.30	34.09	51.59	62.73	76.36	85.57	92.95	100.00

Table 3.2: This table shows the amount of trapped charge released as a function of the percentage of the full well depth to which the detector was illuminated, and as a percentage of the total charge released in the most illuminated ramp.

3.3 Dark Current and Glow in V23

Accurate characterization and modeling of the dark current in V23 have been complicated by the absence of detailed doping concentrations and profiles from the manufacturer. The results of the measurements and the corresponding physical models are presented in this section.

3.3.1 Dark Current Characterization Read Modes

The V23 readout electronics support standard up-the-ramp (UTR) sampling. In this mode the array is reset once and then non-destructively read out a user-specified number of times.

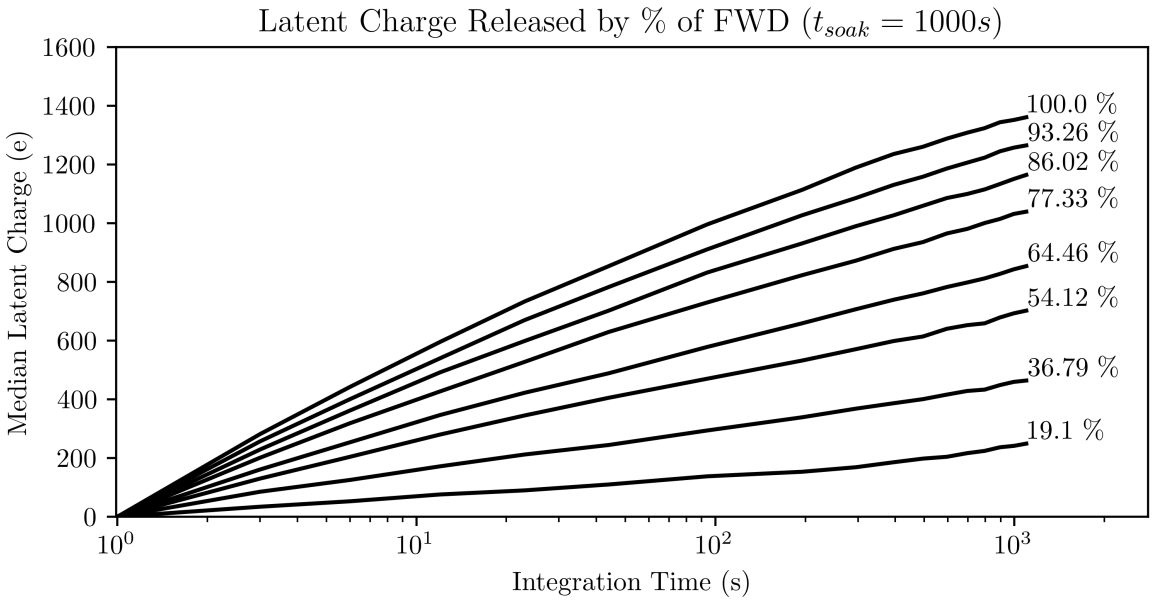

Figure 3.12: This figure shows a plot of persistence for Q4 of V23, taken after illuminating the detector a certain percentage of the full well depth.

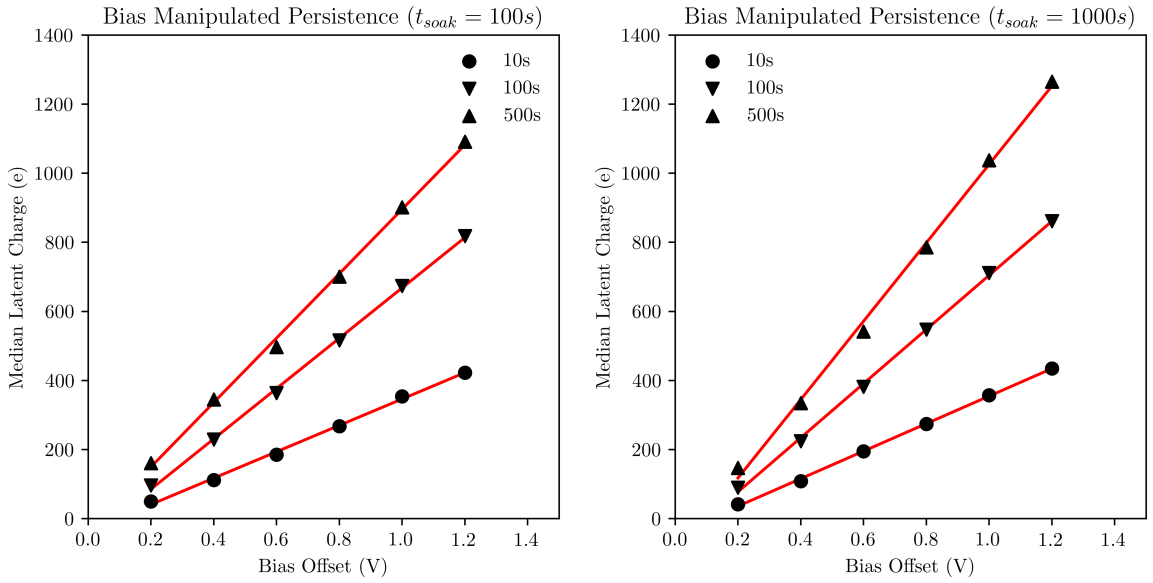

Figure 3.13: This figure shows cross-cuts of the persistence in Figure 3.11 at 10, 100, and 500 seconds.

Readout configurations are denoted UTR,X,Y,Z, where X is the total number of frames in the ramp, Y is the number of non-destructive reads performed per frame, and Z is the number of dropped (skipped) frame periods between successive saved frames.

The dropped-frame count Z directly controls the effective integration time per saved frame in multiples of the basic array readout period (0.9924 s). For example, a five-frame ramp with approximately 1 s integration per frame (no dropped frames) is executed as UTR,5,1,0. A five-frame ramp in which each frame (except the initial reference frame) integrates for 1000 s is executed as UTR,5,1,999.

3.3.2 Pixels Used in Dark Current Analysis

The pixels selected for the dark current analysis were chosen using objective performance criteria, specifically their isolation from hot pixels and the linearity of their response. Two independent masks were constructed and combined to exclude poorly performing pixels. The first mask eliminates all pixels that are either persistently hot or neighbor hot pixels. The second mask, derived from photon transfer measurements, excludes pixels exhibiting nonlinear or anomalously rapid charge accumulation (see Section 3.1). Application of the combined mask removes approximately 150,000 pixels from Q4, which contains 262,144 pixels in total. Because of the glow artifact present in the lower portion of the array (discussed below), only pixels in the top 50 rows of Q4 were retained. The final sample therefore consists of approximately 13,000 well-behaved pixels that display consistent and acceptable dark current characteristics.

Construction of the pixel masks revealed a clear correlation between defective-pixel fraction and junction implant area. Figure 3.14 presents two ratios for each of the four quadrants: the fraction of hot pixels N_h/N_q (black) and the ratio of implanted junction area to total pixel area $A_{\mathrm{junc}}/A_{\mathrm{pix}}$ (red). The nearly identical scaling of these two quantities indicates that the proximity of lattice defects to the p-n junction is a primary cause of anomalous pixel behavior, including elevated dark current. This relationship is well established in the literature for a wide variety of semiconductor photodiodes.[37, 38, 39, 40, 41]

Multiple studies report that defect densities below $10^5\,\mathrm{cm}^{-2}$ produce negligible impact

on photodiode performance, whereas state-of-the-art HxRG detectors achieve defect densities on the order of $10^4\,\mathrm{cm}^{-2}$ or lower.[40, 39] Although the exact defect density in the SATIN detectors cannot be disclosed (Raytheon proprietary), it is several orders of magnitude higher than $10^5\,\mathrm{cm}^{-2}$. This elevated defect density plays an important role in the discussion of the relative contributions of edge glow, source-follower glow, and trap-assisted tunneling to the measured dark current in Section 3.3.7.

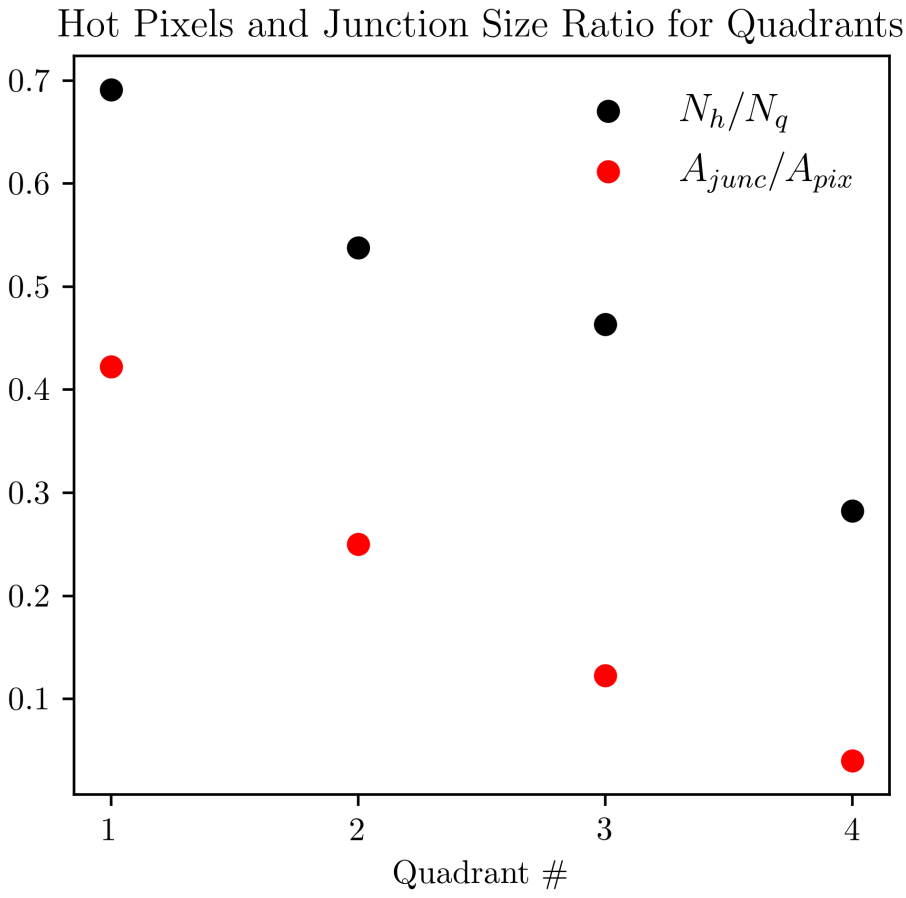

Figure 3.14: This figure presents the fraction of hot pixels N_h/N_q (black) and the geometric fill factor $A_{\mathrm{junc}}/A_{\mathrm{pix}}$ (red) for each of the four quadrants of detector V23.

3.3.3 Glow Background

Glow is an electroluminescence phenomenon that increases the background signal in modern infrared detectors. In detector systems it typically originates from photon emission by the

readout integrated circuit (ROIC) itself.[42, 32, 43, 7, 44] The earliest observation of light emission from a semiconductor diode was reported by Henry Round in 1907, who noted visible luminescence from a silicon carbide crystal under applied voltage. Oleg Losev subsequently demonstrated in the 1924 that the emission from SiC junctions was not thermal in origin. The first quantitative explanation for glow in p-n junctions was provided by Kurt Lehovec in 1951, who attributed it to carriers injected across a forward-biased junction.[45, 46]

Several models have since been proposed to describe ROIC glow in infrared arrays. Tam and Hu attributed the emission primarily to bremsstrahlung from hot carriers accelerated in high electric fields.[47] Bude et al. and Carbone et al. predicted peak photon energies in the 0.5–1 eV range.[48, 49] Stellari et al. developed a probabilistic model for photon emission from MOSFET channels that depends on electric-field strength and carrier density.[50] Maestre et al. directly imaged source-follower glow using an infrared EMCCD camera.[51, 7] The most comprehensive study of glow in HgCdTe detectors remains that of Regan and Bergeron, who showed that, at cryogenic temperatures, essentially all measured dark current in H2RG devices originates from multiplexer glow. They demonstrated correlations between glow intensity and frame rate, number of samples per ramp, and detector cutoff wavelength—the last providing support for the hot-carrier bremsstrahlung mechanism of Tam and Hu.

3.3.4 Sources of Glow

While multiplexer glow is not a completely understood phenomenon, there have been a number of efforts to characterize it in various systems and determine which elements of the circuitry generate it. Of the possible sources of glow, three have been identified in the literature. The first has a drastic effect, and is associated with the clocking circuitry of the ROIC. Overshoot on the clock lines is known to cause glow for these types of IR devices, as it activates diode protection circuitry on the ROIC that heat up and cause infrared emission.[52] The left image in Figure 3.15 shows this type of glow in V23.

The second glow component arises from the column-selection and output-amplifier circuitry located along the bottom edge of the array. This source produces a pronounced gradient that

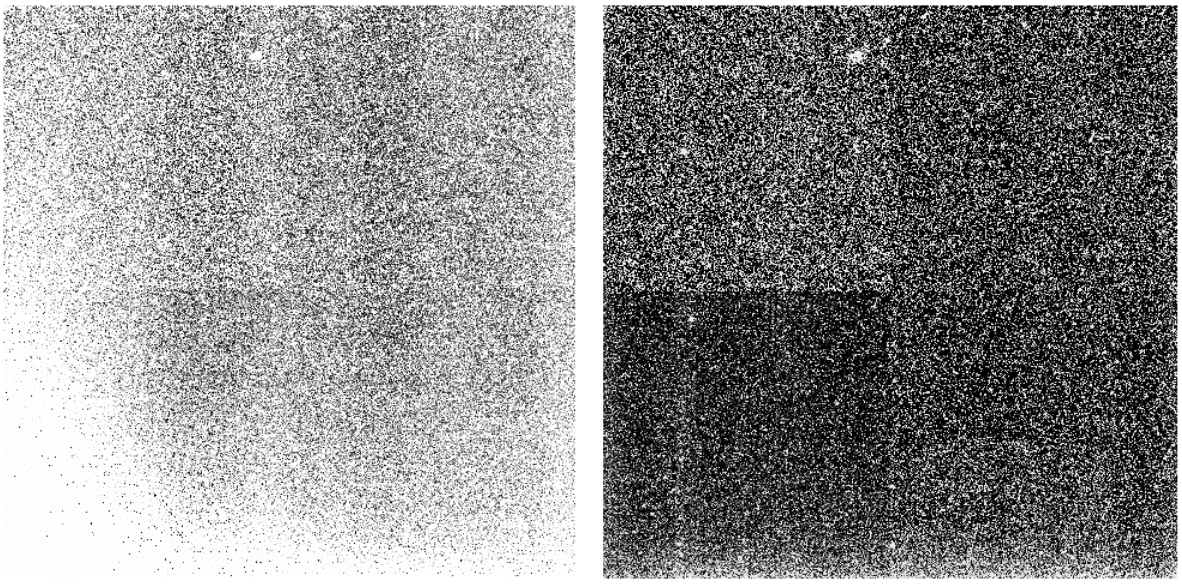

Figure 3.15: This figure shows two dark current slope maps of V23. The scale on both images is drawn such that black represents a pixel slope of 0 e/s and white 0.2 e/s. The image on the left is from data generated without additional resistance in the clock lines, and the image on the right is data taken with an additional 100 ohms on the pixel master clock (PMC) and frame start clock (FSC).

increases toward the amplifiers, as seen in the right panel of Figure 3.15.[4, 42, 43] Figure 3.16a displays the median pixel value per row for quadrants Q4 and Q1, extending from the bottom of Q4 to the top of Q1. The gradient is evident in Q4 and appears to continue into Q1, although the signal-to-noise ratio in Q1 is insufficient for reliable fitting owing to the limited number of well-behaved pixels.

An exponential-plus-constant fit to the Q4 median row profile is presented in Figure 3.16b. The constant term corresponds to the spatially uniform dark current contribution, which includes intrinsic detector dark current plus any glow emitted by the in-pixel source-follower transistors (whether readout-dependent or steady-state thermal emission). The exponential term represents the distance-dependent glow from the column/output circuitry at the array edge.

The third glow component arises from within the individual pixel unit cell and is generally attributed to the in-pixel source-follower transistor.[43, 51, 7] One method to separate the glow

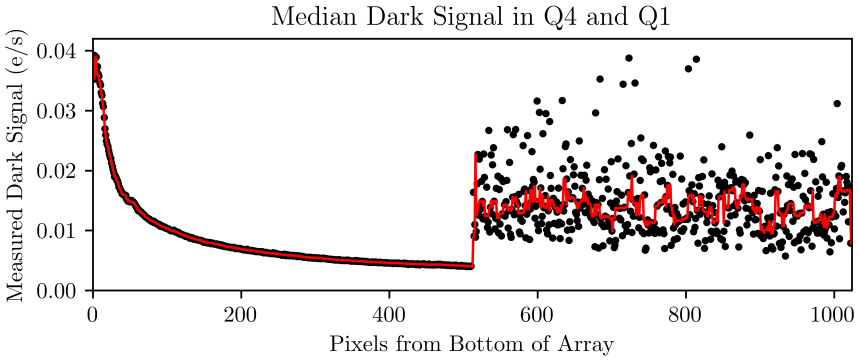

(a)

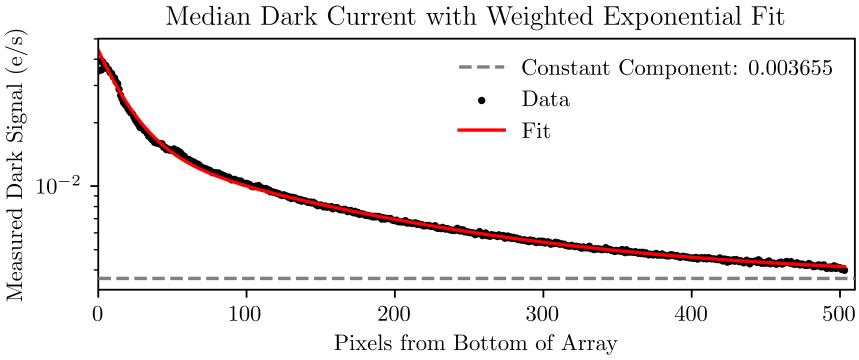

(b)

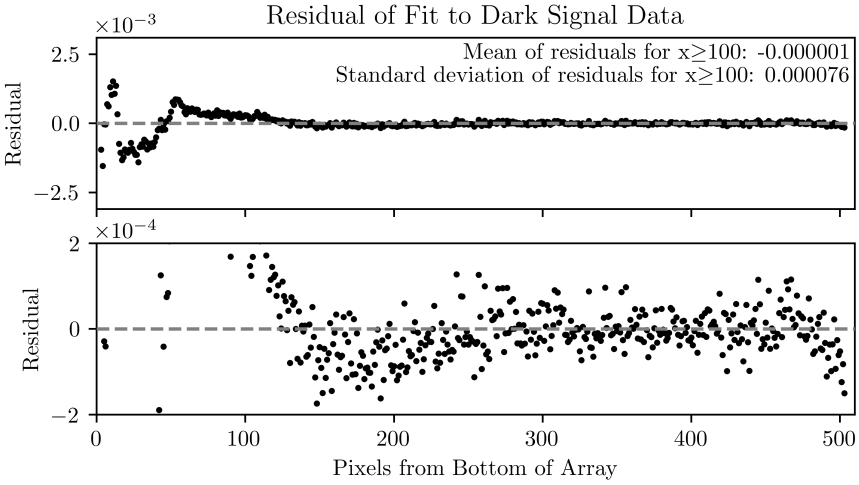

(c)

Figure 3.16: The top panel of this figure displays the median signal per row across quadrants Q4 and Q1, showing the glow-induced gradient that increases toward the column/output circuitry at the bottom of the array. An exponential-plus-constant fit to the Q4 data is overlaid as a solid curve in the middle panel, and the fit residuals are presented in the bottom panel.

that occurs from reading out each frame from the actual dark current of the pixel is to perform fitting on multiple sets of data which use increasingly more sparsely sampled frames.[43] The electronics used for our experiments allow for the implementation of 'dropped' frames, which is a wait time during which no clocking is sent to the detector chip. In the idealized case, the detector should not accumulate any charge aside from the actual dark current during these dropped frames. We attempt to generate maps of the dark current and per-frame glow components by taking three datasets of equivalent total integration time (t≈100 s): a) UTR,100,1,0 b) UTR,34,1,2 and c) UTR,12,1,9. For each ramp type we take 30 sets of ramps, subtract the first frame of the ramp to remove the reset effects, average the results of the last 20 sets, and then perform fitting of the results using:

$$S_{\text{total}} = \frac{S_{\text{PFG}} X}{t} + S_D \tag{3.3.1}$$

where S_{total} is the total signal of the pixel, S_{PFG} is the signal from per-frame glow, X is the total number of frames (reads) in the ramp, t is the integration time, and S_D is the signal from the dark current component.

Fitting this to the data and solving for S_D and S_{PFG} yields the two maps shown in Figure 3.17. Of particular note is the presence of increased current at the bottom of the array even in the dark current map, likely due to persistence from the signal introduced by per-frame glow. Unfortunately, the convolution of noise sources (actual dark current, edge glow, persistence from the glow, source follower glow, etc) makes it so this simple model is insufficient to accurately separate the dark current and per-frame glow components. The median value of the best Q4 pixels selected for this analysis in S_D is an order of magnitude higher than the actual dark current, and a number of pixels carry negative values. Similarly, the per-frame glow values are too high, and would result in dark currents far higher than what we measure in our devices. Attempts to refine the model to include these factor were fruitless, as were all attempts to improve the input data (more frames, longer exposures, more datasets, using only datasets with frame times longer than 10 seconds, etc).

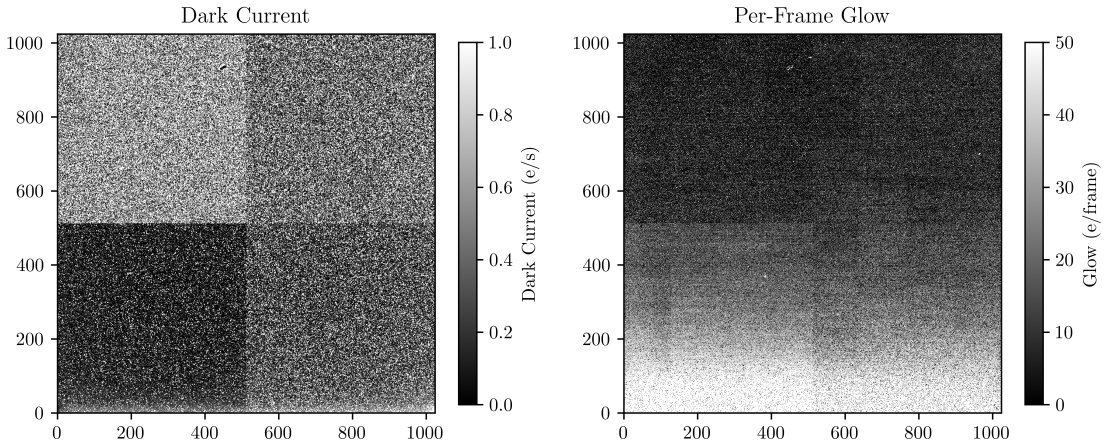

Figure 3.17: This figure shows maps of dark current and per-frame glow for V23.

3.3.5 Mitigating Glow

The prominent clocking-overshoot glow component in detector V23 can be suppressed by two independent methods. The first method reduces the clock power-supply voltage CLKPWR, thereby decreasing the overshoot amplitude, which scales with the applied voltage. The second method inserts series resistance into the clock lines, damping the ringing and preventing the overshoot from activating the ROIC protection diodes. Adding sufficient series resistance eliminated this glow contribution entirely: beyond approximately 20 Ω the overshoot no longer triggered electroluminescence, and further resistance produced no additional reduction.

Figure 3.18 presents oscilloscope traces of the frame-start clock (FSC) and pixel-master clock (PMC) with and without added series resistance. The left panel shows the large ringing present without resistance; the right panel shows the effectively damped waveforms obtained with 100 Ω of added resistance on each line.

Modifying CLKPWR was shown to be effective, but unnecessary when sufficient resistance is added to the clock lines. Figure 3.19 shows two plots: The left panel plots measured glow intensity versus CLKPWR voltage, both with and without added clock-line resistance. The right panel plots glow intensity versus added series resistance, demonstrating saturation of the suppression effect above approximately 20 Ω.

The persistent glow at the bottom of the detector has proven much harder to mitigate.

Figure 3.18: This figure shows two oscilloscope measurements of clock ringing in V23. The image on the left is generated without additional resistance in the clock lines (PMC, yellow; FSC, green), and the image on the right is data taken with an additional 100 ohms on the PMC (yellow) and FSC (green).

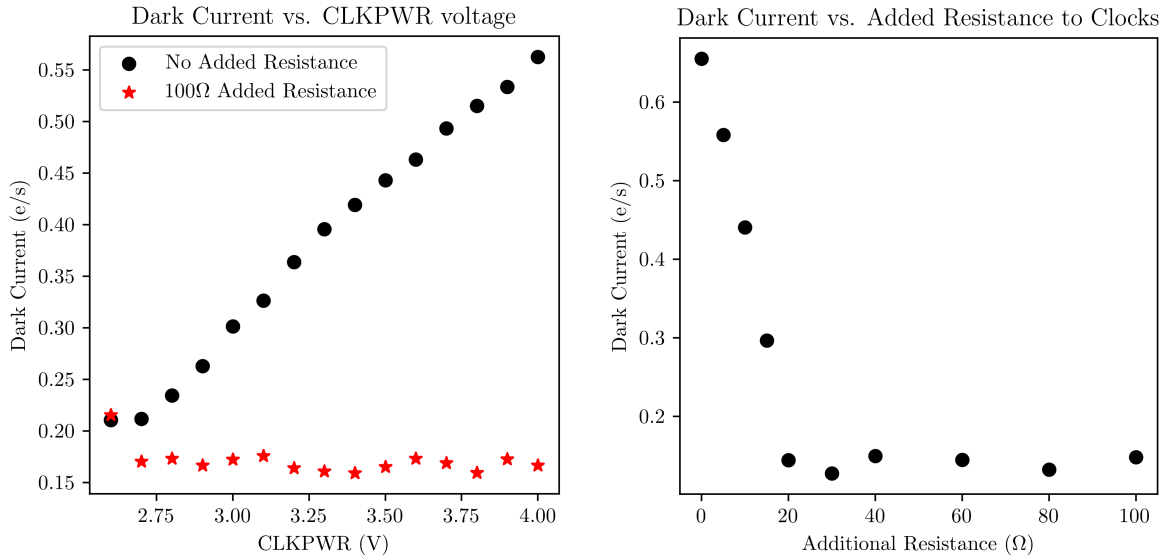

Figure 3.19: This figure shows two plots; On the left, the median measured dark signal is shown as a function of the CLKPWR voltage, with and without added clock line resistance. On the right, the plot shows a decrease in dark current with added clock resistance at a constant CLKPWR voltage.

Literature on glow reduction in the HxRG family of detectors has shown that changing certain voltages, such as increasing the drain voltage on the output buffers, can significantly reduce the edge glow, albeit with significant diminishing returns as the drain voltage rises.[44] However, testing this effect in the VIRGO ROIC (*e.g.* by modulating vnOut, see Figure 1.3) has not yielded improvements in the edge glow.

3.3.6 Dark Current and Glow as a Function of Sampling Rate

Two types of up-the-ramp read modes were used for the majority of the testing. The first read mode uses continuous 'fast' sampling and is heavily dominated by glow. The fast mode continuously reads out frame after frame, and is the default operating mode of the device. For the dark current data labeled 'fast', we use UTR,65,1,0, and for the data labeled 'sparse' we use UTR 35,1,999. Figure 3.20 shows two histograms of the dark current, for the fast and sparse dark current modes. The measured dark current for this population of pixels when sampled is invariant with respect to the number of frames in a ramp, so long as the frame integration time remains constant.

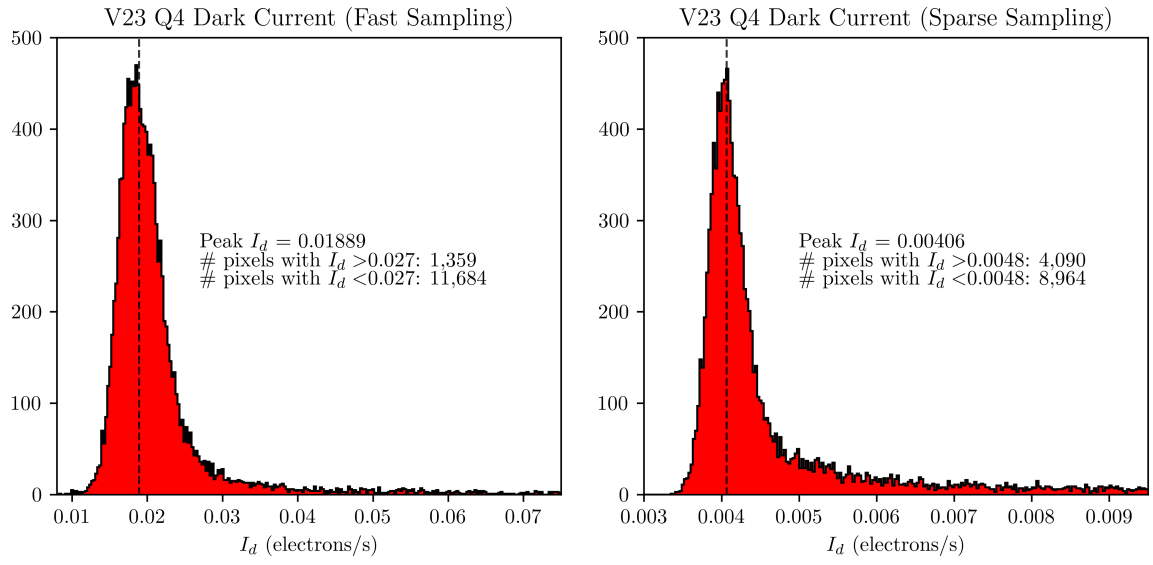

Figure 3.20: This figure shows two dark current histograms for V23. On the left is one taken for continuously sampled UTR frames, while the one on the right shows dark current for UTR frames with 1000 s integration times.

The histograms reveal two important features. First, reducing the readout sampling density decreases the median dark current by a factor of approximately 5. Second, the high-current tail of the distribution becomes considerably more populated in the sparsely sampled data.

Each distribution was fitted with a Gaussian function near its peak. The number of pixels lying beyond $\mu+3\sigma$ is indicated on the plots; the sparsely sampled dataset contains nearly three times as many pixels in this tail as the densely sampled dataset. This marked increase in the tail population indicates that the intrinsic pixel-to-pixel dark current variation is substantially larger than apparent in high-sampling-rate measurements, where per-read multiplexer glow dominates the signal and masks the true tail. By reducing the glow contribution through sparser sampling, the underlying dark current distribution of the detector array is uncovered, revealing a significant number of pixels with elevated dark current that are otherwise obscured.

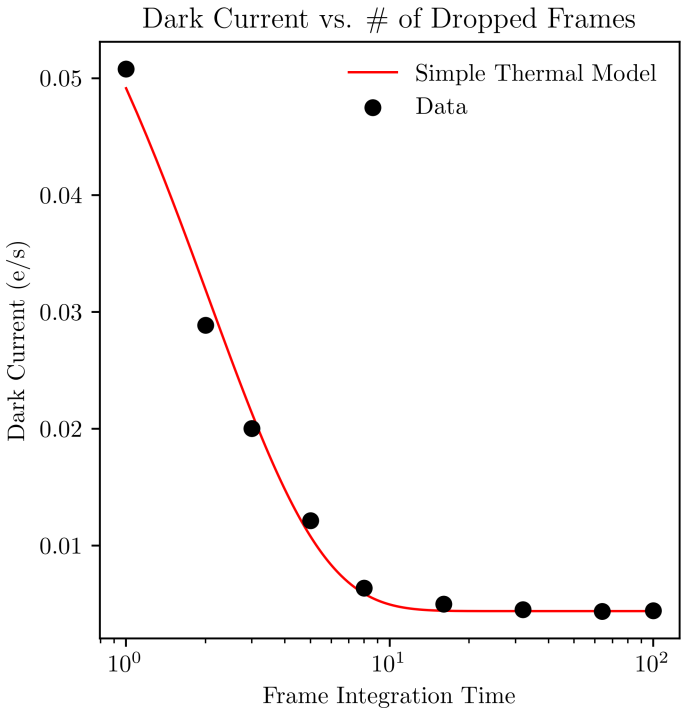

Figure 3.21: This figure shows how measured dark current decreases as the frame integration time increases.

Figure 3.21 shows the measured dark current as a function of frame integration time over the range 1–64 s. Each point represents the median measured dark current for a 65-frame

ramp. The observed decrease with longer integration time provides insight into the origin of the edge glow component that arises from the column circuitry at the bottom of the array. The functional form of the curve indicates that this glow is primarily thermal in nature: the ROIC column electronics do not fully return to equilibrium temperature between successive read cycles. Consequently, the steady-state temperature reached during the available cooling interval (equal to the frame integration time) governs the magnitude of the thermally induced glow.

A simple thermal relaxation model is overlaid in red on Figure 3.21. The model assumes an initial temperature rise upon readout followed by exponential cooling with an adjustable time constant and amplitude; it reproduces the observed trend without requiring detailed knowledge of the circuitry. The simple model is shown in Equation 3.3.2:

$$T_s = T_i \exp\left(\frac{-\alpha t}{\tau}\right) + \beta \tag{3.3.2}$$

where T_s is the temperature to which the readout circuitry settles after initial heating by T_i degrees, t is the integration time, τ is a cooling timescale factor, and α and β are arbitrary constants chosen to align the model with the data above. The model presented here is deliberately simplified. It demonstrates only that a basic thermal-relaxation description can reproduce the observed dependence of edge-glow intensity on frame integration time. A comprehensive physical model, constructed with detailed knowledge of the ROIC layout, power-dissipation sites, and three-dimensional optical propagation paths, would be required to quantitatively account for the spatial gradient across the array and the partial absorption or scattering of emitted photons by intervening structures.

3.3.7 Dark Current Temperature Dependence

Figure 3.22 presents an Arrhenius plot of the measured dark current for the nominal pixel population in Q4 of V23. The plot displays the individual contributions from each major dark current mechanism discussed in Section 2.3, the Rule-22 prediction (adjusted for our detector parameters), and the sum of all mechanisms. Because the manufacturer does not

disclose detailed device parameters (doping concentrations and profiles, defect densities, absorber thickness, etc.), the theoretical curves were calculated using the best available estimates derived from published literature, historical program documentation, and engineering correspondence.

The edge-glow component (orange), previously isolated as the difference between the exponential term and constant component in the gradient fit of Figure 3.16, is included in the Arrhenius plot. This distance-dependent contribution establishes a lower bound on the fraction of measured dark current originating from the column/output circuitry at the bottom of the array. For the pixel population analyzed here, edge glow accounts for at least 10% of the total dark current at the lowest temperatures, corresponding to approximately 0.0004 e/s out of the measured 0.0040 e/s.

One unresolved question concerns the contribution from thermal emission by the in-pixel source-follower transistor. In more mature Teledyne HxRG detectors, multiplexer glow generated within the pixel itself has been shown to dominate the dark current even when extensive mitigation techniques (including opaque metal shielding layers) are employed.[43] Mitigation strategies shown to be effective for the HxRG series—modulation of the source-follower drain voltage and increased pixel clocking speed to reduce current flow duration through the transistor—were tested on the SATIN detectors, yet produced no measurable reduction in dark current.[7] Given the elevated defect density of the SATIN HgCdTe material and the absence of any observable response to source-follower operating conditions, trap-assisted tunneling must be the primary remaining contributor to the measured dark current floor.

3.4 Crosstalk

Crosstalk is a phenomenon where neighboring pixels in an array exhibit a coupling of signal between them. Crosstalk can be caused by many mechanisms, but the simplest form can be imagined as charge being generated in one pixel and being captured by a neighboring one. It is a charge diffusion process described by random walk of electrons, weighted by the electric field within the pixel. The term random walk was first defined by Karl Pearson in 1905.[53]

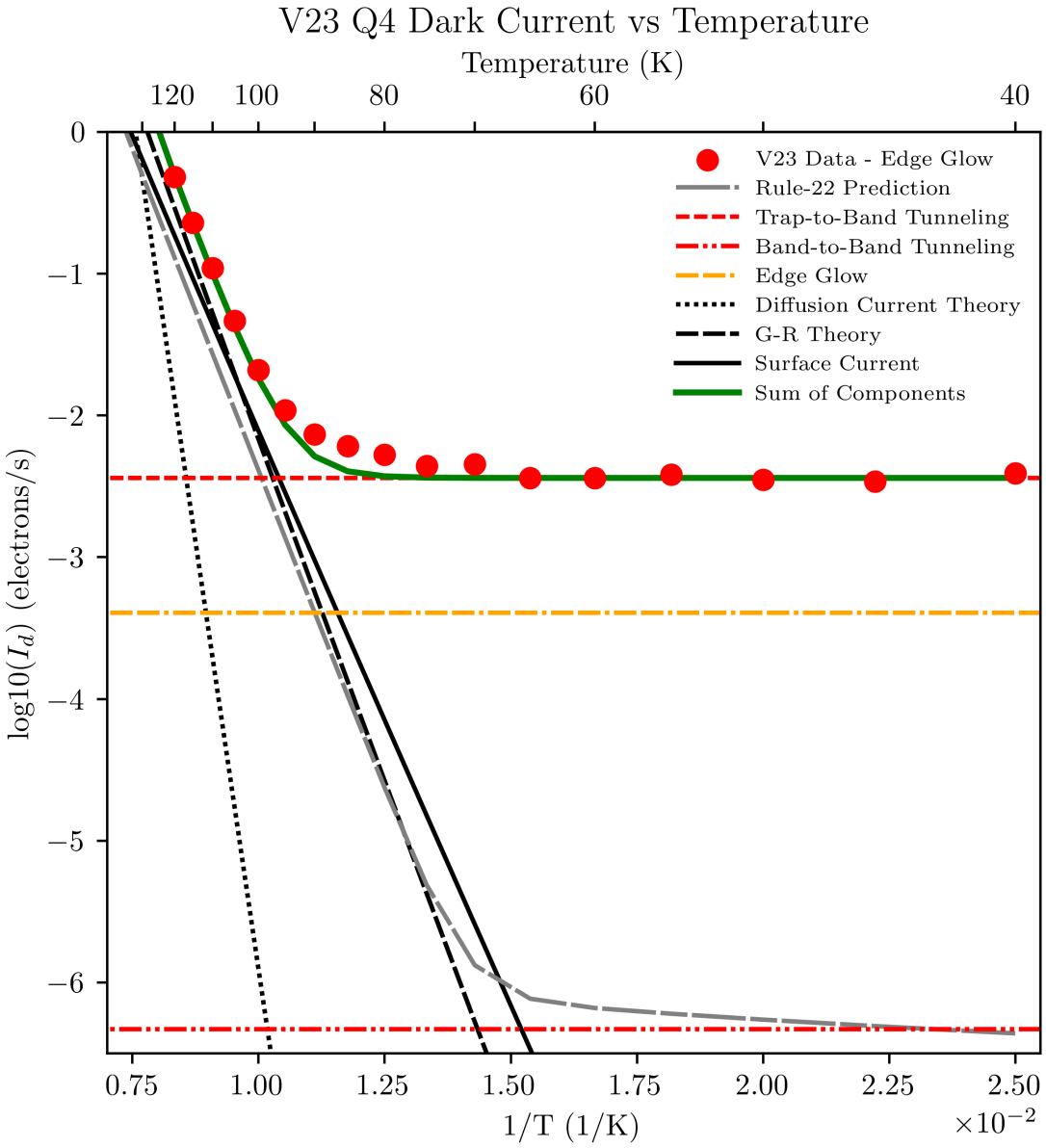

Figure 3.22: This figure shows the dark current as a function of temperature for Q4 of V23. The black lines show the components that come from diffusion, G-R, and surface currents, the red lines show contributions from direct and trap-assisted tunneling, the orange line represents the edge glow, the gray line shows the Rule-22 model adjusted for our cutoff wavelength and junction implant size, and finally a green line representing the sum of orange, red, and black components.

He wrote:

> *A man starts from a point O and walks ℓ yards in a straight line; he then turns through any angle whatever and walks another ℓ yards in a straight line. He repeats this process n times. I require the probability that after these n stretches he is at a distance between r and $r + \delta r$ from his starting point, O.*

The solution to this problem is:

$$P_n(r) = \frac{2}{n\ell^2} \exp\left\{-\frac{r^2}{n\ell^2}\right\} r dr \tag{3.4.3}$$

where r is measured in the same units as ℓ. This treatment isn't ideal for our situation as it assumes equal step sizes and fails to account for the aforementioned drift, but it serves as a good starting point.[31] Mosby uses this solution and tailors it to apply more appropriately to the physics of the pixel, accounting for the fact that the pixels drift in three dimensions, not two, and that the hole drift ends after n collisions due to the electric field. Mosby generalizes Rayleigh's solution by replacing ℓ with the mean free path of holes λ_h projected onto the x-y plane:

$$\ell = \frac{\pi}{2} \int_0^{\frac{\pi}{2}} \sin(\phi) d\phi \lambda_h = \frac{2}{\pi} \lambda_h \tag{3.4.4}$$

Substituting that into Equation 3.4.3 and solving to get the charge-spreading point spread function (PSF):

$$\Psi(r) = \frac{\pi}{4n{\lambda_h}^2} \exp\left(-\frac{\pi^2 r^2}{4n{\lambda_h}^2}\right) \tag{3.4.5}$$

which is a two-dimensional gaussian with a standard deviation of:

$$\sigma = \frac{\lambda_h}{\pi} \sqrt{2n} \tag{3.4.6}$$

The number of steps taken (n) can be calculated as a ratio of the time needed for a hole to drift out of the absorber (τ_d) to the mean scattering time (τ_s):

$$\tau_d = \frac{z}{\mu_h |E_d|} \tag{3.4.7}$$

$$\tau_s = \frac{\mu_h m_h^*}{q} \tag{3.4.8}$$

$$n = \frac{\tau_d}{\tau_s} \tag{3.4.9}$$

where $|E_d|$ is the drift field amplitude (which decreases with distance from the 'center' of the p-n junction), μ_h is a hole mobility parameter, m_h^* is the effective mass of holes, and q is the elementary charge. The mean thermal velocity of holes (v_{th}) multiplied by the mean scattering time yields the mean free path of holes in the detector:

$$v_{th} = \sqrt{\frac{kT}{m_h^*}} \tag{3.4.10}$$

$$\lambda_h = v_{th}\tau_s \tag{3.4.11}$$

which yields the charge-spreading PSF as a function of real detector parameters:

$$\sigma = \frac{1}{\pi}\sqrt{\frac{2kTz}{q|E_d|}} \tag{3.4.12}$$

where T is the temperature, and z is the vertical distance traveled, which is on the order of the thickness of the absorber layer.[31] Mosby's solution, presented above, presents an important inverse-root relation between E_d and σ. It is extremely relevant for detectors like V23, which operate at high reverse biases, and thus have high E_d. Modeling of threading dislocations in MCT also suggests that the space around threading dislocations has increased electric potential, which could theoretically contribute to this shrinking of σ, especially in a material as defective as that of V23.[40]

Pixels in Q4 of V23 exhibits a characteristic crosstalk that is very low in the 4-neighbors and near-zero in the 8-neighbors, as shown in Figure 3.23. The increased crosstalk in the pixel directly right of center is consistent with increased crosstalk in pixels that follow pixels with high signal in the read direction, often attributed to incomplete settling of the output amplifier. This form of crosstalk is separate from crosstalk due to charge diffusion.

Several techniques exist for measuring interpixel crosstalk. Passive approaches rely on rare,

randomly occurring events: cosmic-ray hits during long dark exposures or X-ray photons from a radioactive source such as ^{55}Fe.[31, 54] Although effective, these methods require substantial total integration time to accumulate sufficient statistics.

Active techniques deliberately create localized charge sources. One established method, developed by Teledyne for HxRG detectors, forward-biases selected pixels to generate controlled hot spots, exploiting the per-pixel reset capability of those ROICs.[55, 56] The VIRGO ROIC used in the SATIN detectors lacks individual pixel addressing, so this approach is not feasible. For the present work, crosstalk was therefore quantified using naturally occurring hot pixels within the array as charge-injection sites.

The crosstalk measurement technique developed for the SATIN detectors circumvents the limited statistics inherent in cosmic-ray-based methods. At the Center for Detectors the standard approach identifies cosmic-ray hits in long dark exposures; however, the extensive shielding of both the dewar and laboratory, combined with the detector orientation, severely suppresses the cosmic-ray flux. Moreover, surviving events typically deposit large, highly asymmetric charge clouds that complicate the isolation of conventional interpixel coupling, necessitating rejection of most candidates.[56, 57] Because the engineering-grade SATIN arrays contain abundant naturally occurring hot pixels, an alternative procedure was implemented that exploits these defects as controlled charge-injection sites. The algorithm proceeds as follows:

1. All persistently hot pixels are identified in a dark ramp dataset.
2. Any hot pixel within three pixels of another hot pixel is excluded, along with its neighbor, to eliminate mutual contamination.
3. Hot pixels within four pixels of the array edge are also excluded to avoid boundary artifacts.
4. An empty $3 \times 3 \times N$ array is constructed, where N is the number of identified hot pixels.
5. Each of the N 3×3 subarrays is populated with the values of the hot pixel and its neighbors, normalized to the signal in the hot pixel.

6. Two 3×3 arrays are created and populated with the mean and median values for each element through the master $3 \times 3 \times N$ array.

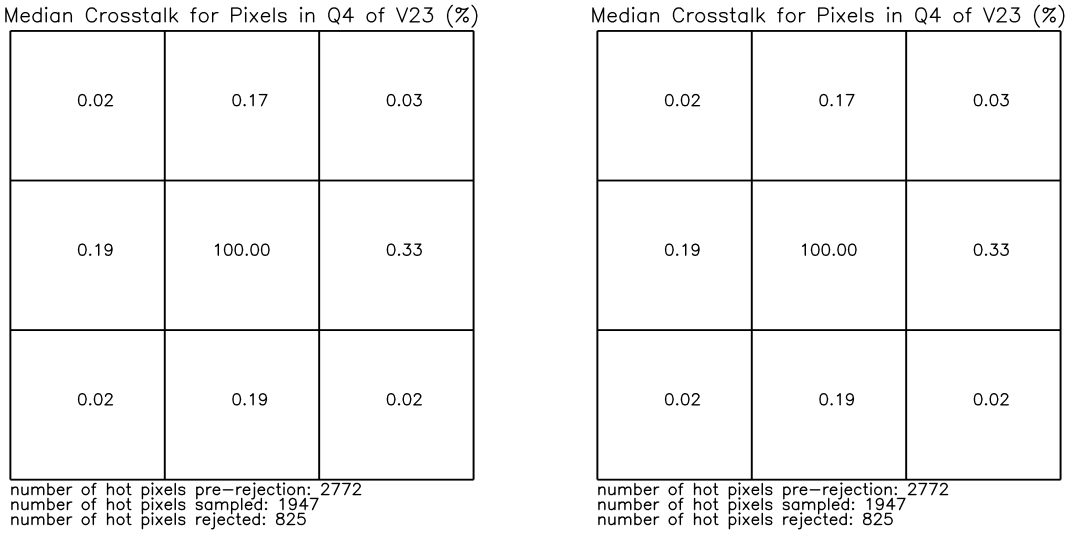

Figure 3.23: The figures above show median and mean values for crosstalk around hot pixels ("events"). The values are normalized to the central pixel, then medians and means are calculated.

Figure 3.23 shows interpixel crosstalk values for V23 that are approximately one order of magnitude lower than those measured in the WFIRST H4RG-10 detectors, where typical values are near 2%.[31] This substantial reduction arises primarily from two factors: minority-carrier lifetime and pixel pitch. V23 employs a $20\,\mu$m pitch (twice that of the H4RG-10) and is fabricated on significantly more defective HgCdTe material, which decreases carrier lifetime, diffusion length, and thereby suppresses lateral charge spreading. The two devices operate under comparable conditions in other respects: identical detector reverse bias magnitude (1 V), similar absorber thickness, and low-viscosity epoxy fill between indium bumps for mechanical support—a feature known to increase crosstalk relative to air-filled gaps because of the higher dielectric constant of epoxy.[58]

3.5 Quantum Efficiency

Quantum efficiency (QE) quantifies the fraction of incident photons that produce collected photoelectrons in a detector pixel. The symbol η is conventionally reserved for internal quantum yield—the average number of electron–hole pairs generated per absorbed photon. Over the visible and infrared spectral range relevant to most astronomical detectors, internal quantum yield is effectively unity ($\eta = 1$). Certain specialized devices, such as avalanche photodiodes (APDs) and electron-multiplying CCDs, incorporate gain stages that can produce internal quantum yields $\eta \geq 10$ and, in extreme cases, many thousands.

The absolute QE in V23 does not display an obvious trend with p-n junction size for λ=800-2300 nm, but a trend in the ratio of peak QE to longwave QE does appear. Figure 3.24 shows that Q1 and Q4 exhibit higher peak QE than Q2 and Q3, though they have vastly different p-n junction sizes. The peak QE for Q1 and Q4 appears to exceed 100% due to individual scan errors of 5-10%. We estimate the actual QE peak for Q4 to be $\approx$95%. A trend of increasing long-wave (LW) QE with decreasing junction size is apparent. Figure 3.24 shows only one dataset, though the results are representative of the many other experiments carried out on this device. Figure 3.25 shows the QE curves, normalized and overplotted to show the trend of better long-wave (2500-2650 nm) QE performance with decreasing junction size. The data are normalized by the mean of each curve's peak (2200-2400 nm) QE values. The bottom-left plot in Figure 3.25 shows mean peak QE (black diamond), the median peak QE (red cross), LW mean QE (blue circle), and LW median QE (green triangle) for each quadrant. The bottom-right plot shows the LW/peak mean ratio (black diamond) and the LW/peak median ratio (red cross) for each quadrant. No model was developed that can accurately explain why this LW QE droop happens, and it is possible that it is an effect of measurement error, due to improper linearity correction, or persistence. However, it should be noted that QE measurements carried out at low fluences - where the pixel response is most linear - display the same behavior as is shown in these figures.

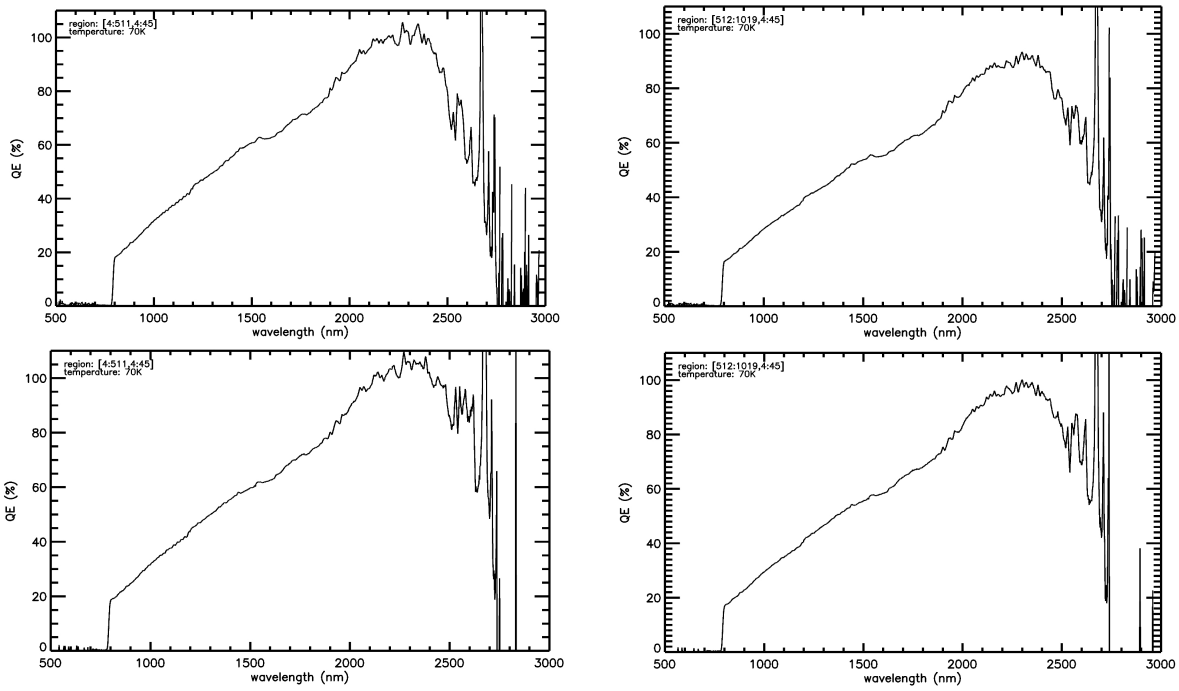

Figure 3.24: This figure shows the quantum efficiency measurement for V23 device quadrants. Starting in the top-left and going clockwise, the plots show QE for Q1, Q2, Q3, Q4.

3.6 Linearity

As described in Section 2.2.1, the reverse-biased p-n junction behaves as a parallel-plate capacitor whose capacitance increases with collected charge. From Equation (3.6.13) the reciprocal of this capacitance represents the voltage response per unit charge. Consequently, as charge accumulates in the pixel the incremental sensitivity to additional photoelectrons decreases. This well-documented effect is commonly known as pixel nonlinearity.[59, 29, 31, 54, 58]

$$C_{\text{dep}} = \left| \frac{\mathrm{d}Q}{\mathrm{d}(V_0 - V_r)} \right| \implies \left| \frac{\mathrm{d}(V_0 - V_r)}{\mathrm{d}Q} \right| = \frac{1}{C_{\text{junc}}} \tag{3.6.13}$$

Figure 3.26 shows the average fractional countrate for pixels in Q1 and Q4 of V23, which have p-n junction implants of 13μm and 4μm, respectively. The curves show how the response of the detector to individual units of charge decreases as the storage well of pixels fills. The Q1 pixels behave as expected, with a gradual and near-linear drop in response as charge is

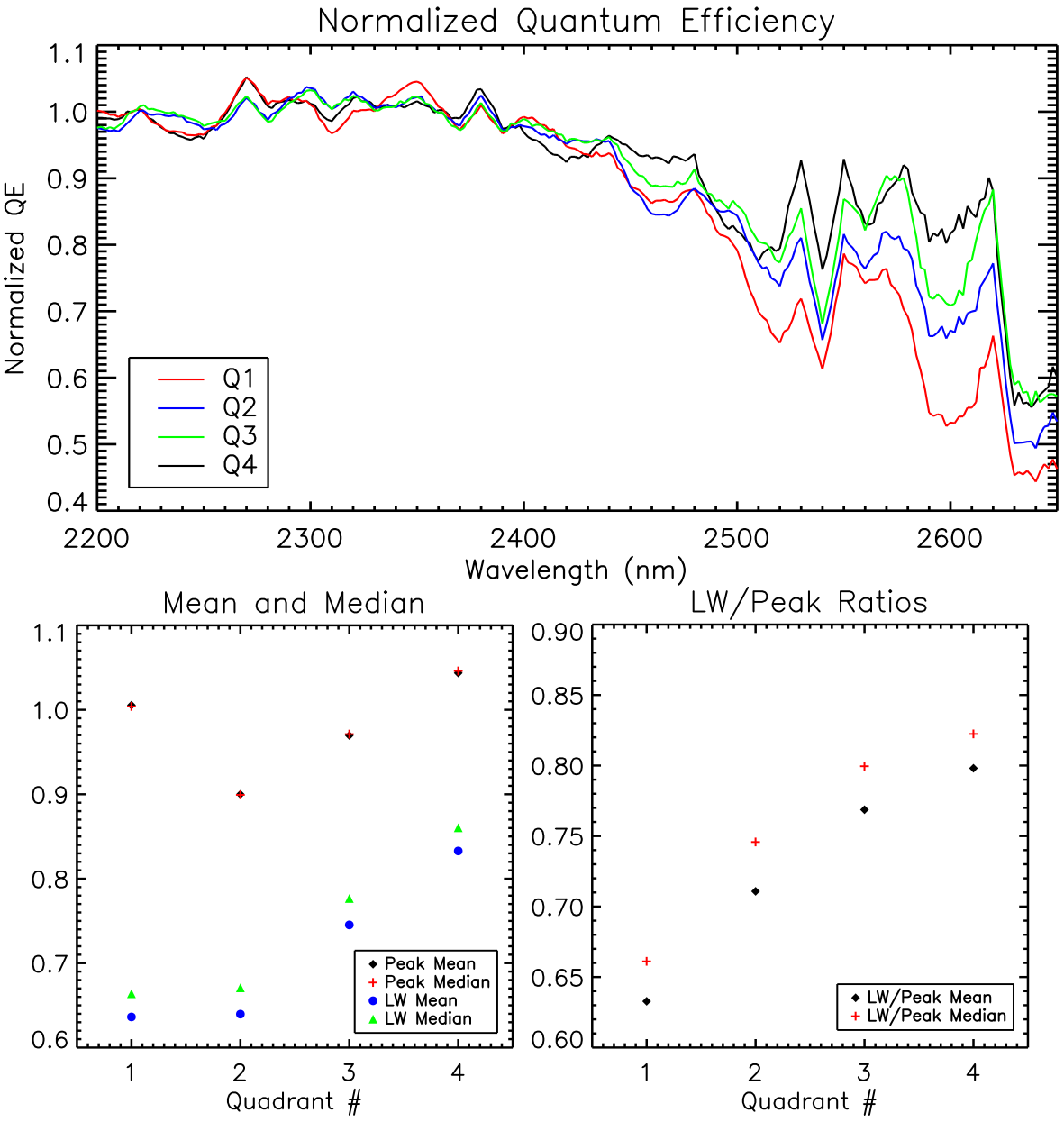

Figure 3.25: This figure shows a close-up of the long-wave QE response in each quadrant of the V23 device. The top plot shows a close-up of the QE for each quadrant, normalized to the mean of the peak (2200-2400 nm). The bottom-left plot shows the mean peak QE, the median peak QE, LW mean QE, and LW median QE for each quadrant. The bottom-right plot shows the LW/peak mean ratio and the LW/peak median ratio for each quadrant.

integrated. This trends as expected with the dominant source of capacitance in the pixel, which is the sum of C_s and C_b (defined in Section 2.2.1). The Q4 pixels exhibit a significant drop in signal response at about 50% of the full well depth, which seemingly approaches a plateau before the pixel saturates and detector response goes to zero.

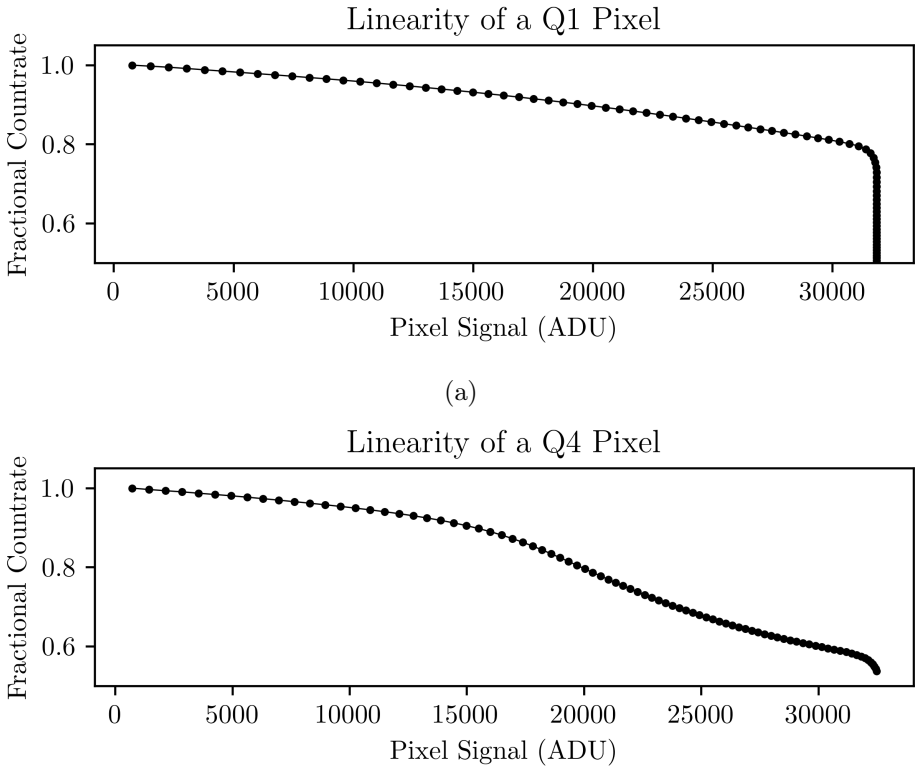

Figure 3.26: These plots show the fractional countrate of pixels in Q1 and Q4 as a function of increasing charge within the pixel.

Figure 3.27 presents calculated capacitance contributions for the p-n junctions in quadrants Q1 and Q4. The bottom-junction capacitance C_b scales with implanted area, whereas the sidewall capacitance C_s scales with junction perimeter. Consequently, C_s becomes dominant as the implanted junction area is reduced. This trend agrees with published results and confirms that the parameter values adopted here—necessarily estimated in the absence of proprietary device specifications—yield physically reasonable behavior. The gate capacitance C_g, assumed independent of junction area, is also plotted; it becomes the largest term at the

smallest implant sizes.

By combining C_b, C_s, C_g, and a small fixed parasitic capacitance, the expected nonlinearity of pixel response can be simulated. One such calculation is shown in Figure 3.28 and successfully reproduces the overall shape of the measured linearity curve presented in Figure 3.26. As noted in Section 2.2.1, accurate modeling of pixel nonlinearity requires detailed knowledge of the ROIC layout, which is not available. The simplified model presented here therefore represents the most practical approximation achievable with the information at hand.

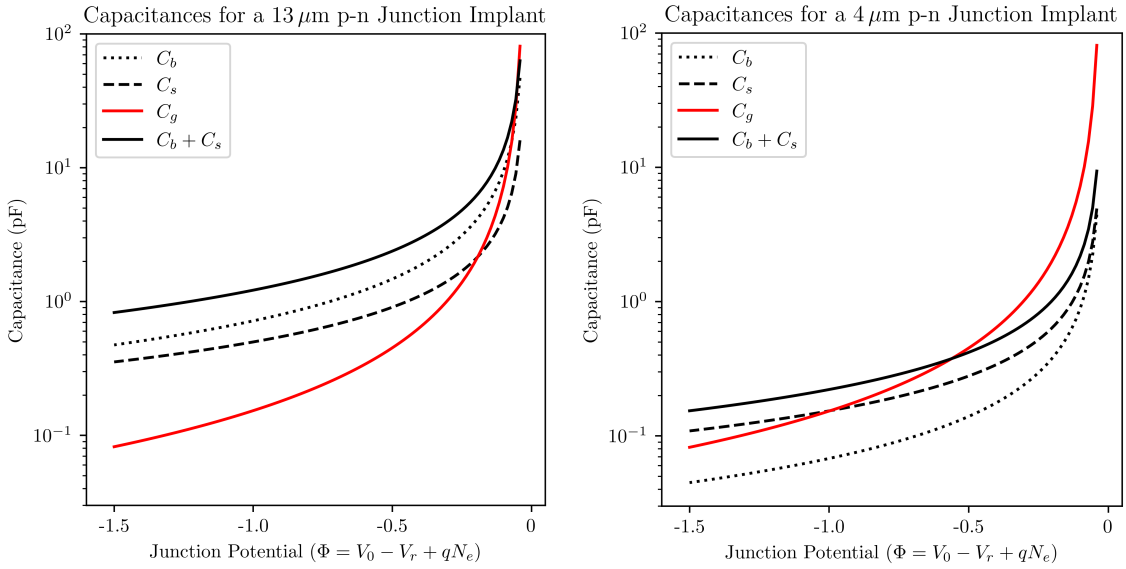

Figure 3.27: The left panel of this figure shows the bottom-junction capacitance C_b, sidewall capacitance C_s, and gate capacitance C_g calculated as functions of collected charge for pixels with the 13 μm junction implant. The right panel shows the same three capacitance components for pixels with the 4 μm junction implant.

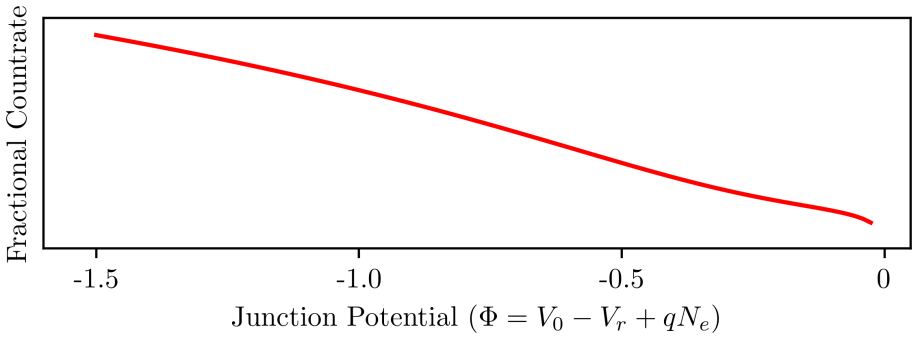

Figure 3.28: This figure shows the simulated expected nonlinearity for Q4.

Chapter 4

On-Sky Verification

This chapter is based on previously published work:

1. Buntic, Lazar, et al. 2024, *Advancing Large Format MCT/Si Infrared Detectors for Astrophysics Research*, SPIE Proceedings Volume 13103, DOI: 10.1117/12.3019111

The detector system was deployed at the University of Rochester's C.E.K. Mees Observatory (42° 42′ 1″ N, 77° 24′ 31.56″ W) from December 7, 2023, to January 18, 2024. Observations of various planets, galaxies, stars, and star clusters were planned, though not all were performed. Unfortunately, as expected in northern New York, the winter weather was uncooperative, rendering most of the scheduled nights at the observatory useless due to cloud cover and snow. However, a few clear nights (spanning December 13 to December 16, 2023) were utilized to generate the results presented here.

4.1 Observing Equipment

The system, as deployed, is shown in Figure 4.1. The orange dewar houses the detector, which is cooled by an Edwards Ltd. (Burgess Hill, U.K.) model 9600 helium compressor. A Lake Shore Cryotronics Inc. (Westerville, OH, U.S.A.) temperature controller monitors temperatures and maintains heater power throughout the observing period. JMClarke Engineering (Simi Valley, CA, U.S.A.) provided the set of detector electronics used to run the detector. This system and equipment are very similar to other experiments deployed by the Center for

Detectors.[60, 61] Custom fixtures were designed and fabricated by the CfD team to interface the dewar system with the telescope and mount the detector electronics. A Parker Hannifin Corp. (Mayfield Heights, OH, U.S.A) OEM750 Step Motor Indexer/Drive operates the filter wheel inside the dewar, which contains a set of J, H, and K-band filters from Materion Corp. (Westford, MA, U.S.A.). Table 4.1 lists the properties of the filters.

Table 4.1: This table lists the properties of the filters used for the observing program. The cut-on and cutoff wavelengths represent half-power points, and the transmission is the average of all transmission values above 70% for each filter. Note that the K-band filter used for this program is distinct from the 2MASS K_s filter.

Filter Name	**Cut-On λ (nm)**	**Cutoff λ (nm)**	**Transmission (%)**
J	1111	1383	80
H	1507	1798	90
K	2005	2400	91

The C.E.K. Mees Observatory telescope is a 60-centimeter f/13.5 Cassegrain telescope located in Ontario County, New York State. Constructed in 1965, the telescope has been modernized and is operated by a fully computerized control system built by the University of Rochester. The telescope is situated at the top of Gannett Hill, an hour south of the city of Rochester. As with many other observatories, the expansion of nearby cities over the past few decades has significantly increased light pollution in the locale. However, our NIR observations remain unaffected by city lighting because the sodium lamps typically used for street lighting cause optical line emission, which is filtered out by our near-infrared observing filters.[62] More significant challenges include tracking and focus instabilities due to the telescope's age - a few instances of gear slippage and drift in the focus position ruined some longer exposures.

4.2 Observation Targets

Several targets were selected for the observing program based on their accessibility during the observing period, breadth of brightnesses, and suitability for testing the detector's range of capabilities. The targets provide a rich variety of objects for both photometry and detector characterization. This thesis presents the photometric results for the M42, M29, and M37

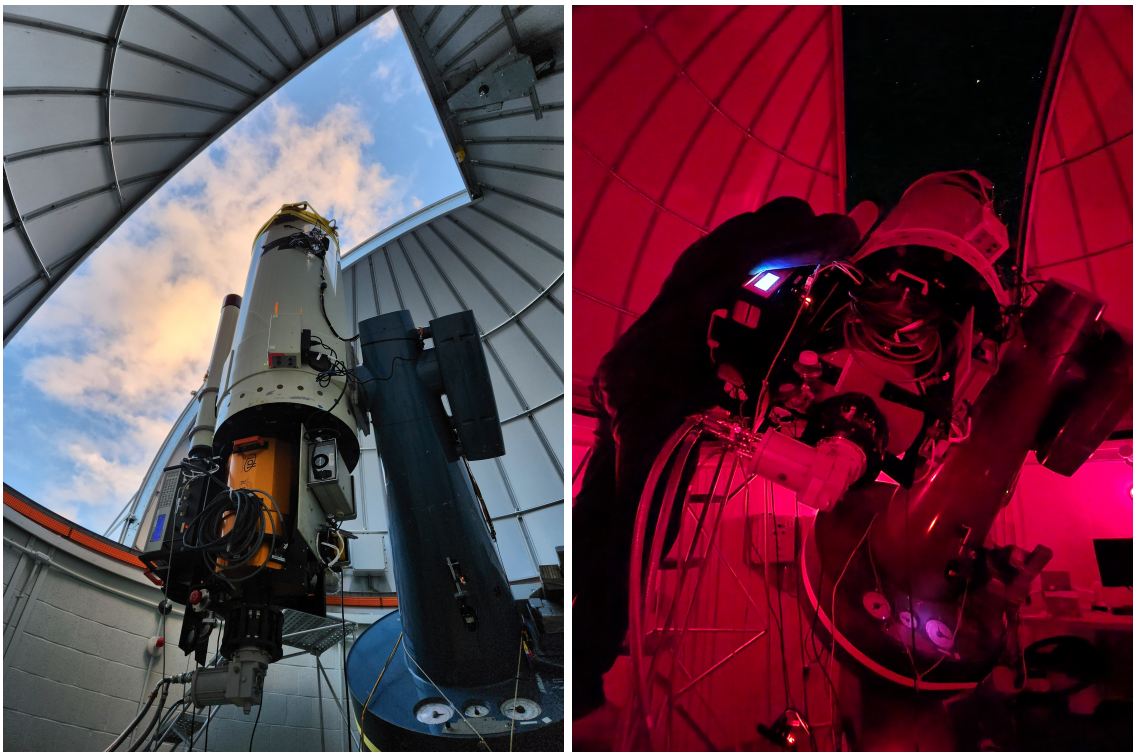

Figure 4.1: This figure shows the detector system as deployed at the Mees Observatory. In the left panel, the orange dewar contains the SATIN V23 detector chip. To the left of the dewar are the electronics used to monitor and maintain the system temperature, and to the right are the detector electronics.

clusters.

4.3 Data Reduction for Observations

Observation data is captured from the detector and output into the astronomy-standard `.fits` format using custom IDL routines. Numerous tools are available for manipulating `.fits` files in essentially every major computing language, often rooted in code written with the IRAF command language in 1981.[63] All results shown below were generated using custom code written in IDL.

Multiple datasets were taken for each object in each of the observing bands (J, H, K), and the telescope was dithered for each dataset. Dithering, a well-established practice in observational astronomy, involves shifting the field-of-view by a few arcseconds between exposures. This technique ensures robustness against cosmic ray hits and bad pixels during reduction by varying the landing position of the star's point-spread function (PSF) across different pixels. By doing so, one can effectively reject information that lands on bad pixels without compromising data completeness, which is maintained by co-adding exposures.[64] This also controls for pixel-to-pixel variation in QE, which is always present in CMOS devices.

We collect science data 'up-the-ramp' by taking a series of non-destructive reads over a set exposure time while the telescope tracks the target.[65] We take calibration frames to accompany each target, including dark current frames ('darks'), sky images, and flat field images ('flats'). Darks are taken when the detector is closed off from the optical path to measure the contribution from thermally generated electron noise in the detector (See Section 3.3). Since darks are independent of the optical path, we usually take them at the start or the end of the observing night, or during the day. It should be noted that taking darks at significantly different times from the data can be problematic for imaging systems that don't have precise temperature controls, since dark current is a thermal effect. Our dewar system maintains a stable 70K detector temperature at all times. We primarily take dark data during the day to maximize the observing time each night. We collect sky images during data acquisition as one of the dither positions. We take them by dithering the telescope FOV

to an area clear of stars to measure the glow and thermal emission of the atmosphere, which we subtract from the data. We take flat frames by illuminating the detector with uniform light and later use them to correct for aberrations in the optical path, such as vignetting.[66, 64] The flats used for the observing program were obtained by imaging the evening sky around sunset, which provided a well-illuminated and gradient-free flat field.

The IDL reduction code first subtracts frame zero from frame n of each ramp in the data, darks, sky images, and flats to remove any residuals from the initial biasing of the detector at the start of the ramp. Second, the code subtracts the darks from the data, flats, and sky images. Third, the code normalizes the flats by their median value and subtracts the sky image from the data. Fourth, the code converts the data from digital numbers (DN) to electrons and divides it by the normalized flat, yielding the final science image which we use to perform photometry. Fifth, the code feeds the science image to a star-finding algorithm that locates the stars in the image and measures them. Finally, the code passes the locations and fluxes of the stars to the master analysis code, which matches the data from all three photometric bands to data from a query of the Vizier 2MASS database, and we plot the results.[67] The following subsections show results for observations of M42, M29, and M37.

4.4 M42 Results

M42 (NGC 1976), the Orion Nebula, is one of the brightest nebulae in the northern sky. It is one of the closest star-forming regions to Earth, and has been extensively studied since its discovery in the early 17^{th} century. In 1617, Galileo observed and documented the Trapezium cluster, a bright star association that provides most of the nebula's illumination. M42 also contains the Becklin-Neugebauer (BN) object, a heavily obscured proto-star adjacent to Trapezium.[68, 69, 70] We chose M42 primarily for the BN object, which is brightest in the K-band for our detector. The stellar density, gas structure, and BN object provide rich data for our analysis and allow extensive testing of the detector in all three observing bands.

We collected M42 data in a series of 40-second exposure ramps between 22:18 ET, December 14, 2023, and 02:30 ET, December 15, 2023. We took four sets of three ramps with the

Trapezium cluster centered in a single quadrant for each observing band. We repeated this for each of the four quadrants, resulting in 48 sets of three ramps.

Figure 4.2 shows a color-composite image of M42 with its corresponding field plot. North is up, and East is left. The image depicts the gaseous structure around the Trapezium cluster and the BN object heating its natal cloud. The photometry for M42 is the least accurate of the three objects presented in this thesis. We attribute this to several factors: (1) the images are composites generated by co-adding all observation data, meaning that data from separate quadrants were co-added - potentially introducing errors not removed during data reduction; (2) the primitive photometry routines (a DAOPHOT derivative for IDL 6.3, implemented without PSF-fitting) are not well-suited to crowded field photometry; and (3) the observing data was contaminated by wispy cloud cover, reducing the measured fluxes from stars by unquantifiable and random amounts. PSF fitting may improve the results, but issue (3) likely still dominates the uncertainties. The photometric measurements of stars in our data largely deviate from the Vizier 2MASS data, with mean deviations of 0.798, 0.949, and 0.763 magnitudes in the J, H, and K bands, respectively.

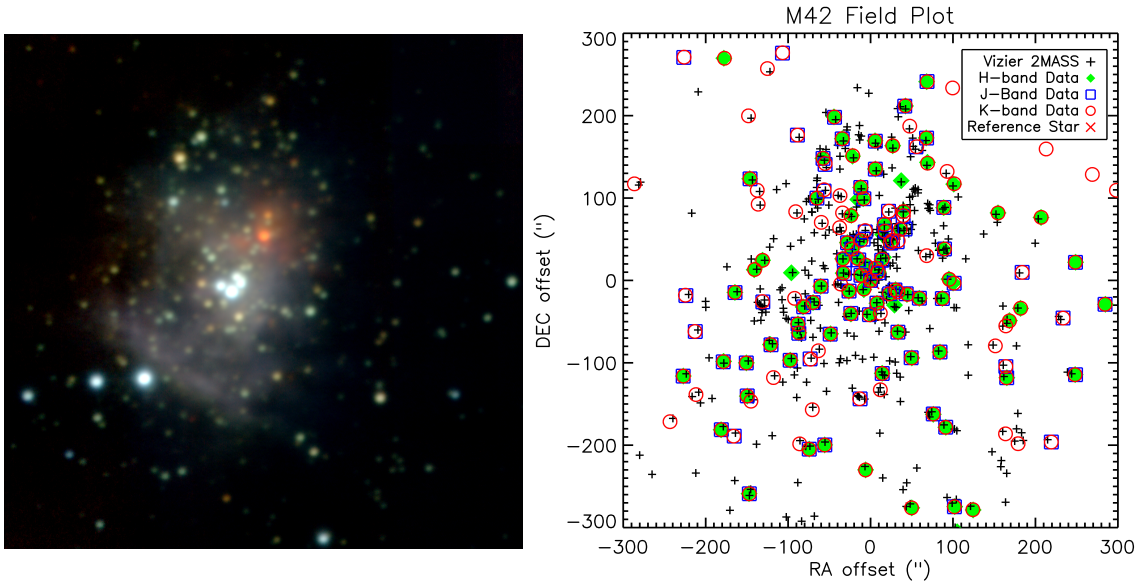

Figure 4.2: The figure on the left presents a color-composite image of M42, stretched to highlight the gas structure. The plot on the right is the field plot, showing the stars identified in each band by our analysis.

4.5 M29 Results

In the IR regime, M29 (NGC 6913) is a young and uncrowded open cluster, selected as an object of interest due to the presence of approximately a dozen sparsely positioned bright stars with magnitudes in the range of JHK $\approx$ 6-11. Table 4.2 lists the stars identified in our photometry, along with the magnitudes reported for them in the Vizier 2MASS catalog. Photometry results were normalized to the brightest star in the frame, meaning that we chose a zero-point magnitude to align our photometric measurement with the catalog results. This decision was primarily made because the exposures were short and had low enough fluence to remain in the linear regime of the detector. Star #0 in Table 4.2 is the brightest object in our frame and serves as the reference star.

The data for M29 were collected in a series of 40-second exposure ramps, between 20:07 and 21:45 ET, December 14, 2023. For each observing band, we took four sets of three ramps, resulting in 12 sets of three ramps each.

Figure 4.3 presents a color-composite image of M29, adjacent to its corresponding field plot. Note the high color variation between stars. Figure 4.4 displays the J-H and J-K color-magnitude diagrams (CMD), which agree remarkably well with the Vizier 2MASS catalog data. Figure 4.5 shows one more CMD, as well as a color-color diagram, comparison to the works of Straižys et al., 2014, 2015.[71, 72] In Figure 4.4, the stellar main sequence and turn-off stretches top-to-bottom on the left side of the plots, while the non-cluster members have higher color values. Figure 4.6 illustrates the deviations of our photometric results, which are generally within 0.2 magnitudes of the catalog data. The y-axis is the stellar magnitude as listed in the 2MASS database, and the x-axis is the difference between that value and that of our photometry. This is significantly better than the M42 data, for a number of reasons: (1), the stellar field is sparse, allowing ample space for the basic photometry routines to generate accurate measurements of the stars with stellar and inner-outer- sky annuli, without interference from other stars; (2), the stars aren't overwhelmingly bright, and thus the detector response to the light is well within the linear regime of our pixel; (3), as all the exposures kept stars in the same quadrants between exposures, the aforementioned quadrant co-adding effect

may not be present; and (4), the data was uncontaminated by cloud cover, resulting in accurate flux measurements. The photometric measurements of stars in our data agree with the Vizier 2MASS data, with mean deviations of 0.046, 0.052, and 0.110 magnitudes in the J, H, and K bands, respectively.

Given the high quality of the M29 photometry, we are able to calculate QE from the data and compare against the in-lab QE experiment. With reasonable assumptions about the transmission of the atmosphere and the reflectivity of the telescope mirrors, we estimate the QE of the detector using Star #0 in Table 4.2 and the following equation,

$$\mathrm{QE_H} = \frac{F_{\mathrm{phot}}}{F_{\mathrm{expected}}} = \frac{\frac{S_{\mathrm{phot}}}{t_{\mathrm{int}}}}{(F_{0,\mathrm{H}} \times 10^{-0.4 m_{\mathrm{H}}})\,(R_{\mathrm{mirr}})^n\,\Delta\lambda_{\mathrm{FWHM}}\,T_{\mathrm{filt}}\,T_{\mathrm{atm}}\,\Delta A} \tag{4.5.1}$$

where $S_{\mathrm{phot}} = 1.26 \times 10^7\,\mathrm{e^-}$ is the total signal from aperture photometry, $t_{\mathrm{int}} = 40\,\mathrm{s}$ is the integration time of the exposure, $F_{0,\mathrm{H}} = 1.138 \times 10^{-9}\,\mathrm{erg/cm^2/s/nm}$ is the Vega zero-point flux for the H-band, $m_{\mathrm{H}} = 6.499$ is the 2MASS H-band magnitude, $\Delta\lambda_{\mathrm{FWHM}} = 291\,\mathrm{nm}$ is the bandpass of the filter, $T_{\mathrm{filt}} = 0.9$ is the average filter transmission, $T_{\mathrm{atm}} = 0.6$ is the transmission of the atmosphere, $R_{\mathrm{mirr}} = 0.8$ is the reflectivity of the mirror, $n = 2$ is the number of mirrors in the telescope, and $\Delta A = 2,572\,\mathrm{cm^2}$ is the primary mirror area minus the secondary mirror obstruction. When these values are plugged into Equation 4.5.1, we get that $\mathrm{QE_H} = 0.60$, which is exactly the expected QE of 60%. Granted, our value for R_{mirr} is just a best guess, provided by telescope staff, as the mirrors have not been cleaned or resurfaced in many years. Additionally, T_{atm} likely varies throughout the total observation time as we track the object across the sky and the amount of atmosphere the starlight passes through changes.

Table 4.2: The table below lists stars identified in our M29 data, the photometric measurements from the Vizier 2MASS catalog, and our photometry results.

M29		Vizier 2MASS Catalog					Photometry				
#	2MASS Identifier	m_J	m_H	m_K	J-H	J-K	m_J	m_H	m_K	J-H	J-K
0	20235311+3828220	7.603	6.499	6.124	1.104	1.479	7.604	6.499	6.124	1.105	1.480
1	20234596+3830033	7.133	6.734	6.323	0.399	0.810	7.055	6.690	6.282	0.365	0.773
2	20240466+3832172	7.015	6.822	6.717	0.193	0.298	7.061	6.821	6.557	0.240	0.504
3	20240654+3829332	7.247	7.093	6.989	0.154	0.258	7.280	7.070	6.913	0.210	0.367
4	20240130+3830496	7.344	7.178	7.100	0.166	0.244	7.361	7.151	6.897	0.210	0.464
5	20235100+3829343	7.738	7.572	7.528	0.166	0.210	7.730	7.524	7.401	0.206	0.329
6	20235501+3827588	7.749	7.584	7.498	0.165	0.251	7.730	7.530	7.516	0.200	0.214
7	20234432+3830430	9.803	7.704	6.773	2.099	3.030	9.712	7.641	6.719	2.071	2.993
8	20235906+3829406	10.030	7.981	7.120	2.049	2.910	9.800	7.918	6.991	1.882	2.809
9	20234116+3827000	9.163	8.311	7.979	0.852	1.184	9.250	8.440	8.193	0.810	1.057
10	20235954+3831479	8.637	8.488	8.441	0.149	0.196	8.680	8.475	8.221	0.205	0.459
11	20234594+3831476	10.569	9.122	8.563	1.447	2.006	10.342	8.980	8.305	1.362	2.037
12	20240896+3830306	10.713	9.147	8.538	1.566	2.175	10.809	9.150	8.690	1.659	2.119
13	20240022+3832445	10.702	9.209	8.597	1.493	2.105	10.741	9.163	8.305	1.578	2.436
14	20235507+3829080	9.642	9.441	9.363	0.201	0.279	9.612	9.416	10.940	0.196	-1.328

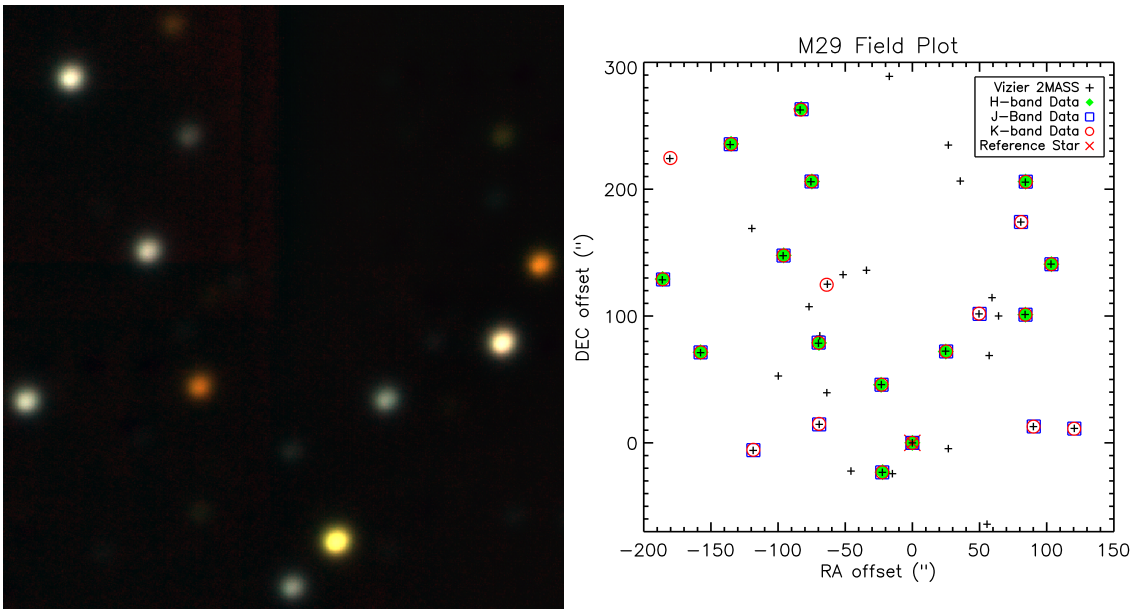

Figure 4.3: The figure on the left shows a color-composite image of the M29 cluster, after processing and stacking. The figure on the right shows a field plot of the M29 cluster. The red cross at (0,0) denotes the bright yellow star in the image, used to align the query with our data.

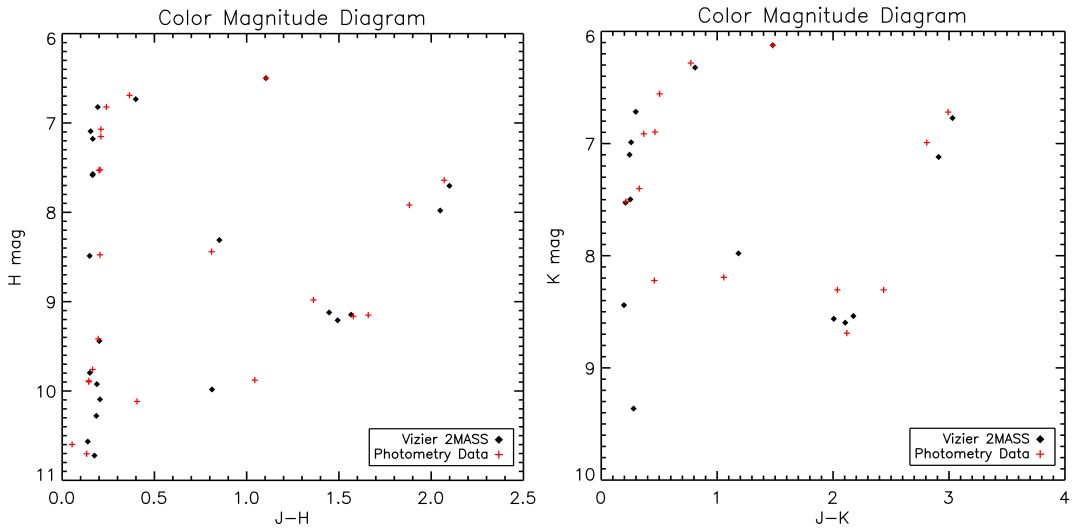

Figure 4.4: This figure shows two color-magnitude diagrams for M29. Note the clustering of the main sequence on the left side of each plot, from top to bottom, and note the turn-off near the top.

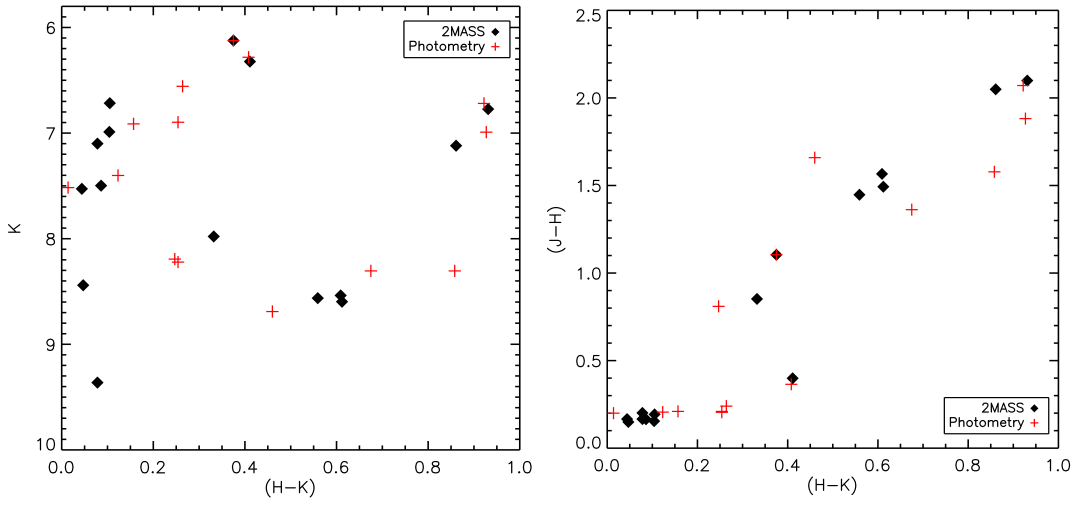

Figure 4.5: This figure shows another color-magnitude and color-color diagram for M29.

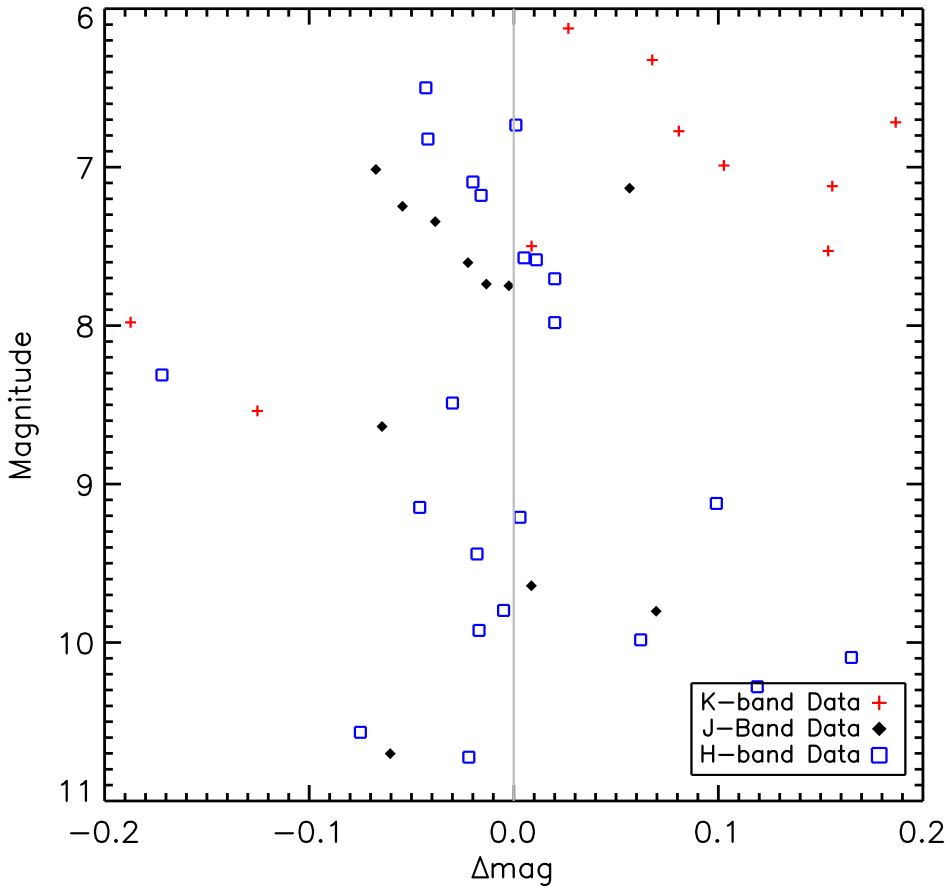

Figure 4.6: This figure shows a Δmagnitude plot of the stars identified in our M29 data. The y-axis represents 2MASS magnitude, while the x-axis is the difference between that value and our photometric measurements.

4.6 M37 Results

In the IR regime, M37 (NGC 2099) is a rather crowded open cluster, selected as an object of interest due to the presence of many stars with magnitudes in the range of JHK mag ≈ 6-12. The results were normalized to a star of medium brightness, meaning that a zero-point magnitude was chosen to match our photometric measurement with the catalog results. We choose this star (first star to the top-right of the brightest one in Figure 4.3) because it has sufficiently low fluence to remain in the linear regime of the detector, even over the full duration of the exposure.

The data for M37 were collected in a series of 160-second exposure ramps, between 22:13 ET, December 15, 2023, and 01:32 ET, December 16, 2023. As with M29, we took four sets of three ramps in each band, resulting in 12 sets of three ramps.

Figure 4.7 presents a color-composite image of M37, adjacent to its corresponding field plot. Figure 4.8 shows the J-H and J-K color-magnitude diagrams (CMD), which show close agreement to the Vizier 2MASS catalog data. Figure 4.9 illustrates the deviations of our photometric results, which are generally within 0.5 magnitudes of the catalog data. The photometric measurements of stars in our data agree with the 2MASS data, with mean deviations of 0.233, 0.269, and 0.383 magnitudes in the J, H, and K bands, respectively. As with M42, the accuracy of the photometry in this cluster was worse than with M29, for the same reasons (high stellar density, primarily).

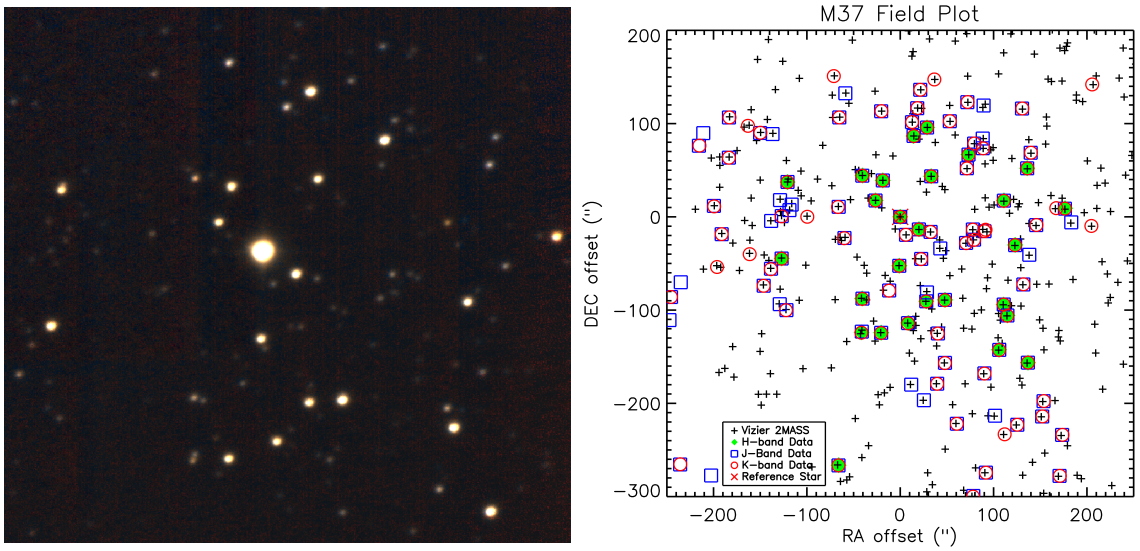

Figure 4.7: The figure on the left shows an H-band image of the M37 cluster, after processing and stacking. The figure on the right shows a field plot of the M37 cluster. The red cross at (0,0) denotes the brightest star in the image, used to align the query with our data.

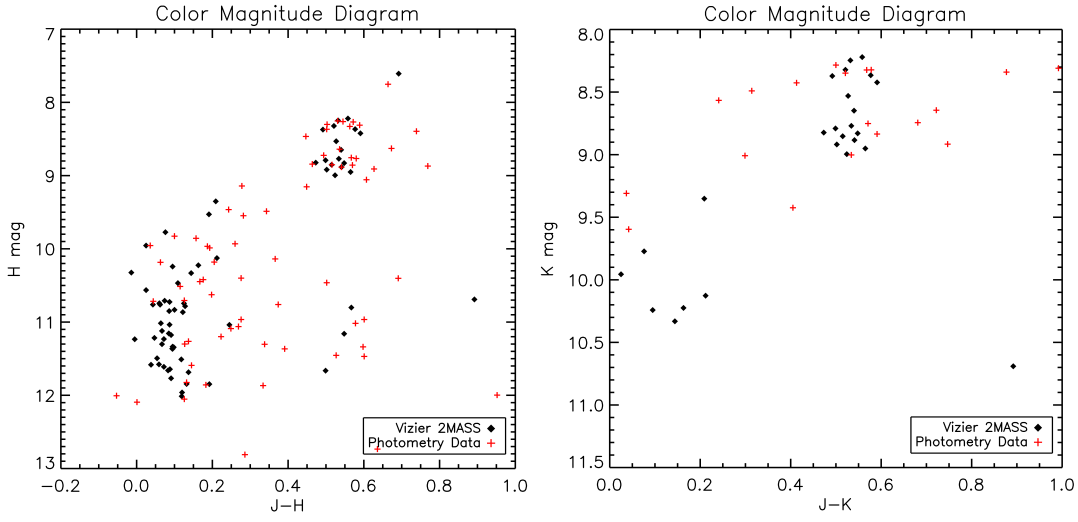

Figure 4.8: This figure shows two color magnitude diagrams for M37.

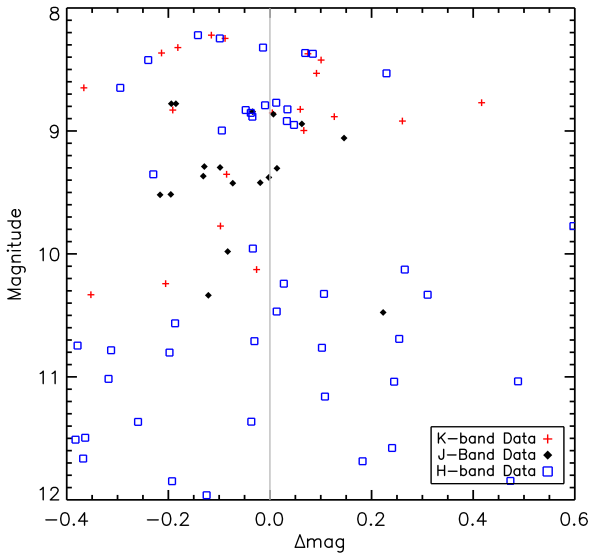

Figure 4.9: This figure shows a Δmagnitude plot of the stars identified in our M37 data.

Chapter 5

Summary and Conclusions

In this thesis, progress in the characterization of Raytheon's HgCdTe-on-Si detectors was discussed. Chapter 1 provided a brief history of scientific imaging and an overview of the HgCdTe material and VIRGO ROIC structure. Chapter 2 introduced the operating principles of the photodiode p-n junction and its features, including dark current and persistence mechanisms. Chapter 3 presented the results of my efforts to characterize dark current and persistence effects in the SATIN detectors, including brief discussions of crosstalk and pixel linearity. Chapter 4 presents the results of an observing run carried out with V23.

The dark current for the best pixels in the detector are shown to be more than an order of magnitude lower than the quadrant median published in previous works. The measured dark current is limited by multiplexer glow near the bottom of the array, and by trap-assisted-tunneling elsewhere. By analyzing the contributions from multiplexer glow and dark current mechanisms, the intrinsic dark current floor has been isolated and modeled as a function of temperature and sampling frequency. Persistence measurements have revealed a broad spectrum of charge-trapping timescales, spanning many orders of magnitude, with trapping occurring predominantly in the bulk active region rather than at surface states. A correlation has been established between p-n junction implant area and both elevated dark current and defective-pixel fraction, attributable to increased defect density within the active volume. These findings provide valuable insights into the limitations and potential improvements for

MCT-on-Si technology.

The dark current analysis has shown that the median dark current in the selected pixel population is approximately 0.0040 electrons per second at cryogenic temperatures, approximately twice that of the detectors used for the WFIRST array. Multiplexer glow from the column/output circuitry contributes at least 10% to this value, with the remainder dominated by glow from in-pixel source-follower transistors and trap-assisted tunneling facilitated by the elevated defect density in the MCT-on-Si material. Arrhenius modeling confirms that generation-recombination current becomes negligible below 100 K, while tunneling persists as the primary temperature-independent component. The edge-glow gradient, modeled as an exponential decay with distance from the ROIC bottom edge, accounts for an additional spatially varying background that must be subtracted to reveal the true pixel dark current distribution. These results indicate that defect reduction in the HgCdTe absorber—potentially through optimized buffer-layer growth—could further lower the dark current floor, bringing MCT-on-Si detectors into closer alignment with CZT-based devices.

Persistence characterization has quantified the trap charge-release timescales in the SATIN detectors. The excess charge observed in light illuminated versus bias manipulated measurements demonstrates that optical illumination likely accesses traps outside the nominal depletion region, such as near the backside surface, that bias manipulation alone cannot populate. Cross-sections through persistence images at fixed times after reset confirm linear growth of trapped charge with fluence, implying trap occupancy scales directly with integrated illumination. These persistence results underscore the role of bulk defects as the dominant trapping sites and suggest that substrate quality is a key limiting factor.

Interpixel crosstalk is approximately 0.2%, an order of magnitude lower than reported for the WFIRST 10 μm-pitch H4RG-10 detectors, attributable, in part, to the larger 20 μm pitch and reduced carrier lifetimes in the defective MCT-on-Si material. Unfortunately, this low crosstalk is likely to rise as improvements to the MCT-on-Si process are made, since purer materials will increase carrier lifetimes and better processes will lower pixel size.

The on-sky observations obtained with the SATIN detectors validate the laboratory char-

acterization. Despite the elevated dark current and persistence relative to CZT devices, the arrays produce usable astronomical images with acceptable noise performance after appropriate image processing, despite sub-par telescope equipment and observing conditions.

The results presented in this thesis indicate that MCT-on-Si detectors have the potential to become competitive with current state-of-the-art detectors, provided that the epitaxial growth process is improved and the arrays are hybridized to a more advanced readout integrated circuit (ROIC). If the defect density can be reduced to $\leq 10^5\,\mathrm{cm}^{-2}$, a critical barrier to lowering dark current and achieving high operability will have been overcome. Although the use of small-pixel junction implants has proven effective in improving operability, further substantial development of the ROIC architecture will likely be required to ensure that pixel linearity is not degraded by parasitic capacitance effects.

Bibliography

[1] Martin B. Sweatman and Alistair Coombs. Decoding european palaeolithic art: Extremely ancient knowledge of precession of equinoxes. *Athens Journal of History*, 5(1):1–30, 2019. 1

[2] Scott M. Johnson, William A. Radford, Aimee A. Buell, Mauro F. Vilela, Jeffrey M. Peterson, Jeffrey J. Franklin, Richard E. Bornfreund, Alexander C. Childs, Gregory M. Venzor, Michael D. Newton, Edward P. G. Smith, Lee M. Ruzicka, Gregory K. Pierce, Daniel D. Lofgreen, Terence J. de Lyon, and John E. Jensen. Status of HgCdTe/Si technology for large format infrared focal plane arrays. In Manijeh Razeghi and Gail J. Brown, editors, *Quantum Sensing and Nanophotonic Devices II*, volume 5732, pages 250–258. International Society for Optics and Photonics, SPIE, 2005. 1.3

[3] M. Vaghayenegar, R. N. Jacobs, J. D. Benson, A. J. Stoltz, L. A. Almeida, and David J. Smith. Correlation of etch pits and dislocations in as-grown and thermal cycle-annealed hgcdte(211) films. *Journal of Electronic Materials*, 46(8):5007–5019, Apr 2017. 1.3

[4] Richard E. Bornfreund, Peter J. Love, Alan W. Hoffman, Ken J. Ando, Elizabeth Corrales, William D. Ritchie, Neil J. Therrien, Joe P. Rosbeck, Aimee Buell, Jeffrey Peterson, Jeffrey Franklin, Mauro Vilela, J. Bangs, Scott M. Johnson, and William Radford. Large format short-wave hgcdte detectors and focal plane arrays. 2015. 1.3, 3.3.4

[5] Brandon J. Hanold, Donald F. Figer, Joong Lee, Kimberly Kolb, Iain Marcuson, Elizabeth Corrales, Jonathan Getty, and Lynn Mears. Large format MBE HgCdTe on silicon detector development for astronomy. In Paul D. LeVan, Ashok K. Sood, Priyalal Wijewar-

nasuriya, and Arvind I. D'Souza, editors, *Infrared Sensors, Devices, and Applications V*, volume 9609, page 96090Y. International Society for Optics and Photonics, SPIE, 2015. 1.3

[6] G. L. Hansen, J. L. Schmit, and T. N. Casselman. Energy gap versus alloy composition and temperature in Hg/1-x/Cd/x/Te. *Journal of Applied Physics*, 53:7099–7101, October 1982. 1.4.1, 2.2, 2.3.2

[7] Thibault Pichon and Luc Boucher. Pixel source follower glow in HxRG detector. *Astronomische Nachrichten*, 344:e20230102, October 2023. 1.4.2, 2.3.5, 3.3.3, 3.3.4, 3.3.7

[8] Ben G. Streetman and Sanjay Banerjee. *Solid state electronic devices*. Pearson/Prentice Hall, Upper Saddle River, N.J, 6th edition, 2006. 2.2, 2.2, 2.3.1

[9] M.B. Reine, A.K. Sood, and T.J. Tredwell. Chapter 6 photovoltaic infrared detectors. In R.K. Willardson and Albert C. Beer, editors, *Mercury Cadmium Telluride*, volume 18 of *Semiconductors and Semimetals*, pages 201–311. Elsevier, 1981. 2.2

[10] M.A. Kinch. *State-of-the-Art Infrared Detector Technology*. SPIE, 2014. 2.2, 2.3.2, 2.3.3

[11] S.M. Sze. *p-n Junctions*, pages 77–133. John Wiley & Sons, Ltd, 2006. 2.2, 2.3.3

[12] Chenming Hu. *Modern semiconductor devices for integrated circuits*. Prentice Hall, Upper Saddle River, N.J, 2010. 2.2, 2.3.1

[13] A. Rogalski. HgCdTe infrared detector material: history, status and outlook. *Reports on Progress in Physics*, 68(10):2267–2336, October 2005. 2.2

[14] M. Kopytko and A. Rogalski. New insights into the ultimate performance of hgcdte photodiodes. *Sensors and Actuators A: Physical*, 339:113511, 2022. 2.2

[15] Ralf Dornhaus, Günter Nimtz, and B. Schlicht. Narrow-gap semiconductors. 1983. 2.2

[16] Fei Wang and Albert Theuwissen. Linearity analysis of a cmos image sensor. *Electronic Imaging*, 29(11):84–84, 2017. 2.2.1

[17] Konstantin D Stefanov. *CMOS Image Sensors*. 2053-2563. IOP Publishing, 2022. 2.2.2

[18] Rory Bowens, Michael R. Meyer, Taylor L. Tobin, Eric Viges, Dennis Hart, John Monnier, Jarron Leisenring, Derek Ives, and Roy van Boekel. Characterization of a longwave HgCdTe GeoSnap detector. In Andrew D. Holland and Kyriaki Minoglou, editors, *X-Ray, Optical, and Infrared Detectors for Astronomy XI*, volume 13103, page 1310325. International Society for Optics and Photonics, SPIE, 2024. 2.3

[19] Candice Marie Bacon. *Development of long wave infrared detectors for space astronomy*. PhD thesis, University of Rochester, New York, January 2006. 2.3.1, 2.3.2, 2.3.4

[20] James Janesick, James Andrews, John Tower, Mark Grygon, Tom Elliott, John Cheng, Michael Lesser, and Jeff Pinter. Fundamental performance differences between CMOS and CCD imagers: Part II. In Thomas J. Grycewicz, Cheryl J. Marshall, and Penny G. Warren, editors, *Focal Plane Arrays for Space Telescopes III*, volume 6690 of *Society of Photo-Optical Instrumentation Engineers (SPIE) Conference Series*, page 669003, September 2007. 2.3.1

[21] Chih-tang Sah, Robert N. Noyce, and William Shockley. Carrier generation and recombination in p-n junctions and p-n junction characteristics. *Proceedings of the IRE*, 45(9):1228–1243, 1957. 2.3.2, 2.3.2

[22] Mario Salvador Cabrera. *Development of 15 μm cutoff wavelength HgCdTe detector arrays for astronomy*. PhD thesis, University of Rochester, New York, January 2020. 2.3.2, 2.3.3

[23] M. A. Kinch. Chapter 7 metal-insulator-semiconductor infrared detectors. In R.K. Willardson and Albert C. Beer, editors, *Mercury Cadmium Telluride*, volume 18 of *Semiconductors and Semimetals*, pages 313–378. Elsevier, 1981. 2.3.3

[24] W. E. Tennant, Donald Lee, Majid Zandian, Eric Piquette, and Michael Carmody. MBE HgCdTe Technology: A Very General Solution to IR Detection, Described by "Rule 07", a Very Convenient Heuristic. *Journal of Electronic Materials*, 37(9):1406–1410, September 2008. 2.3.5

[25] Majid Zandian. Rule-22: An Update to Rule-07. *Journal of Electronic Materials*, 52(11):7095–7102, November 2023. 2.3.5

[26] Guillaume Huber, Michael Bottom, Charles-Antoine Claveau, Shane Jacobson, Matthew Newland, Ian Baker, Keith Barnes, and Matthew Hicks. Glow reduction of ultra-low noise LmAPDs: towards photon counting infrared arrays. In Andrew D. Holland and Kyriaki Minoglou, editors, *X-Ray, Optical, and Infrared Detectors for Astronomy XI*, volume 13103 of *Society of Photo-Optical Instrumentation Engineers (SPIE) Conference Series*, page 1310320, August 2024. 2.3.5

[27] Ian Baker, Matthew Hicks, Chris Maxey, and Daniel Owton. Leonardo UK high performance shortwave APDs for astronomy. In Priyalal Wijewarnasuriya, Arvind I. D'Souza, and Ashok K. Sood, editors, *Infrared Sensors, Devices, and Applications XIII*, volume 12687, page 1268702. International Society for Optics and Photonics, SPIE, 2023. 2.3.5

[28] James W. Beletic, Richard Blank, David Gulbransen, Donald Lee, Markus Loose, Eric C. Piquette, Thomas Sprafke, William E. Tennant, Majid Zandian, and Joseph Zino. Teledyne Imaging Sensors: infrared imaging technologies for astronomy and civil space. In David A. Dorn and Andrew D. Holland, editors, *High Energy, Optical, and Infrared Detectors for Astronomy III*, volume 7021, page 70210H. International Society for Optics and Photonics, SPIE, 2008. 2.3.5

[29] Gregory Mosby Jr., Nathan Eggen, Marsha Wolf, Kurt Jaehnig, and Ralf Kotulla. Persistence characterization and data calibration scheme for the RSS-NIR H2RG detector on SALT. In Andrew D. Holland and James Beletic, editors, *High Energy, Optical, and Infrared Detectors for Astronomy VII*, volume 9915, page 99152U. International Society for Optics and Photonics, SPIE, 2016. 2.4, 3.6

[30] Jarron M. Leisenring, Marcia Rieke, Karl Misselt, and Massimo Robberto. Characterizing persistence in JWST NIRCam flight detectors. In Andrew D. Holland and James Beletic, editors, *High Energy, Optical, and Infrared Detectors for Astronomy VII*, volume 9915

of *Society of Photo-Optical Instrumentation Engineers (SPIE) Conference Series*, page 99152N, August 2016. 2.4

[31] Gregory Mosby, Bernard J. Rauscher, Chris Bennett, Edward S. Cheng, Stephanie Cheung, Analia Cillis, David Content, Dave Cottingham, Roger Foltz, John Gygax, Robert J. Hill, Jeffrey W. Kruk, Jon Mah, Lane Meier, Chris Merchant, Laddawan Miko, Eric C. Piquette, Augustyn Waczynski, and Yiting Wen. Properties and characteristics of the Nancy Grace Roman Space Telescope H4RG-10 detectors. *Journal of Astronomical Telescopes, Instruments, and Systems*, 6:046001, October 2020. 2.4, 3.2.3, 3.4, 3.4, 3.4, 3.6

[32] Derek Ives, Domingo Alvarez, Naidu Bezawada, Elizabeth George, and Benoit Serra. Characterisation, performance and operational aspects of the H4RG-15 near infrared detectors for the MOONS instrument. In Andrew D. Holland and James Beletic, editors, *X-Ray, Optical, and Infrared Detectors for Astronomy IX*, volume 11454 of *Society of Photo-Optical Instrumentation Engineers (SPIE) Conference Series*, page 114541N, December 2020. 2.4, 3.3.3

[33] Roger M. Smith, Maximilian Zavodny, Gustavo Rahmer, and Marco Bonati. A theory for image persistence in HgCdTe photodiodes. In David A. Dorn and Andrew D. Holland, editors, *High Energy, Optical, and Infrared Detectors for Astronomy III*, volume 7021, page 70210J. International Society for Optics and Photonics, SPIE, 2008. 2.4

[34] Roger M. Smith, Maximilian Zavodny, Gustavo Rahmer, and Marco Bonati. Calibration of image persistence in HgCdTe photodiodes. In David A. Dorn and Andrew D. Holland, editors, *High Energy, Optical, and Infrared Detectors for Astronomy III*, volume 7021 of *Society of Photo-Optical Instrumentation Engineers (SPIE) Conference Series*, page 70210K, July 2008. 2.4

[35] Simon Tulloch. Persistence Characterisation of teledyne H2RG detectors. *arXiv e-prints*, page arXiv:1807.05217, July 2018. 2.4

[36] Simon Tulloch, Elizabeth George, and ESO Detector Systems Group. Predictive model of persistence in H2RG detectors. *Journal of Astronomical Telescopes, Instruments, and Systems*, 5:036004, July 2019. 2.4

[37] K. Jóźwikowski, A. Jóźwikowska, M. Kopytko, A. Rogalski, and L.R. Jaroszewicz. Dislocations as a noise source in lwir hgcdte photodiodes. *Journal of Electronic Materials*, 45:4769–4781, 2016. 3.3.2

[38] Candice M. Bacon, Craig W. McMurtry, Judith L. Pipher, Amanda Mainzer, and William Forrest. Effect of dislocations on dark current in LWIR HgCdTe photodiodes. In Andrew D. Holland and David A. Dorn, editors, *High Energy, Optical, and Infrared Detectors for Astronomy IV*, volume 7742, page 77421U. International Society for Optics and Photonics, SPIE, 2010. 3.3.2

[39] Antoni Rogalski. Infrared detectors: status and trends. *Progress in Quantum Electronics*, 27(2):59–210, 2003. 3.3.2

[40] K. Jóźwikowski, A. Jóźwikowska, M. Kopytko, A. Rogalski, and L.R. Jaroszewicz. Simplified model of dislocations as a srh recombination channel in the hgcdte heterostructures. *Infrared Physics and Technology*, 55(1):98–107, 2012. 3.3.2, 3.4

[41] B. S. Chaudhari, H. Goto, M. Niraula, and K. Yasuda. Analysis of dislocations and their correlation with dark currents in cdte/si heterojunction diode-type x-ray detectors. *Journal of Applied Physics*, 130(5):055302, 08 2021. 3.3.2

[42] Olivier Boulade, Vincent Moreau, Patrick Mulet, Olivier Gravrand, Cyril Cervera, Jean-Paul Zanatta, Pierre Castelein, Fabrice Guellec, Bruno Fièque, Philippe Chorier, and Julien Roumegoux. Development activities on NIR large format MCT detectors for astrophysics and space science at CEA and SOFRADIR. In Andrew D. Holland and James Beletic, editors, *High Energy, Optical, and Infrared Detectors for Astronomy VII*, volume 9915 of *Society of Photo-Optical Instrumentation Engineers (SPIE) Conference Series*, page 99150C, July 2016. 3.3.3, 3.3.4

[43] Michael W. Regan and Louis E. Bergeron. Zero dark current in H2RG detectors: it is all multiplexer glow. *Journal of Astronomical Telescopes, Instruments, and Systems*, 6:016001, January 2020. 3.3.3, 3.3.4, 3.3.4, 3.3.7

[44] Naidu Bezawada, Derek Ives, Elizabeth George, Domingo Alvarez, Benoit Serra, Mark Farris, Anders Petersen, and Liz Corrales. Output buffer glow and its mitigation in H4RG-15 detectors. *Journal of Astronomical Telescopes, Instruments, and Systems*, 10(2):026007, 2024. 3.3.3, 3.3.5

[45] K. Lehovec, C. A. Accardo, and E. Jamgochian. Injected Light Emission of Silicon Carbide Crystals. *Physical Review*, 83(3):603–607, August 1951. 3.3.3

[46] E. Fred Schubert. *Light-Emitting Diodes (2nd Edition)*. Cambridge University Press, 2006. 3.3.3

[47] S. Tam and Chenming Hu. Hot-electron-induced photon and photocarrier generation in silicon mosfet's. *IEEE Transactions on Electron Devices*, 31(9):1264–1273, 1984. 3.3.3

[48] Jeff Bude, Nobuyuki Sano, and Akira Yoshii. Hot-carrier luminescence in Si. *Physical Review B*, 45(11):5848–5856, March 1992. 3.3.3

[49] L Carbone, R Brunetti, C Jacoboni, A Lacaita, and M Fischetti. Polarization analysis of hot-carrier light emission in silicon. *Semiconductor Science and Technology*, 9(5S):674, may 1994. 3.3.3

[50] Franco Stellari, F. Zappa, S. Cova, and L. Vendrame. Tools for non-invasive optical characterization of cmos circuits. pages 487 – 490, 02 1999. 3.3.3

[51] Stephan Maestre, Pierre Magnan, Francis Lavernhe, and Franck Corbiere. Hot carriers effects and electroluminescence in the CMOS photodiode active pixel sensors. In Nitin Sampat, Ricardo J. Motta, Morley M. Blouke, Nitin Sampat, and Ricardo J. Motta, editors, *Sensors and Camera Systems for Scientific, Industrial, and Digital Photography Applications IV*, volume 5017, pages 59 – 67. International Society for Optics and Photonics, SPIE, 2003. 3.3.3, 3.3.4

[52] JMCE Jon Clarke. private communication. 3.3.4

[53] Karl Pearson. The Problem of the Random Walk. Nature, 72(1865):294, July 1905. 3.4

[54] Gregory Mosby, Bob Hill, Analia Cillis, Roger Foltz, Chris Bennett, Mario Cabrera, Michael Hickey, Chris Merchant, Augustyn Waczynski, Yiting Wen, Bernie Rauscher, Edward J. Wollack, Jeff Kruk, John Auyeung, Joshua Schlieder, Eric Switzer, Maxime Rizzo, Neil Zimmerman, Edward Cheng, Craig Cabelli, Eric Piquette, Jianmei Pan, Mark Farris, Anders Petersen, John Gygax, Colin Stuart, Dave Cottingham, Jonathan Mah, Stephanie Cheung, Lane Meier, Daniel Kelly, and Steven Mann. Summary of the Nancy Grace Roman Space Telescope flight detector performance. *Journal of Astronomical Telescopes, Instruments, and Systems*, 11:011210, January 2025. 3.4, 3.6

[55] Rachel P. Dudik, Margaret E. Jordan, Bryan N. Dorland, Daniel Veillette, Augustyn Waczynski, Benjamin F. Lane, Markus Loose, Emily Kan, James Waterman, Chris Rollins, and Steve Pravdo. Interpixel crosstalk in teledyne imaging sensors h4rg-10 detectors. *Applied Optics*, 51(15):2877, May 2012. 3.4

[56] Bernard J. Rauscher, David Alexander, Clifford K. Brambora, Meng Chiao, Brian L. Clemons, Rebecca Derro, Charles Engler, Ori Fox, Matthew B. Garrison, Matthew A. Greenhouse, Greg Henegar, Robert J. Hill, Thomas Johnson, Rodolfo J. Lavaque, Don J. Lindler, Sridhar S. Manthripragada, Cheryl Marshall, Brent Mott, Thomas M. Parr, Wayne D. Roher, Kamdin B. Shakoorzadeh, Miles Smith, Augustyn Waczynski, Yiting Wen, Donna Wilson, Mary Ballard, Craig Cabelli, Edward Cheng, James Garnett, Elliott Koch, Markus Loose, Majid Zandian, Joseph Zino, Timothy Ellis, Bryan Howe, Miriam Jurado, Ginn Lee, John Nieznanski, Peter Wallis, James York, Michael W. Regan, Giorgio Bagnasco, Torsten Böker, Guido De Marchi, Pierre Ferruit, Peter Jakobsen, and Paolo Strada. James Webb Space Telescope Near-Infrared Spectrograph: dark performance of the first flight candidate detector arrays. In David A. Dorn and Andrew D. Holland, editors, *High Energy, Optical, and Infrared Detectors for Astronomy III*, volume 7021, page 702124. International Society for Optics and Photonics, SPIE, 2008. 3.4

[57] Christopher V. Griffith, Stephen D. Bongiorno, David N. Burrows, Abraham D. Falcone, and Zachary R. Prieskorn. Characterization of an x-ray hybrid CMOS detector with low interpixel capacitive crosstalk. In Andrew D. Holland and James W. Beletic, editors, *High Energy, Optical, and Infrared Detectors for Astronomy V*, volume 8453, page 84530F. International Society for Optics and Photonics, SPIE, 2012. 3.4

[58] Donald F. Figer, Justin Gallagher, Lazar Buntic, Jonathan Getty, and Stefan Lauxtermann. The SATIN infrared detector development program and the road to HELLSTAR. In Andrew D. Holland and James Beletic, editors, *X-Ray, Optical, and Infrared Detectors for Astronomy X*, volume 12191 of *Society of Photo-Optical Instrumentation Engineers (SPIE) Conference Series*, page 121910P, August 2022. 3.4, 3.6

[59] A. A. Plazas, C. Shapiro, R. Smith, E. Huff, and J. Rhodes. Laboratory Measurement of the Brighter-fatter Effect in an H2RG Infrared Detector. PASP, 130(988):065004, June 2018. 3.6

[60] Justin P. Gallagher, Lazar Buntic, Donald F. Figer, and Wei Deng. Characterization of single-photon sensing and photon-number resolving CMOS image sensors. In Andrew D. Holland and James Beletic, editors, *X-Ray, Optical, and Infrared Detectors for Astronomy X*, volume 12191 of *Society of Photo-Optical Instrumentation Engineers (SPIE) Conference Series*, page 121910T, August 2022. 4.1

[61] Lance M. Simms, Donald F. Figer, Brandon J. Hanold, Daniel J. Kerr, D. Kirk Gilmore, Steven M. Kahn, and J. Anthony Tyson. First use of a HyViSI H4RG for astronomical observations. In Thomas J. Grycewicz, Cheryl J. Marshall, and Penny G. Warren, editors, *Focal Plane Arrays for Space Telescopes III*, volume 6690 of *Society of Photo-Optical Instrumentation Engineers (SPIE) Conference Series*, page 66900H, September 2007. 4.1

[62] W. H. Krase and Kathleen A. Wolf. *Astronomy and sodium lighting.* 1984. 4.1

[63] D. C. Wells, E. W. Greisen, and R. H. Harten. FITS - a Flexible Image Transport System. *Astronomy and Astrophysics, Supplement*, 44:363, June 1981. 4.3

[64] A. Viana and T. Wiklind. *NICMOS Instrument Handbook*. STScI, 2009. 4.3

[65] J. D. Offenberg, D. J. Fixsen, B. J. Rauscher, W. J. Forrest, R. J. Hanisch, J. C. Mather, M. E. McKelvey, Jr. McMurray, R. E., M. A. Nieto-Santisteban, J. L. Pipher, R. Sengupta, and H. S. Stockman. Validation of Up-the-Ramp Sampling with Cosmic-Ray Rejection on Infrared Detectors. PASP, 113(780):240–254, February 2001. 4.3

[66] F. A. Ringwald. A Cookbook for Reducing KPNO Infrared Array Data. In Diana M. Worrall, Chris Biemesderfer, and Jeannette Barnes, editors, *Astronomical Data Analysis Software and Systems I*, volume 25 of *Astronomical Society of the Pacific Conference Series*, page 328, January 1992. 4.3

[67] R. M. Cutri, M. F. Skrutskie, S. van Dyk, C. A. Beichman, J. M. Carpenter, T. Chester, L. Cambresy, T. Evans, J. Fowler, J. Gizis, E. Howard, J. Huchra, T. Jarrett, E. L. Kopan, J. D. Kirkpatrick, R. M. Light, K. A. Marsh, H. McCallon, S. Schneider, R. Stiening, M. Sykes, M. Weinberg, W. A. Wheaton, S. Wheelock, and N. Zacarias. *2MASS All Sky Catalog of point sources.* 2003. 4.3

[68] John Bally, Adam Ginsburg, Jan Forbrich, and Jaime Vargas-González. The Orion Protostellar Explosion and Runaway Stars Revisited: Stellar Masses, Disk Retention, and an Outflow from the Becklin-Neugebauer Object. ApJ, 889(2):178, February 2020. 4.4

[69] Lynne A. Hillenbrand. On the Stellar Population and Star-Forming History of the Orion Nebula Cluster. AJ, 113:1733–1768, May 1997. 4.4

[70] E. E. Becklin and G. Neugebauer. Observations of an Infrared Star in the Orion Nebula. ApJ, 147:799, February 1967. 4.4

[71] V. Straižys, K. Milašius, R. P. Boyle, F. J. Vrba, U. Munari, N. R. Walborn, K. Černis, A. Kazlauskas, K. Zdanavičius, R. Janusz, J. Zdanavičius, and V. Laugalys. The Enigma of the Open Cluster M29 (NGC 6913) Solved. AJ, 148(5):89, November 2014. 4.5

[72] V. Straižys, F. J. Vrba, R. P. Boyle, K. Milašius, K. Černis, K. Zdanavičius, J. Zdanavičius, A. Kazlauskas, M. Macijauskas, and R. Janusz. Interstellar Extinction in the Direction of the Open Cluster M29. AJ, 149(5):161, May 2015. 4.5